

Simulations of X-ray Bursts and Superbursts

Inauguraldissertation

zur
Erlangung der Würde eines Doktors der Philosophie
vorgelegt der
Philosophisch-Naturwissenschaftlichen Fakultät
der Universität Basel
von

Sofie Fehlmann

aus Schafisheim, AG

Basel 2015

Originaldokument gespeichert auf dem Dokumentenserver der Universität Basel
edoc.unibas.ch



This work is licensed under a Creative Commons
Attribution-NonCommercial-NoDerivatives 4.0 International License.

Genehmigt von der Philosophisch-Naturwissenschaftlichen Fakultät auf Antrag von

Prof. Dr. F.-K. Thielemann

PD Dr. M. Falanga

Basel, den 21. April 2015

Prof. Dr. J. Schibler

Dedicated to my stepfather

Uwe Murr

who died unexpectedly during my PhD.

Acknowledgements

I would like to acknowledge Prof. F.-K. Thielemann for supervising my work and giving me the possibility to present my results at international conferences. Thanks also to J. Reichert who was trying to help me with the nuclear network calculations.

The results obtained in this thesis would not have been possible without the collaboration and support of a variety of people. Therefore, many thanks go to:

M. Frensel: For always being interested in my recent results and the long discussions we had on the forth floor just after lunch.

Dr. M. Chakraborty: For updating me with the recent news in observations of X-ray bursts. Her views had a significant influence on the development of my PhD work.

Dr. M. Hempel: For supporting me before, during and after the conference in Florence 2014. I will never forget all his offers for help.

My family: For just being crazy and different! It's great to be a part of such a cool family!

Dancing mates and JJJC Olten: For giving me the opportunity to relax and have fun after a tough day of work. They encouraged and helped me to get rid of frustrations due to failures and problems which I encountered during my work.

Abstract

Observations of neutron star in binary systems provide powerful constrains on the physics at the surface of neutron stars. During the accretion of matter from the companion star, periodic nuclear explosion are triggered in the outer layers of the neutron star, increasing the luminosity during a time range of a few minutes. Rarely, one can also detect day-long explosions in accreting binary systems. The nature of those two kind of bursts is still not well understood. In fact, simplified simulations of the outer layers of an accreting neutron star in a binary are not yet able to reproduce all observable features.

The work presented in this thesis is devoted to the one-dimensional simulations of X-ray bursts and superbursts. The numerical code used in this work has initially been programmed by J. Fisker in 2006. By updating and optimizing the code, we are able to simulate X-ray bursts as well as superbursts in a feasible time range. Using a large nuclear network, we study the features of X-ray bursts and compare them with observations. To understand the link between various properties entering our simulations as parameters or boundary conditions, we present several models which reproduces hundreds of X-ray burst. In this current work, we focus mainly on changes in crustal heating, accretion rate and accretion composition. Analyzing the influence on the light curve as well as on the ashes of X-ray bursts, we are able to compare our results with observations. To shed some light on the self-consistent ignition of a superburst, we model a setup which may lead to the ignition of a superburst.

Our results suggest that additional helium, heavier isotopes and the lack of hydrogen in the accretion composition help to generate carbon-rich X-ray burst ashes. Strong heating below the superburst ignition layer prevents the destruction of carbon after an X-ray bursts and might be the key ingredience in the self-consistent ignition of a superburst within the time range of the observed recurrence time.

Table of contents

List of figures	xii
List of tables	xv
1 Introduction	1
1.1 Neutron star layers	1
1.1.1 Photosphere	3
1.1.2 Atmosphere	4
1.1.3 Ocean	5
1.1.4 Crust	5
1.1.5 Core	5
1.2 X-ray burst	6
1.3 Superburst	9
1.4 Goals of this Work	11
2 Tools for Simulations of X-ray Bursts and Superbursts	15
2.1 Hydrodynamics	16
2.1.1 Equation of state	19
2.1.2 Heat Transport	20
2.1.3 Adaptive Grid	23
2.1.4 Adaptive Grid Modification	25
2.1.5 Boundary Conditions	26
2.2 Nuclear Reaction Network	29
2.3 Convective Mixing	33
2.3.1 Weakness of Mixing Length Theory	33
2.4 Advection of the composition	34
2.5 A short comparison with the MESA and KEPLER	35

3	Nuclear Network Test	37
3.1	Initial Model	37
3.2	Nuclear network comparison	39
3.2.1	Model with $0.1 \dot{M}_{\text{edd}}$	40
3.2.2	Model with $0.025 \dot{M}_{\text{edd}}$	43
3.2.3	Problems with Use of Reduced Network	46
4	Simulations of X-ray bursts	49
4.1	Surface Layer	51
4.2	Ignition zone	52
4.3	Ashes	58
4.4	Opacity	59
5	Crustal Heating	63
5.1	Simulations with variations of crustal heating	64
5.2	Observable properties and crustal heating	74
5.2.1	Accretion Rate	75
5.2.2	Composition	93
6	Simulations of Superbursts	119
6.1	Increasing the computational domain	120
6.2	Models	121
6.2.1	Fast accretion model	122
6.2.2	Standard accretion model	124
6.2.3	Slow accretion model	124
6.3	Simulation of superbursts	126
7	Summary and outlook	127
7.0.1	Future projects	131
	References	133
	Curriculum Vitae	139

List of figures

1.1	Shell model of a neutron star	2
1.2	Schematic view of a neutron star binary system	3
1.3	Observational data from an X-ray burst in 4U 1254-69	7
1.4	Schematic view of X-ray burst ignition conditions	8
1.5	Observational data from the superburst KS 1731-260	9
2.1	Schematic view of the code	15
3.1	Schematic view of progenitor file	39
3.2	Network comparison	40
3.3	Ashes obtained with different networks at high accretion rate.	42
3.5	Ashes obtained with different networks at low accretion rate.	45
3.7	Comparison of the opacities	47
4.1	Kippenhahn diagram of the burn rate and temperature. The time axis is chosen such that the peak burst luminosity is found at $t = 0$ s. The burn rate is described in units of s^{-1} , the temperature in units of K. . .	50
4.2	Composition change during a single X-ray burst	52
4.3	Schematic view of the ignition reactions	53
4.4	Composition in the ignition zone before ignition	54
4.5	Composition in the ignition zone at peak luminosity	56
4.6	Composition in the ignition zone after the burst	57
4.7	Mass fraction of specific isotopes in function of the density	58
4.8	The thermal, radiative and total opacity between two bursts	59
4.9	The radiative, electron scattering and free-free opacity between two bursts	60

5.1	Kippenhahn diagram of the burn rate for different crustal heating at the inner boundary. The time axis is chosen such that the peak burst luminosity is found at $t = 0$ s. The burn rate is described in units of s^{-1} and the column density in units of g cm^{-2}	64
5.2	Recurrence time versus crust heating	66
5.3	Hydrogen, helium and hydrogen as a function function of density and temperature. The dashed profile corresponds to a crust heating of 1.5 MeV/nuc and the solid profile indicates the solution with a crust heating of 0.5 MeV/nuc.	66
5.4	Time evolution of the composition at ignition with two different heating sources	67
5.5	Convection and semi-convection at low accretion rate	68
5.6	Convection and semi-convection at low accretion rate	69
5.7	Peak luminosity and quiescence luminosity as a function of the heating at the inner boundary	70
5.8	Comparison of the burst luminosities for different heating	71
5.9	Comparison of different opacities for two values of boundary heating . .	71
5.10	Comparison of the ashes for high and low heating sources	72
5.11	Crust heating versus the mass fractions of ^{12}C with a constant accretion rate	73
5.12	Observed photon count rate of typical Type I X-ray bursts	74
5.13	Recurrence time in function of the boundary luminosity	76
5.14	Temperature versus column density at different accretion rates	78
5.15	The burn rate in function of the column density and time. The time $t = 0$ s coincides with the burst peak luminosity. For both accretion rate models, we used zero additional heating at the inner boundary. . .	79
5.16	The time axis is chosen such that the burst peak luminosity is at $t = 0$ s. To get a correct comparison, we used zero additional heating at the inner boundary.	80
5.17	Convection and semi-convection at low accretion rate	82
5.18	Convection and semi-convection at low accretion rate	82
5.19	Burst luminosity at different accretion rates	83
5.20	Opacities at different accretion rates	84

5.21	The composition at the ignition depth just before the ignition takes place (left figure) and the composition below the ignition depth at the inner boundary (right figure). The red line corresponds to an accretion rate of $2 \cdot 10^{17}$ g/s, whereas the black line corresponds to $5 \cdot 10^{16}$ g/s. The x-axis indicates the mass number and the y-axis corresponds to the logarithm of the mass fraction. You should note that the crustal heating has been set to zero for both simulations.	85
5.22	Ignition zone temperature at different accretion rates	86
5.23	The diagram of e -folding time of observations of X-ray bursts	87
5.24	The e -folding time and rise time of X-ray bursts with different accretion rates in function of the crust luminosity at the inner boundary.	88
5.25	The ratio of persistent fluence to burst fluence	90
5.26	The mass fraction of carbon and helium at a density of $9 \cdot 10^6$ g/cm ³ for different accretion models. The x-axis denotes the crust luminosity at the inner boundary of our model.	91
5.27	Recurrence time of X-ray bursts in function of heating for different ratios of He/H in the accretion compositions	94
5.28	Recurrence time of X-ray bursts in function of heating for models with different amount of heavier isotopes	95
5.29	Temperature profiles of different accretion compositions	96
5.30	Kippenhahn diagrams of various accretion composition models	98
5.31	Helium and hydrogen in function of time and column density for the hydrogen-rich accretion	99
5.32	Helium and hydrogen in function of time and column density for the solar accretion	99
5.33	Helium and hydrogen in function of time and column density for the helium 1 accretion	100
5.34	Helium and hydrogen in function of time and column density for the helium 2 accretion	100
5.35	The burn rate in function of column density and time for the heavy 1 and heavy 2 model (see Table 5.4). For both models, we do not apply an additional heating ($Q_{heat} = 0$ MeV/nuc) in order to compare results with other setups. The time axis is chosen such that the peak burst luminosity takes place at $t = 0$ s.	101

5.36 Helium and hydrogen in function of time and column density for the heavy 1 accretion model	102
5.37 Helium and hydrogen in function of time and column density for the heavy 1 accretion model	102
5.38 Burst luminosities for different accretion composition models	103
5.39 Temperature evolution of the solar abundance model and the heavy 2 model	104
5.40 Electron abundance evolution of the solar abundance model and the heavy 2 model	105
5.41 The average rise time in function of crustal heating for different accretion compositions.	107
5.42 The average e -folding time in function of crustal heating for different accretion compositions.	108
5.43 The α value in function of heating at the inner boundary	109
5.45 Convective zone for the hydrogen-rich accretion	110
5.46 Convective zone for the solar abundance accretion	111
5.47 Convective zone for the helium-rich 1 accretion	111
5.48 Convective zone for the helium-rich accretion	112
5.49 Convective zone for the heavy 1 accretion	112
5.50 Convective zone for the heavy 2 accretion	113
5.51 Total opacity in function of column density	113
5.52 The composition of the ashes with different accretion compositions . . .	114
5.53 The mass fraction of carbon and helium in the ashes in function of heating with different ratios of hydrogen to helium in the accretion compositions	115
5.54 The mass fraction of carbon and helium in the ashes in function of heating with different ratios of hydrogen/helium to heavier isotopes in the accretion compositions	115
6.1 Burst luminosity of the test X-ray burst model with fast accretion . . .	123
6.2 Typical burst luminosity of the test X-ray burst model with fast accretion	124

List of tables

1.1	List of Superbursts	10
2.1	List of Isotopes from the 304 network	31
2.2	List of Isotopes from the 561 network	32
3.1	Burst comparison with different reaction networks using a high accretion rate	41
3.2	Burst comparison with different reaction networks using a low accretion rate	44
5.1	Accretion rate models	76
5.2	Ignition conditions at different accretion rates	81
5.3	Properties concerning the mass fraction of carbon in the ashes with different accretion rate models	92
5.4	Description of the models with variations in the accretion composition	93
5.5	Ignition conditions of different accretion composition models	103
5.6	Properties concerning the mass fraction of carbon in the ashes with different accretion compositions	116
6.1	Problems and possible solution at higher accretion rates	122
6.2	Features of the fast accretion superburst model	123
7.1	Summary of how accretion rate and heating affects the X-ray bursts	129
7.2	Summary of how the accretion composition affects the X-ray bursts	129

Chapter 1

Introduction

Neutron stars are compact objects which can be directly observed. They have a typical radius of about 10 km which includes a mass of about $1 - 2 M_{\odot}$. Due to their high density, neutron stars provide a unique laboratory to study fundamental aspects in astrophysics including the behaviour of strong magnetic fields, the properties of nuclear forces at high densities, phase transitions to exotic matter and the effects of strong gravitation. They are born hot in old massive stars when the core is collapsing and the outer layers exploding as a supernova. During the collapse phase, degenerate neutrons are formed by electron capture on protons. If the mass of the initial star is less than approximately $25 M_{\odot}$, the collapse is stopped by the degeneracy pressure. As a second option, neutron stars can also be formed in binary systems through the accretion induced collapse of a white dwarf. Such a collapse generates a supernova which either destroys the initial object or forms a neutron star.

1.1 Neutron star layers

Neutron stars are divided into different layers: a core, an inner crust, an outer crust, an ocean, an atmosphere and a photosphere (see figure 1.1). In the studies of X-ray bursts, one is typically describing the depth in terms of the column density. The relativistic column density y at a radius r inside the neutron is given as

$$y(r) = \int_{R-r}^R \rho(r') \frac{dr'}{\Gamma}, \quad (1.1)$$

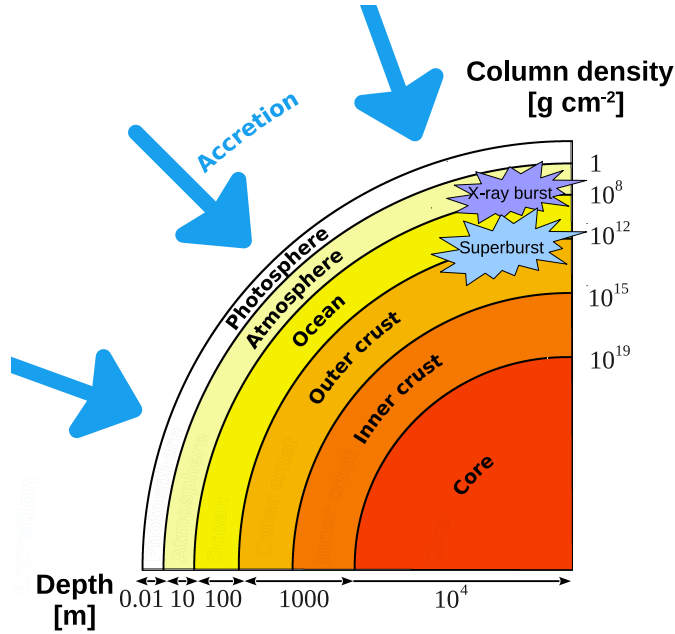


Fig. 1.1 Different shells of an accreting neutron star. Note that the accretion rate is locally changing and not constant over the surface of the neutron star.

where R is the radius of the neutron star, ρ is the density and

$$\Gamma = \sqrt{1 - \frac{2GM}{Rc^2}}, \quad (1.2)$$

with M being the mass of the neutron star. The column density is in units of g cm^{-2} and is a parameter of how much matter is lying above a certain radius. The larger the column density, the closer the depth to the center of the neutron star.

A few percent of neutron stars are located in binary systems. The companion stars in such binary systems may be either ordinary stars, white dwarfs, neutron stars or possibly black holes. In the current work, we want to focus on accreting neutron stars in a binary systems with an ordinary stars or a white dwarfs, see Figure 1.2. Through Roche lobe overflow, matter which is accreted from a binary companion onto the surface of a neutron star. The accreted matter is thought to consist of mainly hydrogen, helium and a small amount of heavier elements. In the following subsections, we will have a closer look at what happens with the accreted matter in the different layers.

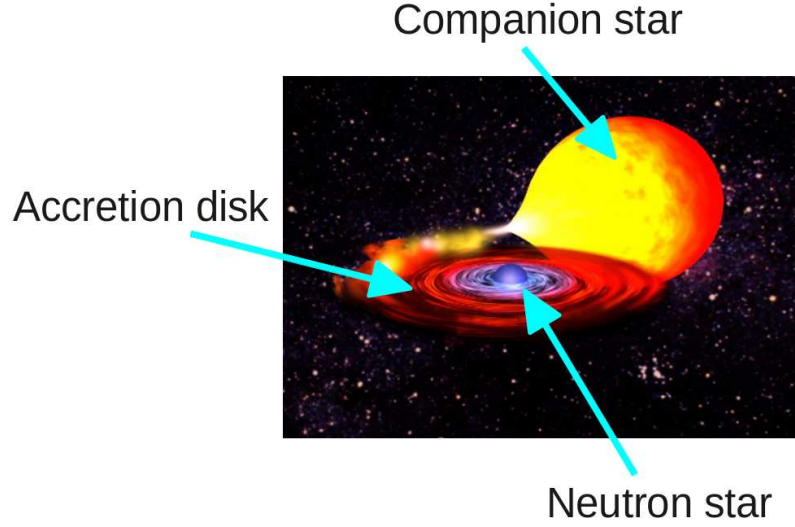


Fig. 1.2 A schematic view of a neutron star binary system with a low mass companion star.

1.1.1 Photosphere

If the angular momentum of the a stream of matter, which is transferred through the first Langrange point, exceeds $r_I c$, where r_I is the radius of the innermost stable orbit, it forms an accretion disk (Prendergast and Burbidge, 1968). In such an accretion disk, matter interacts by turbulences and magnetic fields and is finally ether accreted onto the surface of the neutron star, returned to the binary companion or thrown out of the binary system through the second Lagrange point (Shapiro and Teukolsky, 1983). Matter impacting the surface of the neutron star decelerate from Keplerian velocity to the spin velocity of the neutron star. This process heats the photosphere to a few hunderd million degree and causes a persistent X-ray emission. The total energy release from mass transfer is given by

$$L = \left(1 - \sqrt{1 - \frac{2GM}{Rc^2}} \right) \dot{M}c^2 \quad (1.3)$$

where one assumed that matter enters from infinity. In the expression above, c is the speed of light, $G = 6.673 \cdot 10^{-8} \text{dyn cm}^2 \text{g}^{-2}$ is the gravitational constant, M and R is the gravitational mass and the radius of the neutron star respectively. By the reason that the persistent luminosity one observes from an accreting neutron star includes

also the luminosity due to interactions in the disk, one can hardly conclude from the observed luminosity about the instantaneous accretion rate.

1.1.2 Atmosphere

The thickness of the atmosphere of a star depends on the balance between the gravitational force and pressure due to temperature and density. Neutron stars have very strong gravitational field of the order of $g \sim 10^{14} \text{cm s}^{-2}$. Thus, the compressed atmospheres have usually a thickness of a few centimeters for accreting neutron stars, while cold neutron stars have atmospheres with a thickness of only a few millimeters. As a comparison, the earth's atmosphere has a thickness of over 100 km. By the reason that the gravitational field of a neutron star is very strong, the hydrostatic balance requires a high pressure and hence a high density. The physics of the atmosphere of neutron stars have been studied by many authors, see e.g. ?, but current atmosphere models are still far from being complete.

The accreted matter consists of the compositions of the donor star's surface which is typically a late-type zero-age main sequence (ZAMS) donor or a white dwarf donor. For ZAMS, one expect an accretion composition with a mixture of hydrogen and helium, whereas for white dwarf donors, the accreted matter is helium-rich. In the atmosphere of a neutron star, matter is thought to be fully ionized. Freshly accreted matter is continuously piled on top and consequently, the composition in the atmosphere undergoes a gradual compression. Such a spatial compression of electron wavefunctions fills the available electron phase-space and makes the electron degenerate. By the reason that the degeneracy pressure is a quantum effect, the electrons can be approximated as a temperature-independent Fermi-Dirac gas. On the other side, the Compton wavelength of nucleons is much shorter due to their mass. This means that in the atmosphere, the phase space of the nucleons is not filled up and hence, one can describe the nucleons as an ideal gas which is temperature dependent.

If the radiative force exceeds the gravitational force, the atmosphere gets unstable to plasma outflow. In hot and non-magnetized atmosphere, the radiative force is produced mainly by Thomson scattering and thus, plasma outflow takes place if the stellar luminosity exceeds the Eddington limit

$$L_{edd} = \frac{4\pi cGMm_p}{\sigma_0}, \quad (1.4)$$

where m_p is the proton mass and σ_0 is the Thomson scattering cross section.

1.1.3 Ocean

Below the atmosphere of a neutron star, matter is accumulated in the ocean. The ocean of a neutron star is very important in the current study since the ocean hosts the possible ignition of a superburst. The composition in the ocean consists of accumulated ashes stable or unstable nuclear burning. Since temperature and density is increasing, the composition in the ocean could possibly burn in a stable manner. In order to explain the observations of superbursts, the ocean of a neutron star should contain a rather large amount of carbon which is basically acting as fuel of a superburst (Hashimoto et al., 2014; Keek and Heger, 2011). Recent studies of phase separations in the crust (Horowitz et al., 2007) indicate that layers below the ocean of a neutron star might provide additional carbon which enable the ignition of a superburst in the ocean.

The ocean of the neutron star has gained in interest as recent studies of the cooling behaviour of neutron star indicate that an additional and strong heating source might be located in the crust, see for example Shternin et al. (2011); Turlione et al. (2013). Up to now, the nature of this source remains still a mystery.

1.1.4 Crust

As matter of the ocean is compressed further due to the accretion of fresh matter, it will eventually solidifies to form the crust of the neutron star. The crust has a typical thickness of the order of 1 km. It is responsible for a heat flux towards the surface and the core of the neutron star since it gives rise to pycnonuclear reactions (Yakovlev et al., 2005). However, recent calculations of Schatz et al. (2013) indicate that the neutrino cooling is very efficient, therefore decoupling the crust and core from the outer layers.

It is thought that the matter in the crust consists of exotic neutron-rich nuclei, relativistic electrons and a superfluid of neutrons. The current theory predicts that highly deformed nuclear clusters with unusual shapes might possibly exist near the crust-core interface. Those clusters are referred as the nuclear pasta phases.

1.1.5 Core

The core has a thickness of several kilometers in a density range of $0.5\rho_0 \leq \rho \lesssim 20\rho_0$, where $\rho_0 = 2.8 \cdot 10^{14} \text{g/cm}^{-3}$ is the saturation nuclear matter density. The composition of the core and the equation of state is highly hypothetical. In the outer part of the

core, there is thought to be matter mainly consisting of neutrons with a few protons, electrons and possibly muons. While the electrons and muons form an almost ideal Fermi gas in the outer region of the core, the neutrons and protons are thought to be described by a strongly interacting Fermi liquid and could be possibly in superfluid state.

In deeper layers of the core, the density is tremendously high and hence, the form of the matter is presumably exotic. Indeed, there are four main hypotheses about the constituents and the behaviour of matter in the inner core of a neutron star:

Hyperonization: Nucleons could convert to hyperons in order to achieve a lower energy level of the dense neutron star matter. Mostly hyperons such as Σ^{-1} and Λ might appear in the composition of the core.

Pion condensation: Pions mediate the interaction between nucleons and might condense into a macroscopic state at extremely high densities. Such a pion condensate is superconducting.

Kaon condensation: Due to the interaction of between kaons and the nucleons, the energy of the kaons will decrease with increasing density until a Bose-Einstein condensate of kaons might be formed.

Phase transition to quark matter: A phase transition to mostly u, d and s quarks might take place.

Probably, the ultra-dense matter in the neutron star core is found to be in mixed phases. A detailed description of the core is very sophisticated and far from being complete.

1.2 X-ray burst

So called Type I X-ray bursts are thought to be the most frequent thermonuclear explosions in the universe and thus provide a large amount of observational data that can be used to determine the properties of matter in the surface layers of a neutron star. Depending on the accretion as well on the temperature and density at the outer layers of the neutron star, X-ray bursts are thought to be ignited in the atmosphere or in the upper ocean. Prior to the explosion, the electrons in the accreted fuel at the ignition depth behave like a degenerate gas while the nuclei can be described by

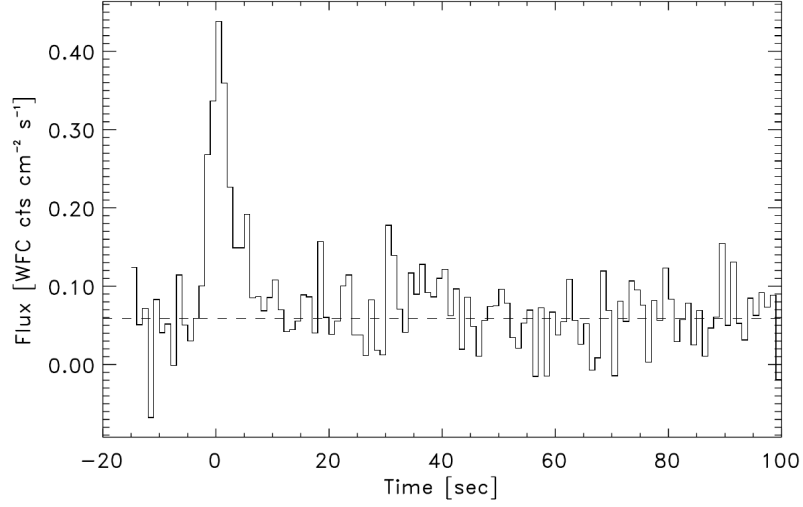


Fig. 1.3 Measurement of a X-ray burst in 4U 1254-69 (In't Zand et al., 2003)

an ideal gas. By the reason that the partial pressure of the nuclei is small compared to the partial degenerate pressure of the electrons, the total pressure of the matter at ignition depth behaves like a degenerate gas. As a consequence, the atmosphere respectively the ocean does not respond to temperature changes by expanding or contracting. Therefore, the gas depends on heat transport by radiation, conduction and convection. This gives rise to thin-shell thermal instabilities which were first discussed by Hansen and Van Horn (1975). Such instabilities cause a nuclear runaway if and only if the nuclear energy release rate becomes more sensitive to temperature perturbations than the corresponding cooling rate (Rakavy et al., 1967):

$$\frac{d\epsilon_{nuc}}{dT} \geq \frac{d\epsilon_{cool}}{dT}, \quad (1.5)$$

where ϵ_{nuc} is the time rate of the nuclear energy release and ϵ_{cool} is the divergence of the heat flux. A runaway is therefore triggered if the reactions in the matter become thermally sensitive by the triple-alpha reaction or by the rp -process (Schatz et al., 1998; Van Wormer et al., 1994; Wallace and Woosley, 1981). The exact features of a X-ray burst depend on the composition of the fuel, reaction rates and conditions at the ignition layer. In addition, since magnetic field, rotation and gravitational interactions with a binary star influence the accretion of matter, it is very unlikely that an explosive runaway is triggered simultaneously over the entire surface of the neutron star. Indeed, observations of X-ray burst light curves exhibit so-called burst oscillations (Strohmayer et al., 1996; Watts, 2012) which give rise to a propagating

burning front.

In general, a typical X-ray burst shows a steep rise in luminosity just after ignition, see for example Figure 1.3. The decay of the luminosity is usually taking place in a time range of a few tens of seconds. Observations of X-ray bursts reveal a constant recurrence time of the order of a few hours during a time frame with a presumably constant accretion rate.

The heat which is generated during a Type I X-ray burst is transported towards the surface and the inner layers of the neutron star respectively. However, due to efficient neutrino cooling (Schatz et al., 2013), the outer layers of the neutron star are thermally decoupled from the core. Nevertheless, the resulting heat flux of X-ray bursts is thought to play a crucial role during the ignition of a superburst.

The ignition and evolution of a single X-ray burst is very sophisticated and depends

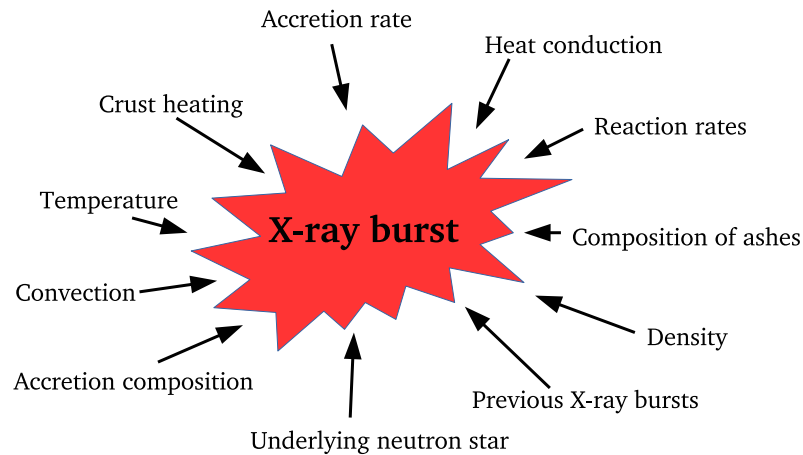


Fig. 1.4 A schematic view of the parameters which influence the ignition and evolution of a X-ray burst.

on various conditions, see Figure 1.4. The majority of those conditions are not yet fully understood at the ignition depth of X-ray bursts. To make things worse, the conditions which influence the X-ray bursts are closely linked to each others. Some of the parameters can be constrained by observations, such as for example the accretion rate or part of the accretion composition. Experiments and statistical simulations can help to constrain the reaction rates of the *rp*-process. However, a large fraction of the reaction rates along the *rp*-process are still uncertain (Amthor et al., 2006). Using

observational constraints, theoretical simulations of X-ray burst help to understand the missing physics and to manifest the reaction rates along the rp -process path. Hence, in order to develop an understanding of the outer layers of a neutron star and its bursts, one needs to couple and compare results from observations, theoretical models and experiments.

1.3 Superburst

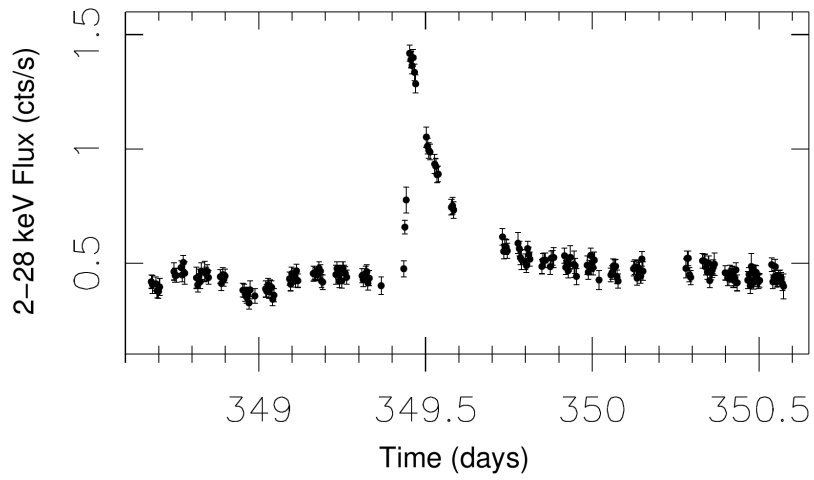


Fig. 1.5 Measurement of a superburst in KS 1731-260 (Kuulkers et al., 2002)

The discovery of superbursts at the surface of neutron stars provided a new area to study the physics of the surface layers as well as the nuclear burning. In principle, a superburst is observed as a very long X-ray burst, emitting a thousand times more energy than normal bursts.

Object	Instrument	Accretion	Superbursts	References
SAX J1747.0-2853	INTEGRAL '11 (?)	? (transient)	1 (?)	Chenevez et al. (2011)
EXO 1745-248	MAXI '11	$\sim 0.0M_{edd}$ (transient)	1	Serino et al. (2012)
4U 0614+091	All Sky Monitor '05/'14	$0.01M_{edd}$	2	Kuulkers (2005)
4U 1254-69	Wide Filed Cameras '99	$0.13M_{edd}$	1	in Zand et al. (2003)
4U 1608-522	All Sky Monitor '05	$0.03M_{edd}$ (transient)	1	Remillard et al. (2005)
4U 1636-536	All Sky Monitor '96/'98/'01	$0.1M_{edd}$	3	Strohmayer and Brown (2002)
KS 1731-260	Wide Filed Cameras '97	$0.1M_{edd}$ (transient)	1	Kuulkers et al. (2002)
4U 1735-444	Wide Filed Cameras '96	$0.25M_{edd}$	1	Cornelisse et al. (2000)
GX 3+1	All Sky Monitor '99	$0.2M_{edd}$	1	Kuulkers (2002)
GX 17+2	Wide Filed Cameras '96-'01	$0.8M_{edd}$	4	in Zand et al. (2004)
4U 1820-303	PCA '99	$0.1M_{edd}$	1	Strohmayer and Markwardt (2002)
Ser X-1	Wide Filed Cameras '97	$0.2M_{edd}$	1	Cornelisse et al. (2002)

Table 1.1 The table lists the properties of all observed superburster. The accretion rate is given in fraction of Eddington mass accretion rate.

Up to now, while there is data from thousands of type I X-ray bursts, only 18 superbursts from 12 superbursters have been observed. In fact, superbursts are a rather new observational phenomenon. The first superburst was discovered in the system 4U 1735-444 in 1996 by Cornelisse et al. (2000). In 1.1 all detected superbursts are listed with their corresponding properties close to the ignition.

The ignition of superburst is thought to take place at the bottom of the ocean where the column density is of the order 0.1 to $5 \cdot 10^{12}$ g/cm² (Cumming and Macbeth, 2004; Stevens et al., 2014). Analysis of superbursts energetics indicate that superbursts are powered by unstable carbon burning in the ashes of X-ray bursts (Taam and Picklum, 1978; Woosley and Taam, 1976). In fact, simplified multi-zone simulation of a superburst in Keek et al. (2012) have confirmed the connection between superbursts and unstable burning of carbon. However, besides the remarkable agreement with observed superburst light curves, their simulated model is not able to ignite self-consistent superbursts. In order to trigger a superburst within the observed time range of a few years of X-ray bursts, they needed to build artificially a layer of a large amount of carbon. Computational superburst models do not only lack in producing enough carbon at the ignition depth, but also fail to explain the recurrence time of observed superbursts.

The appearance of superburst can act as an additional constrain on the unknown parameters in the field of explosions of X-ray bursts. In fact, the ignition of a superburst is strongly linked to the previous X-ray bursts. On the other side, a superburst is an energy-rich explosion which heats the layers at the surface of the neutron star, quenching the appearance of X-ray bursts for a while. A realistic simulation of superbursts at the surface layers of a neutron star in a binary system requires therefore the simulations of thousands of preceding X-ray bursts.

1.4 Goals of this Work

The motivation of this study is to understand the link between various parameters which influence X-ray burst as well as superburst ignition and evolution. Observations, experiments and simulations can help us to constrain the unknown physics at the surface of a neutron star. However, due to the extraordinary conditions at the surface of neutron star, the understanding of X-ray bursts and superburst is far from being complete.

In order to study how certain parameters might influence ignition of bursts and how

they fit into the system of conditions, we adapt a numerical simulation model of the surface layer of a neutron star. While it is yet not possible to generate real conditions of the surface of a neutron star in an experiment on earth, numerical simulations have proven to be a powerful tool to study X-ray bursts. Indeed, the combination of observational data, experiments, calculations from theory and numerical simulations can shed some light on the conditions at the surface of neutron stars.

The goal of this work is to include results from observations, theory and experiments into a numerical simulations and to study the dependence on various conditions at the surface of a neutron star. As the current picture of X-ray bursts and superbursts is not fully understood, we are aiming to analyze the connection between several parameters. Future work might constrain some of the parameters which influence burst ignitions and evolution at the surface of neutron stars. By understanding the links in the network of parameters, we will be able to use the new knowledge and put further constraints on the remaining unknowns.

In addition, the comprehension of how the X-ray bursts behave under various conditions will help us to predict how changes in the environment of a neutron star will influence the bursts. We will discuss in more details, how one could possibly achieve a superburst recurrence time of the order of a few years and which parameters would help to solve the puzzle of the superburst ignition.

In a first step, we will discuss the physics used in the simulations and the structure of the code which allows us to simulate X-ray bursts as well as superbursts in a reasonable time. In order to study the network of parameters, we will have a closer look at the following properties:

- Network size
- Crust heating
- Accretion rate
- Accretion composition

Variations of those parameters will influence indirectly the following X-ray burst ignition conditions:

- Heat conduction
- Composition of ashes

- Density
- Temperature
- Influences of previous X-ray bursts
- Convection

In order to limit the scale of this work, you should note that we disregard the variations in reaction rates, the influence of changes in the mass and radius of the underlying neutron star, changes in physical equations (e. g. equation of state, calculation of opacity,...) and different convection models. Additional future work might be done to complete the picture of free parameters influencing X-ray burst simulations.

As a conclusion: The ultimate goal of this current work is to get an understanding of the complexity of the physical parameters influencing X-ray bursts and superbursts ignition. We aim to link the results from simulations with observations, thereby putting further constraints on unknown parameters.

Chapter 2

Tools for Simulations of X-ray Bursts and Superbursts

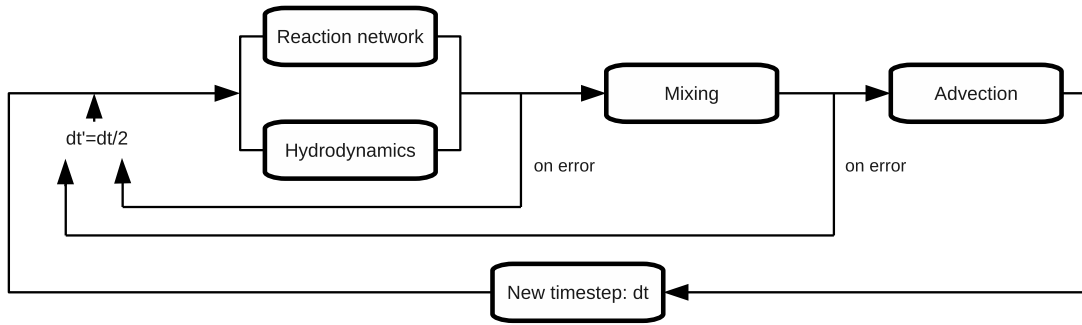


Fig. 2.1 Schematic view of the calculation procedure. The reaction network and the hydrodynamic parts are solved in parallel.

We model the surface layers of a neutron star using a general relativistic code. The code implicitly solves the hydrodynamic equations coupled with a nuclear reaction network (Hix and Thielemann, 1999) on a one-dimensional grid. The hydrodynamics part is based on a version of AGILE (Liebendoerfer et al., 2002) which has been modified for X-ray burst and superburst simulations. Convective mixing is taken into account by using the mixing length approximation.

In order to speed up the calculations, we use a new parallelized version of the code which makes use of OpenMP as well as MPI. Each new time step, the solution is divided into four submatrices, see Figure 2.1:

1. Nuclear reactions
2. Hydrodynamics and advection
3. Convective mixing and diffusion of composition
4. Advection of the composition

Due to the fact that the implicit scheme requires the inversion of the Jacobian matrix which is connected to the independent variables of a system of equations, we use the fast and efficient PARDISO solver (Schenk et al., 2001) both for the hydrodynamics as well as for the nuclear reaction network.

For a given time step dt , the hydrodynamic equations and the nuclear reaction network are solved in parallel. On error, the time step will be divided by a factor of two and the procedure is repeated until both the hydrodynamic and the nuclear network solvers succeed. The convection solver makes use of the mixing length theory and returns the convected isotopes. If the mixing procedure fails, the time step dt is divided by a factor of two and a new iteration is started. On success, a second order scheme performs the advection of the new composition.

In the following sections, we will describe each part of the code in more details.

2.1 Hydrodynamics

In a gravitationally dominated field the macroscopic motion of the matter is completely determined by the Einstein field equation(s)

$$G_{\mu\nu} = 8\pi T_{\mu\nu}, \quad (2.1)$$

where G is the Einstein curvature tensor and T is the stress-energy tensor.

In spherical symmetry the stress-energy tensor for an ideal fluid with radiation in co-moving coordinates is given by (Lindquist, 1966)

$$T^{tt} = \rho \left(1 - B(X) + e_{matter}/c^2 + e_{rad}/c^2 \right) \quad (2.2)$$

$$T^{ta} = T^{at} = q_{rad}/c \quad (2.3)$$

$$T^{aa} = p_{matter} + p_{rad} \quad (2.4)$$

$$T^{\theta\theta} = T^{\phi\phi} = p_{matter} + \frac{1}{2}(\rho e_{rad} - p_{rad}), \quad (2.5)$$

where $\rho = m_u n_u$ is the rest mass density and n_u is the baryon number density. Further, e_{matter} is the specific internal energy from the thermal motion of the nuclei and the electrons, $B(X) = -\sum X_j (m_j - A_j m_u) c^2 / (A_j m_u c^2)$ is the sum of the specific binding energies of the nuclei relative to ^{12}C . For a certain specie j , the mass excess energy is $(m_j - A_j m_u) c^2$, m_j is the atomic mass, A_j is the nucleon number and X_j is the fraction of nucleons of species j in a given volume relative to all nucleons in the volume. In the equations above, e_{rad} is the specific energy of radiation, q_{rad} is the first angular momentum, p_{rad} is the second angular momentum and p_{matter} is the matter pressure. Due to the short mean free path, thermal equilibrium is ensured over the entire layer for a certain depth. This means that the diffusion approximation is valid and both matter and radiation are in thermal equilibrium. Thus, the term q_{rad} becomes the radiation energy flux and $p_{rad} = \rho e_{rad}/3$ becomes the photon pressure, and hence we find

$$T^{tt} = \rho (1 + e/c^2) \quad (2.6)$$

$$T^{ta} = T^{at} = \rho/c \quad (2.7)$$

$$T^{\theta\theta} = T^{\phi\phi} = T^{aa} = p. \quad (2.8)$$

Here $p = p_{matter} + p_{rad}$ is the pressure and $e = e_{matter} - B(X_j)c^2 + e_{rad}$ is the specific energy. To solve the set of equations, we assume a spherically symmetric metric where the radial coordinate is represented by a and attached to comoving matter:

$$ds^2 = -\alpha^2 c^2 dt^2 + \left(\frac{1}{\Gamma} \frac{\partial r}{\partial a} \right)^2 da^2 + r^2 (d\theta^2 + \sin^2 \theta d\phi^2), \quad (2.9)$$

where r is the areal radius of the volume enclosing a and α is the proper time correction (redshift) of the coordinate time lapse dt of an observer following the motion of the matter attached to a as seen from infinity. Further, $\Gamma = \sqrt{1 + u^2/c^2 - 2Gm/rc^2}$ is a factor which in the special relativistic limit becomes the boost factor between the inertial system and the co-moving system. Here u is the matter velocity as seen from a frame of constant areal radius and m is the total gravitational mass contained within a radius r . The total gravitational mass is given by the sum of the rest mass, gravi-

tational energy, kinetic energy, heat energy and nuclear binding energy. You should note that in the static limit, Γ relates to the volume correction of the Schwarzschild metric.

Given the metric and the set of equation (2.6-2.8) Liebendörfer et al. (2001) solved the Einstein field equation (2.1) and derived a set of conservative equations for the dynamical motion. By adding nuclear and non-nuclear neutrino emission, one finds the following set of equations:

$$\frac{\partial}{c^2 \partial t} \left(\frac{1}{D} \right) = \frac{\partial}{\partial a} (4\pi r^2 \alpha u) \quad (2.10)$$

$$\frac{\partial \tau}{\partial t} = -\frac{\partial}{\partial a} (4\pi r^2 \alpha (up + \Gamma q)) - \Gamma \frac{\partial \epsilon}{\partial t} \quad (2.11)$$

$$\begin{aligned} \frac{\partial S}{\partial t} = & -\frac{\partial}{\partial a} (4\pi r^2 \alpha (\Gamma p + uq/c^2)) \\ & - \frac{\alpha}{r} \left(\left(1 + \frac{e}{c^2} + \frac{3p}{\rho c^2} \right) \frac{Gm}{r} + \frac{8\pi Gr^2}{\rho c^2} \left(p \left(1 + \frac{e}{c^2} \right) \rho - \frac{q^2}{c^4} \right) - \frac{2p}{\rho} \right) \end{aligned} \quad (2.12)$$

$$\frac{\partial V}{\partial a} = \frac{4\pi}{3} \frac{\partial r^3}{\partial a} = \frac{1}{D} \quad (2.13)$$

$$\frac{\partial m}{\partial a} = 1 + \tau/c^2 \quad (2.14)$$

$$\frac{\partial}{\partial t} \left(\frac{1}{4\pi r^2 c^4 \rho^2} q \right) = - \left(1 + e/c^2 \right) \frac{\partial \alpha}{\partial a} - \frac{1}{\rho c^2} \frac{\partial}{\partial a} (\alpha p), \quad (2.15)$$

where we have defined a specific rest mass density, a specific total energy density and a specific momentum density:

$$\frac{1}{D} = \frac{\Gamma}{\rho} \quad (2.16)$$

$$\tau = \Gamma e + \frac{2}{\Gamma + 1} \left(\frac{1}{2} u^2 - \frac{Gm}{r} \right) + \frac{uq}{\rho c^2} = \Gamma (c^2 + e) - c^2 + \frac{uq}{\rho c^2} \quad (2.17)$$

$$S = u \left(1 + e/c^2 \right) + \Gamma \frac{q}{\rho c^2} \quad (2.18)$$

The term $\partial \epsilon / \alpha \partial t$ describes the neutrino emission rate in the co-moving frame and includes neutrino emission due to weak reactions and neutrino emission via bremsstrahlung

which is calculated using the formulation of Schinder et al. (1987).

Introducing an adaptive grid equation (see below), results in one independent variable t and 7 dependent variables, namely: a, r, u, m, ρ, T and α which are determined using the set of equations (2.10-2.15) and one grid equation. However, the hydrodynamics is sensitive to the efficient convective heat transport which depends on the physical transport of the composition. By the reason that the physical transport of the composition is held constant during one hydrodynamics time step because of the operator split method, one has to consider three additional equations with three additional variables:

$$\frac{\partial \Gamma Y_e}{\partial t} = -\frac{\partial}{\partial a} \left(4\pi r^2 \rho \alpha \Gamma \left(-4\pi r^2 \rho D \frac{\partial}{\alpha \partial a} (\alpha Y_e) \right) \right) \quad (2.19)$$

$$\frac{\partial \mu^{-1}}{\partial t} = -\frac{\partial}{\partial a} \left(4\pi r^2 \rho \alpha \Gamma \left(-4\pi r^2 \rho D \frac{\partial}{\alpha \partial a} (\alpha \mu^{-1}) \right) \right) \quad (2.20)$$

$$\frac{\partial \Gamma Y_{e^2}}{\partial t} = -\frac{\partial}{\partial a} \left(4\pi r^2 \rho \alpha \Gamma \left(-4\pi r^2 \rho D \frac{\partial}{\alpha \partial a} (\alpha Y_{e^2}) \right) \right), \quad (2.21)$$

where $Y_e = \sum X_j Z_j / A_j$ is the electron abundance, $Y_{e^2} = \sum X_j Z_j^2 / A_j$ is the second moment of the electron abundance and $\mu^{-1} = Y_e + \sum X_j / A_j$ is the mean molecular weight.

The set of equations (2.10-2.15) together with the grid equation and the equations (2.19-2.21) define the hydrodynamics and are solved each new time step using the Newton-Raphson method (Press et al., 1992)

$$\delta y = \left(\frac{\partial f}{\partial y} \right)^{-1} y, \quad (2.22)$$

where y is the array containing the hydrodynamical variables. Using the PARDISO solver (Schenk et al., 2001), the hydrodynamics is solved each time step by deriving the solution of a $10n \times 10n$ submatrix equation with n being the number of grid points.

2.1.1 Equation of state

Explosive burning resulting in a type I X-ray burst occurs in the atmosphere respectively ocean of a neutron star. At this depth, the accreted atoms are assumed to be fully ionized and the abundance of the electrons is set by the composition. We calculate the electron contribution to the pressure and internal energy by assuming an arbitrarily relativistic and arbitrarily degenerate gas. As an approximation, the

baryon contribution can be described as an ideal gas. The photons are assumed to be in a local thermodynamical equilibrium since the mean free path is short.

All those features are contained in K. Nomoto's EOS code, and hence we adopt it for our X-ray burst. A further useful advantage of K. Nomoto's EOS code is that it is very fast. It returns the pressure p and the internal energy e as a function of mass density ρ , temperature T , electron abundance Y_e , the second order momentum of the electron abundance Y_{e^2} and the mean molecular weight μ^{-1} .

2.1.2 Heat Transport

The total heat transport is given by

$$q = q_\gamma + q_c, \quad (2.23)$$

where q_γ is the radiative/conductive heat transport and q_c is the convective heat transport. In the following, we will describe two options of heat transport in more details.

Heat Transport by Convection

To determine whether convection occurs in a system, one can analyze a blob of matter. This blob in the stellar environment is convectively stable iff both the Schwarzschild and Ledoux criterium hold:

$$\left(\frac{d \ln T}{d \ln P} \right)_s \leq \left(\frac{d \ln T}{d \ln P} \right)_{blob} - \sum_{x \in \{Y_e, Y_e^2, \mu^{-1}\}} \frac{\chi_x}{\chi_T} \left(\frac{d \ln x}{d \ln P} \right)_s, \quad (2.24)$$

where the index 's' accounts for a derivative in the stellar profile and

$$\chi_x = \left(\frac{\partial \ln P}{\partial \ln x} \right)_{\{Y_e, Y_e^2, \mu^{-1}\} \setminus x}, \quad (2.25)$$

where x may be any of the state-variables $\{Y_e, Y_e^2, \mu^{-1}\}$ and the other variables fixed. Further, the sum in equation (2.24) describes the Ledoux criterium and determines the compositional gradients in the stellar profile.

During a burst, the thermonuclear runaway causes a steep temperature gradient which does not satisfy equation (2.24) and therefore produces convective blobs. Such blobs of matter travel a given mixing length Λ until they dissolve and release heat. In fact,

this kind of heat transport is much more efficient than radiative or conductive heat transport. The convective heat flux q_c can be calculated using the formula of Thorne (1977):

$$q_c = \frac{1}{2} c_p \bar{v} \rho \Lambda \Gamma \left(\left. \frac{dT}{dr} \right|_s - \left. \frac{dT}{dr} \right|_{blob} \right), \quad (2.26)$$

with $\Gamma = \sqrt{1 + u^2/c^2 - 2Gm/rc^2}$, c_p and \bar{v} being the specific heat capacity respectively the average velocity of rising or descending blobs. By the reason that the energy of the matter is much larger than the energy arising due to pressure, we calculate the convection in the Newtonian limit and therefore assume $\Gamma \approx 1$ during our simulations. The average velocity \bar{v} can be obtained by using the following relation (Thorne, 1977):

$$\bar{v}^2 = \frac{1}{8} \frac{Gm}{r^2} \Lambda^2 Q \frac{1}{T} \left(\left. \frac{dT}{dr} \right|_s - \left. \frac{dT}{dr} \right|_{blob} \right), \quad (2.27)$$

with

$$Q = - \left(\frac{\partial \ln \rho}{\partial \ln T} \right)_{P, Y_e, Y_e^2, \mu^{-1}} \quad (2.28)$$

Note that the square of the average velocity \bar{v} is always positive during convection.

Heat Transport by Conduction and Radiation

At the surface of an accreting neutron star, the mean free path of photons and electrons is very short and hence, many collisions occur traversing the width of our model. This means that the electrons and photons are in a local thermodynamical equilibrium and therefore, heat transport follows Fourier's law and Fick's law. The relativistic transport equation for such a spherical symmetric system is given by (Lindquist, 1966)

$$\frac{q_\gamma}{c} r^2 \left(\frac{1}{\Gamma} \frac{\partial r}{\partial a} \right)^2 + \frac{1}{\rho \kappa} \frac{1}{\alpha} \frac{\partial}{\partial t} \left(\frac{q_\gamma}{c} r^2 \left(\frac{1}{\Gamma} \frac{\partial r}{\partial a} \right)^2 \right) = - \frac{4a_{rad} c}{3} \frac{r^2}{\kappa \rho} \left(\frac{1}{\Gamma} \frac{\partial r}{\partial a} \right) T^3 \frac{\partial}{\partial a} (\alpha T), \quad (2.29)$$

where κ is the opacity, L is the luminosity and q_γ is the heat flux by conduction and radiation. Using $\frac{\partial r}{\partial a} = \frac{\Gamma}{4\pi r^2 \rho}$ one finds

$$q_\gamma + \frac{(4\pi r^2 \rho^2)^2}{r^2} \frac{1}{\kappa \rho} \frac{\partial}{\partial t} \left(q_\gamma \frac{r^2}{(4\pi r^2 \rho^2)^2} \right) = - \frac{4a_{rad} c}{3} \frac{\Gamma}{\kappa \rho} T^3 \frac{\partial}{\partial r} (\alpha T). \quad (2.30)$$

The mean free path of the bursting region is given by $l = (\kappa \rho)^{-1} \sim 10^{-1} \text{cm}$ which is much shorter than the distance a photon can travel during the proper rise time of the

luminosity. Hence, we can neglect the time-dependent term

$$q_\gamma = -\frac{4a_{\text{rad}}c}{3} \frac{T^3}{\kappa\rho} \Gamma \frac{\partial}{\alpha\partial r} (\alpha T). \quad (2.31)$$

Applying again $\frac{\partial r}{\partial a} = \frac{\Gamma}{4\pi r^2 \rho}$, the formula reduces to

$$q_\gamma = -\frac{16\pi a_{\text{rad}}c}{3} \frac{T^3}{\kappa} r^2 \frac{\partial}{\alpha\partial a} (\alpha T). \quad (2.32)$$

Given the luminosity, the temperature gradient is directly proportional to the opacity of the matter. Since the opacity depends on the composition, temperature and density, we need to calculate the opacity accurately as it determines the relation between density and temperature in our model.

The most important contributions to the opacity in the upper atmosphere of a neutron star are the electron scattering and the free-free absorption. In deeper layers, what means in the lower atmosphere and ocean, the matter is degenerate and electron conductivity dominates. The electron conductivity can be described by electron-electron and electron-ion scattering. At the ignition region of superburst, the interaction of electrons with phonons and impurities becomes important.

In the upper atmosphere, electron scattering dominates and defines the Eddington limiting luminosity. We use the approximation of Paczynski (1983) and extend the formulation to an arbitrary composition:

$$\kappa_{es} = \frac{\kappa_0}{(1.0 + 2.7 \cdot 10^{11} \rho / T^2) \left(1.0 + (T / 4.5 \cdot 10^8)^{0.86}\right)}, \quad (2.33)$$

where

$$\kappa_0 = \frac{8\pi}{3} \left(\frac{e^2}{m_e c^2} \right)^2 \frac{1}{m_u} \sum_i \frac{Z_i}{A_i} X_i \quad (2.34)$$

is the Thomson scattering cross section for a certain composition assuming fully ionized matter. Further, ρ is the mass density, T is the temperature, m_e is the electron mass, m_u is the unit mass, e is the electron charge and c the speed of light. The quantities A_i , Z_i and X_i are the nucleon number, proton number and mass fraction respectively. To handle the free-free opacity κ_{ff} , we use the model from Schatz et al. (2013). The total radiative opacity κ_r can be presented by using the approximation of Potekhin and Yakovlev (2001)

$$\kappa_r = (\kappa_{ff} + \kappa_{es}) A(f, T), \quad (2.35)$$

where

$$A(f, T) = 1 + \frac{1.097 + 0.777T_{Ry}}{1 + 0.536T_{Ry}} \left(\frac{\kappa_{ff}}{\kappa_{ff} + \kappa_{es}} \right)^{0.617} \left(1 - \frac{\kappa_{ff}}{\kappa_{ff} + \kappa_{es}} \right)^{0.77}. \quad (2.36)$$

Here, $T_{Ry} = T/(0.15782 \cdot 10^6 \cdot Z)$ with Z being the mean charge number.

On the other hand, the thermal conduction is assigned by a conductive opacity (Urpin and Yakovlev, 1980)

$$\kappa_t = \frac{4acT^2 m_\star}{\pi k_B^2 \rho n_e} \nu_c, \quad (2.37)$$

where m_\star is defined by the electron Fermi energy $E_F = (m_\star - m_e)c^2$ and $\nu_c = \nu_{ee} + \nu_{ei} + \nu_{ep} + \nu_{eim}$ is the collision frequency due to electron interactions with other electrons, ions, phonons or impurities respectively. To handle the electron-ion scattering, we use the results of Urpin and Yakovlev (1980) generalized with the description of Schatz et al. (2013). The electron-electron scattering is included by implementing the expressions given in Potekhin et al. (1997). In deeper layers, electron-phonon collisions are considered using the formulation of Baiko and Yakovlev (1995) and electron-impurity scattering are implemented with the formulation of Schatz et al. (2013).

Finally, the total opacity is given by the harmonic sum

$$\kappa^{-1} = \kappa_r^{-1} + \kappa_t^{-1} \quad (2.38)$$

Typically, the radiative conduction dominates in the outer layers of a neutron star where matter is non-degenerate, whereas the thermal conductivity is important in deeper and strongly degenerate layers.

2.1.3 Adaptive Grid

To resolve correctly thermonuclear runaway in thin shells of the order of $10^{-16}M_\odot$ as well as the advection of ashes at very high densities in thick shells of the order of $10^{-9}M_\odot$, one needs to use a grid discretization which can handle zone variables differing over many orders of magnitude. We use the adaptive grid of AGILE (Liebendoerfer et al., 2002) with modifications for XRB and superburst simulations. To understand why the original grid of AGILE is not appropriate for our purpose, we will have a look at the discretization of the Poisson equation

$$m_{i+1}^{t+\Delta t} - m_i^{t+\Delta t} = \Gamma_{i'}^{t+\Delta t} \left(1 + \frac{e_{i'}^{t+\Delta t}}{c^2} \right) da_{i'}^{t+\Delta t}. \quad (2.39)$$

where $\Gamma_{i'}^{t+\Delta t} = \sqrt{1 + \left(u_i^{t+\Delta t}/c \right)^2 + 2Gm_i^{t+\Delta t}/r_i^{t+\Delta t}c^2}$, $e_{i'}^{t+\Delta t}$ is the internal energy of a zone, $m_i^{t+\Delta t}$ is the total gravitational mass inside the gravitational radius, $r_i^{t+\Delta t}$, and $da_{i'}^{t+\Delta t} = a_{i+1}^{t+\Delta t} - a_i^{t+\Delta t}$ is the rest mass of a zone. All variables with primed indices are defined on the center-grid while variables with unprimed indices are defined on the edge-grid. The adaptive grid is evaluated with double precision, what means the numerics yields a maximum of 15 decimals of precision. Unfortunately, this will not suffice to resolve thin shells at the surface of the neutron star. Indeed, the terms $m_{i+1}^{t+\Delta t} - m_i^{t+\Delta t}$ and $da_{i'}^{t+\Delta t} = a_{i+1}^{t+\Delta t} - a_i^{t+\Delta t}$ cause problems: Two large numbers are subtracted resulting in a number which is several orders of magnitude smaller.

To illustrate the problem, one can have a look at a common used term during the calculation of the adaptive grid is for example the difference in radius: $r_{i+1}^{t+\Delta t} - r_i^{t+\Delta t}$. At the surface, r is of the order 10^6 cm, while the width of one zone may be a few cm. Hence, the inclusion of both thick and thin shells suggests that it is not advisable to use the original discretization of AGILE.

To improve the adaptive grid for X-ray burst and superburst calculations, one can use the following expressions for the vectors:

$$m_i^{t+\Delta t} = m_i^t + \Delta m_i^{t+\Delta t} \quad (2.40)$$

$$r_i^{t+\Delta t} = r_i^t + \Delta r_i^{t+\Delta t} \quad (2.41)$$

$$da_i^{t+\Delta t} = da_i^t + \Delta da_i^{t+\Delta t} - \Delta da_i^{t+\Delta t} \quad (2.42)$$

Substituting these relations into equation 2.39 results in

$$\left(m_{i+1}^t - m_i^t \right) + \left(\Delta m_{i+1}^{t+\Delta t} - \Delta m_i^{t+\Delta t} \right) = \Gamma_{i'} \left(1 + \frac{e_{i'}}{c^2} \right) \left(da_i^t + \Delta a_{i+1}^{t+\Delta t} - \Delta a_i^{t+\Delta t} \right). \quad (2.43)$$

You should note that for a certain time step, the expression $\left(m_{i+1}^t - m_i^t \right)$ results in a small constant number comparable to $\Delta m_i^{t+\Delta t}$. That means that $\Delta m_i^{t+\Delta t}$ becomes a new independent variable. $\Delta a_i^{t+\Delta t}$, $\Delta m_i^{t+\Delta t}$ and $\Delta r_i^{t+\Delta t}$ are the so-called shift vectors.

As a further advantage, accretion is easily handled by setting

$$\Delta da_i^{t+\Delta t} = \dot{M} dt \quad \text{for all } i, \quad (2.44)$$

in case of using outflow boundary conditions (total mass of the model is constant), respectively

$$\Delta da_i^{t+\Delta t} = \dot{M} dt \frac{\rho_i^3}{\sum_i \rho_i^3} \quad \text{for all } i, \quad (2.45)$$

in case of accretion boundary conditions. However, you should note that such a choice of grid does include numerical diffusion of the composition.

Essentially, each time step, the grid variables are set by the definition of the baryonic mass difference between two adjoined zones. Instead of applying either equation (2.44) or (2.45) to define the grid cells, we have a third and robust method which will be described in the following section.

2.1.4 Adaptive Grid Modification

As described in the previous section, we have rewritten the original version of the adaptive grid in AGILE in forms of shift vectors in order to handle the extrem variable ranges. By defining the baryonic mass difference between two adjoined zones for a given time step, we can interpolate the new grid point locations. X-ray bursts occur at densities of the order of 10^6g/cm^3 whereas superburst are thought to ignite at densities of 10^9g/cm^3 (Gupta et al., 2007). To maintain both an accurate simulation of thousands of X-ray bursts and a possible ignition of a superburst, one needs to choose the locations of the grid cells cautiously.

To derive the description of our current version of the adaptive grid, let $N_i = \Delta a_i$ be the mass of zone i and $n_i = a_i^{t+\Delta t} - a_{i-1}^{t+\Delta t}$ be the mass which is advected into zone i during a time step Δt . You should note that both variables have the units of mass per zone. Let further k be a constant, introducing the logarithmic series $X_i = k^i$, and set $\hat{N}_i = N_i/X_i$ respectively $\hat{n}_i = n_i/X_i$. The aim of our new version of the adaptive grid is to find a logarithmic mass zone distribution.

We further introduce another useful term

$$R_i^{grid} = \left(\sqrt{1 + \sum_j \left(w_j \frac{N_{scale}}{F_{scale}^j} \frac{f_i^j - f_{i-1}^j}{N_i} \right)^2} \right)^{-1}, \quad (2.46)$$

where the sum is over all other independent variables, w_j is a weight factor which determines the significance of a certain variable, N_{scale} and F_{scale} are overall scales for the independent variables, and f_i^j is the actual value of the variable j at grid point i . In a next step, we normalize the variable R_i^{grid} :

$$\hat{R}_i^{grid} = \frac{|R_i^{grid}|}{\max_i (|R_i^{grid}|)} \quad (2.47)$$

In addition, the desired resolution of the adaptive grid R_i is linked to the old resolution by

$$R_i = (1 - sloth) \hat{R}_i^{grid} + sloth \frac{\max_i (\hat{N}_i X_i)}{\hat{N}_i}, \quad (2.48)$$

where the variable *sloth* determines how the resolutions are mixed. In our simulations, we use $sloth = \exp(-dt/0.1)$, where dt is the time step and 0.1 is a chosen parameter. This ensures that in cases of large time steps, the desired resolution will determine how the grid moves since *sloth* is small. On the other side, short time steps will maintain the old grid spacing.

Finally, the adaptive grid equation results in

$$0 = (\hat{N}_{i+1} R_{i+1} - \hat{N}_i R_i) + (\hat{n}_{i+1} R_{i+1} - \hat{n}_i R_i), \quad (2.49)$$

where the first parenthesis contain constant large terms, while the second parenthesis settle how the grid points are moving. If the value of the first parenthesis is zero, then the current resolution is the desired resolution, and hence, the grid points will not move. By maintaining a logarithmic profile of the grid, we automatically advect the accreted mass downwards. In other words, the adaptive grid modification will be appropriate for outflow as well as for accretion boundary conditions.

2.1.5 Boundary Conditions

In order to solve the system of equations, one needs to set the boundary values. Implementing correct values at the boundaries is crucial and will greatly influence the outcome of a simulation. Concerning the surface boundaries, a precise and detailed description of the photosphere is sophisticated very difficult to implement. Therefore, we determine surface temperature using a crude but accurate radiative zero photosphere model which will be discussed in the following:

Assuming hydrostatic equilibrium, the pressure of the neutron star can be described by the Tolman-Oppenheimer-Volkoff equation (Oppenheimer and Volkoff, 1939)

$$\frac{\partial P}{\partial r} = \frac{-GM\rho \cdot \left(1 + \frac{P}{\rho c^2}\right) \cdot \left(1 + \frac{4\pi r^3 P}{Mc^2}\right)}{r^2 \left(1 - \frac{2GM}{rc^2}\right)}, \quad (2.50)$$

where P is the pressure, r is the radius, G is the gravitational constant, M is the gravitational mass, c is the speed of light and ρ is the density of the rest mass. Due to the fact that the energy density of the pressure is very low in the photosphere compared to the rest mass density, we can simplify the equation above:

$$\frac{\partial P}{\partial r} = \frac{-GM\rho}{r^2 \left(1 - \frac{2GM}{rc^2}\right)}. \quad (2.51)$$

Further, the temperature is given by (Glen and Sutherland, 1980)

$$\frac{d}{dr} (Te^\phi) = \frac{-3\kappa\rho L_\gamma e^\phi}{16\pi acT^3 r^2 \sqrt{1 - \frac{2GM}{c^2 r}}}, \quad (2.52)$$

where T is the temperature, e^ϕ is the red shift correction factor, κ is the opacity, L_γ is the photon luminosity and a is the radiation. The gravitational field is approximately constant over the width of the photosphere and hence the red shift correction factor e^ϕ can be divided out:

$$\frac{\partial T}{\partial r} = \frac{-3\kappa\rho L_\gamma}{16\pi acT^3 r^2 \sqrt{1 - \frac{2GM}{c^2 r}}}. \quad (2.53)$$

Combining equation (2.51) with (2.53), we find

$$\frac{\partial P}{\partial T} = \frac{16\pi GacMT^3}{3\kappa L_\gamma \sqrt{1 - \frac{2GM}{c^2 r}}}. \quad (2.54)$$

Assuming that the release of nuclear energy is negligible over the width of the photosphere, the luminosity L_γ is constant. For a given pressure P_0 in the photosphere, we can find the corresponding temperature T_0 . Using those starting values, we can solve the differential equation with use of a forth order Runge-Kutta solver down to a certain surface pressure P_{surf} which will provide us the temperature T_{surf} at the boundary of our model. In order to speed up the calculations, we neglect the conductivity during the evaluation of the opacity. This leads to an error of the order of 0.1%

in the opacity at the boundary of our model.

One of the major advantages of using our photosphere model is that we gain speed by neglecting the nuclear reactions and convection. However, one of the drawbacks is that we are not able to study bursts with peak luminosity at the Eddington limiting luminosity of the neutron star atmosphere. Such a scenario is violating the assumptions of our model and will require a sophisticated replacement employing wind and transport equations.

Besides the temperature at the surface of a model, we need further boundary conditions to solve the system of equations. In general, to simulate the outer layers of a neutron star, we provide two different models:

Outflow Boundary Conditions: Each new time step, the same amount of accreted mass at the surface of the model will advect at zero Lagrangian velocity into the outermost ghost zone in order to keep the total mass of the model constant:

$$\Delta da_{nq}^{t+\Delta t} = \dot{M}\Delta t = \Delta da_1^{t+\Delta t} \quad (2.55)$$

Further, at the inner boundary we take use of von Neumann boundary conditions to constrain the temperature, density and lapse function. Heating from the layers below the range of our model is included as a boundary luminosity L_1 .

At the surface, the lapse function is set to match the Schwarzschild solution, whereas the surface pressure is set by Dirichlet boundary conditions. The surface temperature is determined by a radiative zero boundary condition (see above).

Accretion Boundary Conditions: Using accretion boundary conditions, we are able to increase the total mass contained in our model. The increase of mass is handled by

$$\Delta da_{nq}^{t+\Delta t} = \dot{M}\Delta t \quad \text{and} \quad \Delta da_1^{t+\Delta t} = 0. \quad (2.56)$$

As an approximations, the pressure and thereby the density are determined by a static Tolman-Oppenheimer-Volkoff equation (Oppenheimer and Volkoff 1939

((Oppenheimer and Volkoff, 1939)) at the inner boundary:

$$\frac{\partial P}{\partial r} = \frac{-GM\rho \cdot \left(1 + \frac{P}{\rho c^2}\right) \cdot \left(1 + \frac{4\pi r^3 P}{Mc^2}\right)}{r^2 \left(1 - \frac{2GM}{rc^2}\right)} \quad (2.57)$$

The temperature at the inner boundary is calculated using the equation of thermal balance:

$$C(T) \frac{\partial T}{\partial t} = -L_\gamma^\infty + L_{acc}^\infty - L_\nu^\infty, \quad (2.58)$$

where $C(T)$ is temperature-dependent the heat capacity, L_γ^∞ is the redshifted luminosity at the inner boundary containing heating from the layers below, L_{acc}^∞ is the accretion luminosity as seen from infinity and L_ν^∞ is the redshifted luminosity accounting for neutrino cooling.

The surface temperature is determined by a radiative zero boundary condition. Further, the lapse function is controlled by Dirichlet boundary conditions at the surface (matching the Schwarzschild solution) and von Neumann conditions at the inner boundary.

In general, we use accretion boundary conditions to generate an initial model and outflow boundary conditions for X-ray burst simulations.

2.2 Nuclear Reaction Network

The reaction network defines the nuclear transmutations of the isotopes in the composition. Each iteration, we solve for every isotope i the reaction equation given by

$$\frac{\partial Y_i}{\alpha \partial t} = \sum_j N_j^i \lambda_j Y_j + \sum_{j,k} N_{j,k}^i \rho N_A \langle j, k \rangle Y_j Y_k + \sum_{j,k,l} N_{j,k,l}^i \rho^2 N_A^2 \langle j, k, l \rangle Y_j Y_k Y_l, \quad (2.59)$$

where $Y_i = n_i/(\rho N_A)$ is the nuclear abundance of an isotope i , n_i is the number density and ρ is the rest mass density. Further, $N_j^i = N_i$, $N_{j,k}^i = N_i/(N_j!N_k!)$ and $N_{j,k,l}^i = N_i/(N_j!N_k!N_l!)$, where N_i is either a positive or a negative integer, describing the number of particles of type i that are created respectively annihilated in the reaction. In order to avoid double counting in the sums, one needs to divide N_i by factorials.

The quantities λ_j , $N_A \langle j, k \rangle$ and $N_A^2 \langle j, k, l \rangle$ in equation (2.59) describe the so-called thermonuclear reaction rates (Fowler et al., 1967). There are three possible types of reactions:

Single particle reaction: Photodisintegration, β -decay, electron or positron capture, neutrino-induced reaction.

Two particle reaction: Proton capture or α capture

Three particle reaction: Triple- α process

In this work, we try to analyze the rp-process and its ashes using two different networks: a 304 isotopes network (see table 2.1) and a 561 isotopes network (see Table 2.2). The particle reactions are taken from REACLIB (Cyburt et al., 2010), the weak reaction rates up to $Z = 32$ are taken Fuller et al. (1980) and Langanke et al. (2001). As there is only a small fraction of material processed above $Z = 32$, we can ignore neutrino losses from heavier isotopes (Schatz et al., 1999), and hence reduce the size of the network.

Solving the set of numerical equations (2.59) results in a change of the composition and therefore a change in the total binding energy of the matter. In addition, neutrino emissions may lead to a change in energy. To include both the change of binding energy and the neutrino emission, as well as the neutrino bremsstrahlung in our hydrodynamical calculations, we need to correct the specific energy as follows

$$e \longrightarrow e - \sum_j N_A \dot{Y}_j B_j + \sum_{weak} N_A \dot{Y}_i E_{\nu i} + e_{bremsstrahlung}, \quad (2.60)$$

where B_j is the binding energy of an isotope j with proton number Z and neutron number N :

$$B_j = (Nm_n + Zm_p - m_j) c^2, \quad (2.61)$$

with m_j being the actual mass of the isotope j . The quantity $E_{\nu i}$ in the second term is the specific energy loss from the neutrino emission due to the i th weak interaction. The last term in equation (2.60) corresponds to the fraction of energy loss via neutrino emission due to neutrino bremsstrahlung. Using the formulation Schinder et al. (1987), we calculate the loss from pair, photo and plasma neutrino emission.

As the nuclear network is calculated separately, an isotope in a zone can not react with another isotope from the neighbouring cell. Therefore, convective mixing and advection should be included in the numerical calculation to enable reaction taking place over a wider range of zones.

Z	A	Z	A
n	1	Co	51-57
H	1-3	Ni	52-62
He	3-4	Cu	54-63
Li	7	Zn	55-66
Be	7-8	Ga	59-67
B	8, 11	Ge	60-68
C	9-10, 12	As	64-69
N	12-15	Se	65-72
O	13-18	Br	68-73
F	17-19	Kr	69-74
Ne	18-21	Rb	73-77
Na	20-23	Sr	74-78
Mg	21-25	Y	77-82
Al	22-27	Zr	78-83
Si	24-30	Nb	81-85
P	26-31	Mo	82-86
S	27-34	Tc	85-88
Cl	30-35	Ru	86-91
Ar	31-38	Rh	89-93
K	35-39	Pd	90-94
Ca	36-44	Ag	94-98
Sc	39-45	Cd	95-99
Ti	40-47	In	98-104
V	43-49	Sn	99-105
Cr	44-52	Sb	106
Mn	47-53	Te	107
Fe	48-56		

Table 2.1 The table lists all the isotopes which are used in the calculations with the 304 isotope network. The network of the isotopes is described in Fisker et al. (2006).

Z	A	Z	A
n	1	Co	50-59
H	1-3	Ni	50-62
He	3-4	Cu	55-65
Li	7	Zn	55-66
Be	7-9	Ga	60-71
B	8,10,11	Ge	60-74
C	9-13, 12	As	60-69
N	12-15	Se	65-80
O	13-18	Br	70-81
F	17-19	Kr	69-84
Ne	17-22	Rb	74-85
Na	20-23	Sr	73-88
Mg	20-26	Y	77-89
Al	22-27	Zr	78-92
Si	22-30	Nb	81-93
P	26-31	Mo	82-97
S	27-34	Tc	85-97
Cl	31-35	Ru	86-102
Ar	31-38	Rh	89-103
K	35-39	Pd	90-108
Ca	35-44	Ag	94-109
Sc	40-45	Cd	95-112
Ti	39-49	In	98-113
V	43-51	Sn	99-120
Cr	43-54	Sb	104-121
Mn	47-53	Te	104-126
Fe	46-58		

Table 2.2 The table lists all the isotopes which are used in the calculations with the 561 isotope network. We adopted the list of isotopes from Reichert (2013), private communication.

2.3 Convective Mixing

Spherical symmetric simulations rule out the occurrence of convective mixing, as convection is a multi-dimension phenomenon. Heat transport by convection is calculated during a hydrodynamics timestep. To complete the convection, one must also consider convective mixing of the composition.

We include therefore convective mixing of the isotopes by implementing the mixing length theory (Cox, 1968). In our present version of the code, we include the Schwarzschild-Ledoux instability criterium.

The convective mixing is described by a relativistic version of the Lagrangian time-dependent diffusion equation of Langer et al. (1985)

$$\frac{\partial \Gamma X_i}{\partial t} = \frac{\partial}{\partial a} \left(4\pi r^2 \rho \alpha \Gamma \left(4\pi r^2 \rho D \frac{\partial}{\partial a} (\alpha X_i) \right) \right), \quad (2.62)$$

where $D = \bar{v}\Lambda/3$ is the diffusion constant. Convective mixing plays a key role in the simulated surface region of the neutron star since the turnover timescale $\tau \sim \Lambda/\bar{v}$ is much shorter than the nuclear timescale.

2.3.1 Weakness of Mixing Length Theory

The convection at the surface of a neutron star plays an important role for the ignition conditions of XRBs and superbursts. However, one dimensional models are not able to reproduce correctly the convection and thus, one has to apply an approximated mixing which accounts for the missing convection. The mixing length theory is the most established model for one dimensional convection. But it has also two major drawbacks in the application of XRB and superburst simulations:

- The mixing length Λ is not known ab initio, but in non-degenerate regime it is reasonable to say that Λ is on the order of the pressure scale height, as bubbles will expand and diffuse into each other and dissolve after traveling about such a distance (Shu, 1991). However, in degenerate regions of the neutron star surface, the pressure scale height is around 5 to 10 meters, and hence much higher than the height of the convective zone. Such conditions violate the basic assumption of the mixing length theory which states obviously that the mixing length Λ (convective turnover) can not be bigger than the convective zone itself. In our study, we ignore this fact and apply a fixed mixing length Λ of 1 cm.

- The mixing length theory was developed for hydrostatic atmospheres and assumes that heat transporting turbulences are either on or off depending on the Schwarzschild-Ledoux criterium (2.24) whereas in a dynamical situation the turbulent region develops or decays over a period of time. One way to reduce this problems is to implement secular instabilities. Those instabilities occur when a blob of matter is stable against convection by the Schwarzschild-Ledoux criterium, though not satisfying the Schwarzschild equation alone. In other words, a region becomes semi-convective if the first part of equation (2.24) is violated:

$$\left(\frac{d \ln T}{d \ln P}\right)_{blob} \leq \left(\frac{d \ln T}{d \ln P}\right)_s \leq \left(\frac{d \ln T}{d \ln P}\right)_{blob} - \sum_{x \in \{Y_e, Y_e^2, \mu^{-1}\}} \frac{\chi_x}{\chi_T} \left(\frac{d \ln x}{d \ln P}\right)_s. \quad (2.63)$$

Secular instabilities, such as semi-convection, are not implemented in our code, since they would seriously slow down our calculations. In addition, we assume that the semi-convections are negligible at accretion rates which are used in our current simulations, see below.

Despite the problems of using the mixing length theory in our simulations, we leave the implementation of a more advanced time-dependent convection theory for future works.

2.4 Advection of the composition

The ignition conditions for the X-ray burst and superburst are very sensitive to the composition. In other words, our model is sensitive to numerical diffusion of the advection of the accreted composition. The adaptive grid handles properly the advection of all intensive variables based on the motion of the grid variable a . After the hydrodynamical calculation, one needs to apply a corresponding advection of X before completing a timestep. The current version of our code uses a conservative formulation of second order that calculates the isotope flux at the zone edges based on an upwind total variation diminishing scheme. This scheme is further based on a Van Leer limiter.

2.5 A short comparison with the MESA and KEPLER

Besides the numerical code we use in the current work, there are further one-dimensional tools available which are able to handle dynamically X-ray bursts and superburst simulations. The most established numerical one-dimensional tools for simulations of explosive runaway at the surface of a neutron star are the MESA code (Paxton et al., 2011, 2013) and the KEPLER code (Weaver and Woosley, 1978). Both codes are implicit and include a hydrodynamics solver linked with a nuclear network calculation. The advantage of using MESA and the KEPLER code is that a rather large community is testing and trying to improve the codes which makes them more reliable. Especially the MESA code, which is an open source code, has a large increase of popularity for X-ray bursts calculations while the KEPLER code is still limited to a certain number of users. Our code has only been used by a very small number of users and might be exposed to numerical errors or bugs.

A further advantage of the MESA and KEPLER tools is the detailed description of convection. While MESA and KEPLER compute semi-convections, it is not included in our current calculations.

The advantage of our code is that it is in general very fast since it makes use of MPI and OpenMP. The parallelization enable simulations with large network as well as a large number of grid cells withing a reasonalbe time frame. In addition, the use of a simplified convection model makes sure that not too much time spend on the calculation of the mixing of matter.

In contrast to the MESA and KEPLER code, we use a general relativistic description which is thought to be important at the surface of neutron stars. Togehter with the ability of the use of an adaptive grid makes our code very relevant in the study of X-ray bursts and superbursts.

Chapter 3

Nuclear Network Test

In this chapter, we discuss the initial model of X-ray burst simulations. In order to verify the reduced network used in our calculations, we explore the reaction flow of explosive burning with two different network sizes. The use of a small network size will be a key essence to simulate the self-consistent ignition of a superburst in an adequate simulation time.

3.1 Initial Model

The initial X-ray burst model contains a total mass of $4.7 \cdot 10^{22}$ g within a radius of the order of 10 m. The underlying neutron star has a radius of 11.2 km and a mass of $1.41 M_{\odot}$ which is included in our calculations as a fixed inner boundary conditions. We accrete solar composition with a constant accretion rate \dot{M}_{acc} of $1 \cdot 10^{17}$ g/s as observed from infinity. The accretion rate is equivalent to

$$\dot{M}_{acc}^0 = (1 + z) \dot{M}_{acc}, \quad (3.1)$$

where \dot{M}_{acc}^0 is accretion rate in the local proper frame at the surface and

$$1 + z = \frac{1}{\sqrt{1 - \frac{2GM}{Rc^2}}}, \quad (3.2)$$

is the redshift. Further, G is the gravitational constant, M is the mass included in our model plus the mass of the underlying neutron star and R is the total radius and c is the speed of light. Since the MESA code (Paxton et al., 2011, 2013) and KEPLER code (Weaver and Woosley, 1978) are based on a Newtonian description, one would

need to apply an accretion rate of $\dot{M}_{acc}^0 = (1+z) \dot{M}_{acc}^\infty = 1.3 \cdot 10^{17}$ g/s to compare the Newtonian solutions with the result of our general relativistic solver (Fisker et al., 2008; Keek and Heger, 2011).

In the field of X-ray burst observations, the accretion rate is often described in terms of the Eddington critical accretion rate

$$\dot{M}_{edd} = \frac{4\pi GM}{c\kappa_0\eta} \quad (3.3)$$

where G is the gravitational constant, $\eta = \frac{GM}{Rc^2}$ the accretion efficiency and κ_0 is the Thompson opacity given by

$$\kappa_0 = \frac{8\pi}{3} \left(\frac{e^2}{m_e c^2} \right)^2 \frac{1}{m_u} \sum_i \frac{Z_i}{A_i} X_i \quad (3.4)$$

Here, ρ is the mass density, T is the temperature, m_e is the electron mass, m_u is the unit mass, e is the electron charge and c the speed of light. The quantities A_i , Z_i and X_i are the nucleon number, proton number and mass fraction respectively. Applying the conditions above, the initial X-ray burst model accretes solar composition with $0.05 M_{edd}$.

Furthermore, we define a fixed heating source Q_{heat} at the inner boundary which accounts for nuclear reactions, neutrino cooling and heat transport from the inner layers of the neutron star. This heating source enters our calculations as a boundary luminosity L_{crust} which is given by

$$L_{crust} = \frac{Q_{heat}}{m_u} \dot{M}_{acc} c^2, \quad (3.5)$$

where L_{crust} is the heat luminosity as seen from infinity, m_u is the atomic mass unit and \dot{M}_{acc} is the accretion rate. The heating source Q_{heat} is set in units of MeV per accreted nucleon. We use an adaptive grid with 129 grid zones and set outflow boundary conditions (see above). The pressure at the outermost zone is set to $5 \cdot 10^{18}$ erg/cm³, the surface temperature is calculated using the zero flux boundary conditions up to a pressure of 10^{17} erg/cm³ (see above).

To analyze the reaction flows during a explosive burning, we make use of two different networks: a 304 isotope network which is described in Fisker et al. (2006, 2008) and an extended 561 isotope network (Reichert 2013, private communication).

The progenitor file consists of a pure artificial Fe54 composition, see figure 3.1. While

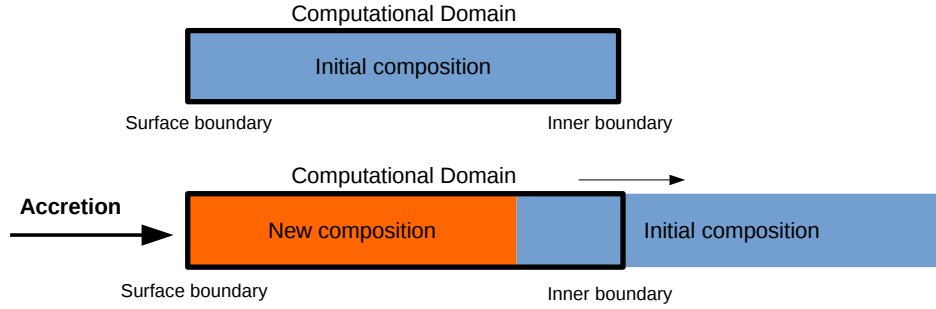


Fig. 3.1 The initial progenitor file consists of an artificial composition. By running the simulations, the initial composition is shifted out of our computational domain, replaced by previously accreted matter.

using the outflow boundary conditions, we run our X-ray burst simulations until the initial Fe54 composition is shifted out of our model at the inner boundary. This procedure makes sure that we have a X-ray model which is independent of initial conditions.

3.2 Nuclear network comparison

The aim of the current investigation is to verify the size of our nuclear network. The 304 isotope network has been tested and verified by Fisker in 2006 with the Jina REACLIB version 0. During our current simulations, we use the updated reaction rates REACLIB V2.0 submitted by Cyburt et al. in 2012 which might introduce some changes in the reaction flow during explosive burning. Hence, one could argue that the verification of Fisker is no more valid and the size of the nuclear network is no more appropriate.

In order to test the size of our nuclear network, we run two simulations with two different networks: a large 561 isotope network and a smaller 304 isotope network. You should note that a larger network will seriously slow down the simulations, thus it is advisable to reduce the number of isotopes as much as possible. Figure 3.2 shows a comparison between the two different networks. Using the smaller network, we neglect in our calculations especially isotopes with large proton and neutron numbers towards the valley of stability.

Since the choice of boundary conditions and parameters influences the reaction flow during a simulation, we adopt here two different tests. In a first step, we set a large

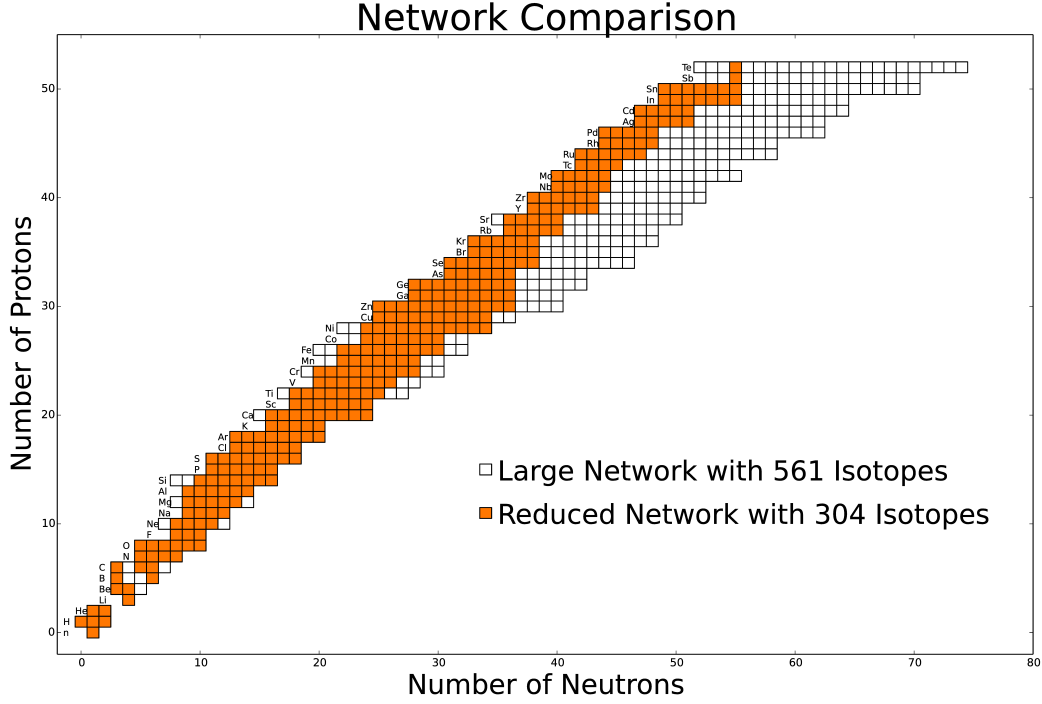


Fig. 3.2 A comparison between the full 561 isotope network and the reduced 304 isotope network.

accretion rate which results in a sequence of X-ray bursts with small recurrence time and rather small maximal burst luminosity. As a second test, we put the accretion rate to a lower value which provides us a solution with large recurrence time and high maximal burst luminosity.

3.2.1 Model with $0.1 \dot{M}_{\text{edd}}$

To start with, we take the initial model as described in 3.1 but change the accretion rate to $1.88 \cdot 10^{17}$ g/s which corresponds to $0.1 \dot{M}_{\text{edd}}$. At the inner boundary, we place a crustal heating source of $Q_{\text{heat}} = 0.5$ MeV per accreted nucleon which enters the calculations as a boundary luminosity. We run the simulations until all iron from the initial model has been advected out through the inner boundary of the model, see figure 3.1. Such a procedure ensures that the simulation of X-ray bursts is independent of the initial composition and conditions.

To get a first overview of the differences between the two different network models, we consider the recurrence time between the bursts. The time between two bursts depends sensitively on the conditions at the ignition point. The composition at the

Properties	304 isotopes	561 isotopes	Percent deviation
Recurrence time [h]	1.344	1.350	0.44%
Max luminosity [erg/s]	$4.940 \cdot 10^{37}$	$5.096 \cdot 10^{37}$	3.16%
Min luminosity [erg/s]	$4.450 \cdot 10^{35}$	$4.459 \cdot 10^{35}$	0.20%
Burst time [s]	123.191	124.141	0.77%
Mass fraction of C12 []	0.012	0.011	8.33%

Table 3.1 The properties of the explosive burning averaged over 50 X-ray bursts using a high accretion rate. The maximal luminosity is the burst peak luminosity and the percent deviation corresponds to the percentaged deviation from the value of the 304 isotope network.

layer where the ignition takes place consists of mainly hydrogen and helium mixed with some ashes from the previous X-ray burst. Further, the ashes of the explosive burning affect among others the heat transport, and thus the temperature at the ignition point. Hence, if the two networks would differ in the resulting ashes, one would expect a discrepancy in the recurrence time.

By the reason that each X-ray burst in our simulations is unique, it would make no sense to compare burst light curves of single bursts. In the following, we therefore investigate differences in averaged properties. We calculate the averaged values of the main features of X-ray burst explosion by taking a sequence of 50 bursts. Taking the average, we found a recurrence time of 1.344h using the 304 isotope network and 1.350h using the 561 isotope network. The difference in recurrence time between the two network models is of the order of 10s which is below one percent of the average recurrence time. Hence, we can conclude that given an accretion rate of $0.1 \dot{M}_{edd}$, we can safely use the network with the reduced number of isotopes without seriously influencing the recurrence time.

The peak luminosity can indicate how much hydrogen and helium is burned during the burst. Explosive burning stops either when the hydrogen is exhausted, matter is no more degenerate or when the rp-process reaches the end-point at ^{107}Te and ^{108}Te where the process is terminated by (γ, α) -photodisintegration (Schatz et al., 2013).

Comparing the maximal burst luminosities of our calculations with the two different reaction networks, we average over a sequence of 50 bursts and find a change in peak luminosity of the order of a few percent. Indeed, the peak luminosities of calculations with the 561 isotope network are slightly increased compared with the results of a 304 isotope network simulation. However, since the difference in peak luminosity is of the order of a few percent, one might not expect a significant change in the profile of the ashes or in the conditions at the ignition region. On the other side, the min-

imal luminosity between two bursts is a measurement of quiescence burning at the time of minimal burst luminosity. Both models agree well in minimal luminosity of $\sim 4 \cdot 10^{35} \text{erg/s}$, the difference is below one percent.

A further property of a Type I X-ray burst light curve is the burst time during which the luminosity is increased due to a burst. The burst time depends on the heat transport as well as on the reaction flow during explosive burning. The rise of luminosity is mainly linked to the reaction flow, while the decay depends mainly on the cooling properties. We found an average burst time of 123s for the 304 isotope network calculation and 124s for the 561 isotope network. The agreement is quite remarkable and shows that the reactions during the decay as well as cooling are not largely affected by the choice of network. You should note that the increased peak luminosity of the 561 isotope network requires a slightly longer decay time.

Finally, we compare the composition of the ashes at the inner boundary. At this

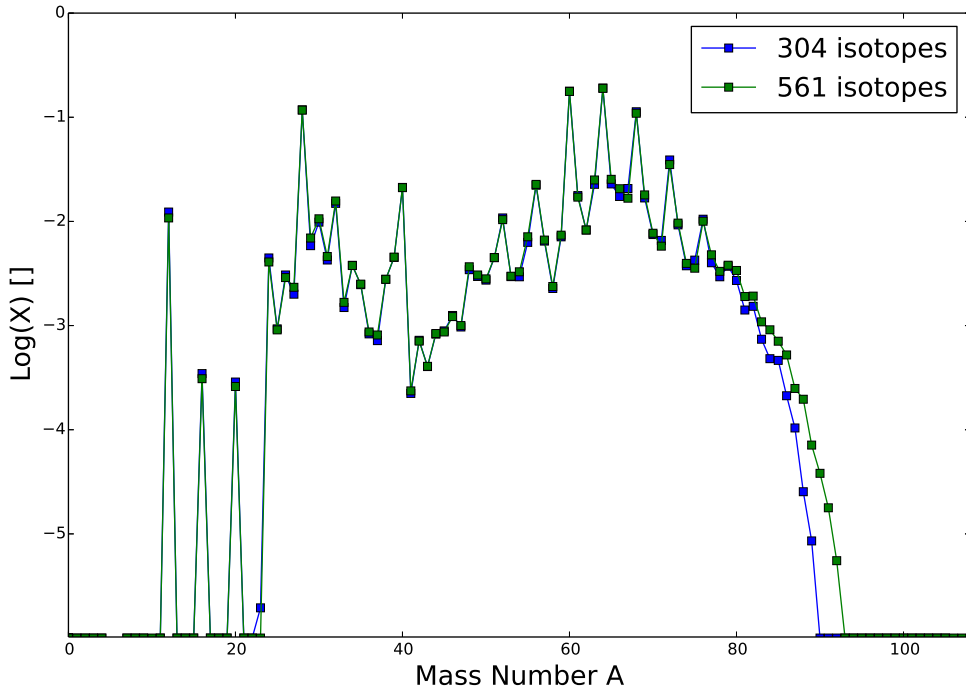
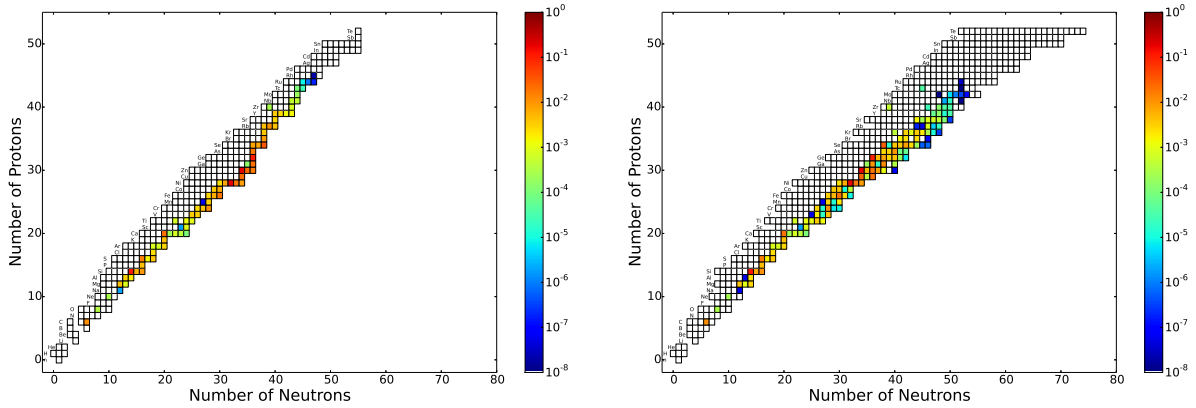


Fig. 3.3 A comparison of the mass fraction of the ashes at a density of $8 \cdot 10^6 \text{ g/cm}^3$ between the full 561 isotope network and the reduced 304 isotope network.

depth, the composition is generated by the simulation of several hundreds of X-ray bursts. Thus, the composition is a kind of averaged property and does not depend on the uniqueness of a single burst. In figure 3.3 we plotted the mass number A versus the

logarithm of the mass fraction X at a density of $8 \cdot 10^6 \text{ g/cm}^3$. With the 304 isotope network we obtain a slight shift to lower mass number isotopes which is consistent with the observation of a lower peak luminosity. Indeed, we found a mass fraction of ^{12}C of $1.23 \cdot 10^{-2}$ for the 304 isotope network calculation and $1.08 \cdot 10^{-2}$ for the 561 isotope network. On the other side, the ashes of the simulation with a large network proceed to heavier isotopes.

The nuclear chart of the mass fractions in figure 3.4a and 3.4b shows that the 561



(a) Mass fraction X of the composition of a simulation with an accretion rate of $0.1 \dot{M}_{\text{edd}}$. The composition is taken at a density of $8 \cdot 10^6 \text{ g/cm}^3$

(b) Mass fraction X of the composition of a simulation with an accretion rate of $0.1 \dot{M}_{\text{edd}}$. The composition is taken at a density of $8 \cdot 10^6 \text{ g/cm}^3$

isotope network shifts the ashes to the rather neutronrich side which is not included in the reduced network calculation. Indeed, heavy isotopes which are produced during the rp -process beta decay towards the valley of stability. Such reactions are not included in the reduced network. However, we found still a remarkable agreement in X-ray burst properties between the two network calculations.

3.2.2 Model with $0.025 \dot{M}_{\text{edd}}$

To judge whether the 304 isotope network is sufficient to describe the reaction flow during a type I X-ray burst, we do a second test with a low accretion rate model. Again, we take the setup from 3.1 and plug in a heating source of 0.5 MeV per accreted nucleon at the inner boundary. The accretion rate is set to $4.72 \cdot 10^{16} \text{ g/s}$ which corresponds to $0.025 \dot{M}_{\text{edd}}$. Applying a such low accretion rate reduces the heating at the inner boundary since the heating Q_{heat} which enters the calculation is depending on

Properties	304 isotopes	561 isotopes	Percent deviation
Recurrence time [h]	8.913	8.910	0.03%
Max luminosity [erg/s]	$1.114 \cdot 10^{38}$	$1.101 \cdot 10^{38}$	1.17%
Min luminosity [erg/s]	$8.376 \cdot 10^{34}$	$8.392 \cdot 10^{34}$	0.19%
Burst time [s]	69.163	69.007	0.23%
Mass fraction of C12 []	0.065	0.061	6.15%

Table 3.2 The properties of the explosive burning averaged over 50 X-ray bursts using an accretion rate of $0.025 \dot{M}_{\text{edd}}$. The maximal luminosity is the burst peak luminosity and the percent deviation corresponds to the percentaged deviation from the value of the 304 isotope network.

the amount of accreted nucleons. Due to this fact, the ignition of the explosive burning will take place at different conditions compared to the model with $0.1 \dot{M}_{\text{edd}}$. First of all, it takes a long time until sufficient fuel has been accreted to ignite a X-ray burst. We found an average burst recurrence time of 8.913h for the calculation with the 304 isotope network and 8.910h for the calculation with the full 561 isotope network. The difference in recurrence time between the two models is below one percent and thus, one can conclude that the reduced size of the network does not considerably change the average time between two bursts.

The maximal burst luminosities indicate where the reaction flow of the explosive *rp*-process is terminated. The bursts are very efficient at low accretion rate and the peak luminosities reach high values of the order of 10^{38} erg/s, see table 3.2. However, we found slightly higher peak luminosities for the model with the reduced network. The slight increase in peak luminosity results in a longer burst time for the 304 isotope calculation since cooling needs more time.

The minimal luminosity between two bursts does not depend on the choice of network. This means that at least at the time of minimal luminosity, no additional burning takes place in the model of the 561 isotope network. In figure 3.5 we plotted the mass fraction of the ashes for the two network calculations at a density of $8 \cdot 10^6$ g/cm³ in function of the mass number. At low accretion rate, we found good agreement of the ash composition in the range of lighter isotopes between the calculation with the full network and the reduced network. As in the case of high accretion rate, there is a slight shift to lower mass number for heavier isotopes using the 304 isotope network. Considering the ignition of a superburst at higher densities, it is important to investigate the amount of ¹²C in the ashes. We found that the reduced network calculation produces ashes with slightly more carbon than the full network calculation, see table

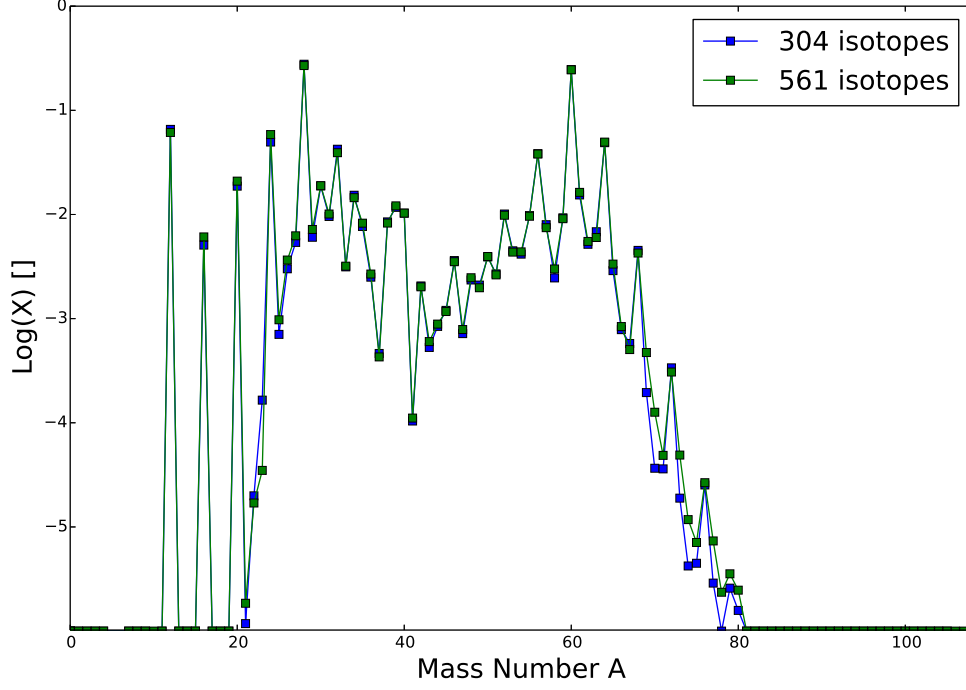
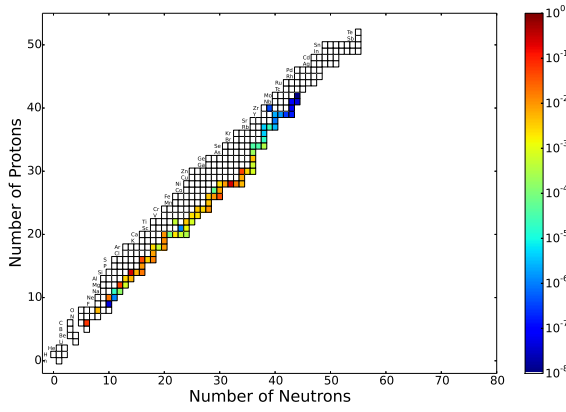
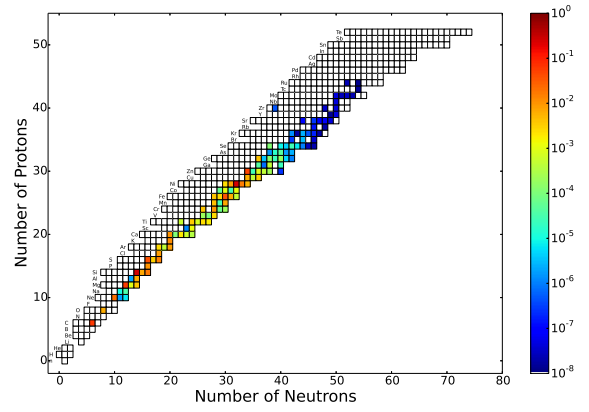


Fig. 3.5 A comparison of the mass fraction of the ashes at a density of $8 \cdot 10^6 \text{ g/cm}^3$ between the full 561 isotope network and the reduced 304 isotope network.



(a) Mass fraction X of the composition of a simulation with an accretion rate of $0.025 \dot{M}_{edd}$. The composition is taken at a density of $8 \cdot 10^6 \text{ g/cm}^3$



(b) Mass fraction X of the composition of a simulation with an accretion rate of $0.025 \dot{M}_{edd}$. The composition is taken at a density of $8 \cdot 10^6 \text{ g/cm}^3$

3.2. In addition, isotopes with large proton number proceed to the valley of stability by beta decay for simulations with the 561 isotope network. Such reactions are not included in the reduced network calculations and might introduce some problems.

In the following subsection, we will discuss in more details the advantages and disadvantages of using a reduced network.

3.2.3 Problems with Use of Reduced Network

In the previous subsections, we did two test simulations with a 304 isotope network and a 561 isotope network. At higher accretion rate, the accretion-dependent heating source at the inner boundary is dominant and hence, the quiescence *rp*-process plays an important role (see below). Quiescence burning before the explosive runaway weakens the burst. On the other side, with low accretion rate, the heating between two bursts is not strong enough and the explosive *rp*-process is very efficient.

For both test simulation, we found that the mass fraction of 12 in the ashes is smaller using a full nuclear network. The effect is more severe in the network test at larger accretion rate where we found an percent deviation of almost ten percent.

Further, heavier isotopes beta decay to more neutron-rich and stable isotopes which are not taken into account in the simulation of a reduced network. Such a shift in the composition towards the valley of stability might have an impact on the superburst ignition. However, recurrence time, peak luminosities and minimal luminosities of a sequence of X-ray bursts are not considerably affected by the choice of the two nuclear network sizes.

The ashes of X-ray bursts influence the heat conduction which might become important during the simulations of superburst. We therefore have to make sure that the opacity is not largely affected by the use of a reduced network. In figure 3.7 we plotted the opacities between two bursts for all our test simulations. The opacity is varying considerably by changing the accretion rate, but shows no large difference if we apply a smaller network. You should note that at lower column density, the opacity is strongly varying over time and hence, the opacities in figure 3.7 show some small differences at the surface for models with the same accretion rate. However, of main interest are the opacities in deeper layers between the X-ray burst and superburst ignition region. In terms of the opacities, we can safely apply the 304 isotope network without modifying considerably the heat transport.

The number of isotopes used in the network alters the simulation time of a given model. The larger the nuclear network, the more time is needed to compute a single X-ray

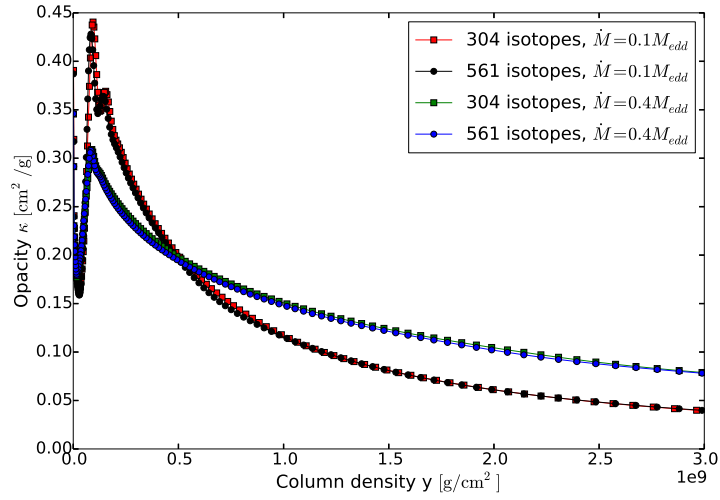


Fig. 3.7 The opacities between two bursts in function of the column density. The squares correspond to the 304 isotope network simulations, whereas the circles indicate the solutions obtained with the 561 isotope network.

burst. A simulation of a self-consistent ignition of a superburst requires thousands of X-ray burst. As a consequence, one should try to reduce the size of the network as much as possible. In our following calculations, we will compute solution with the 304 isotope network, but keeping in mind the problems due to the choice of the reduced network.

Chapter 4

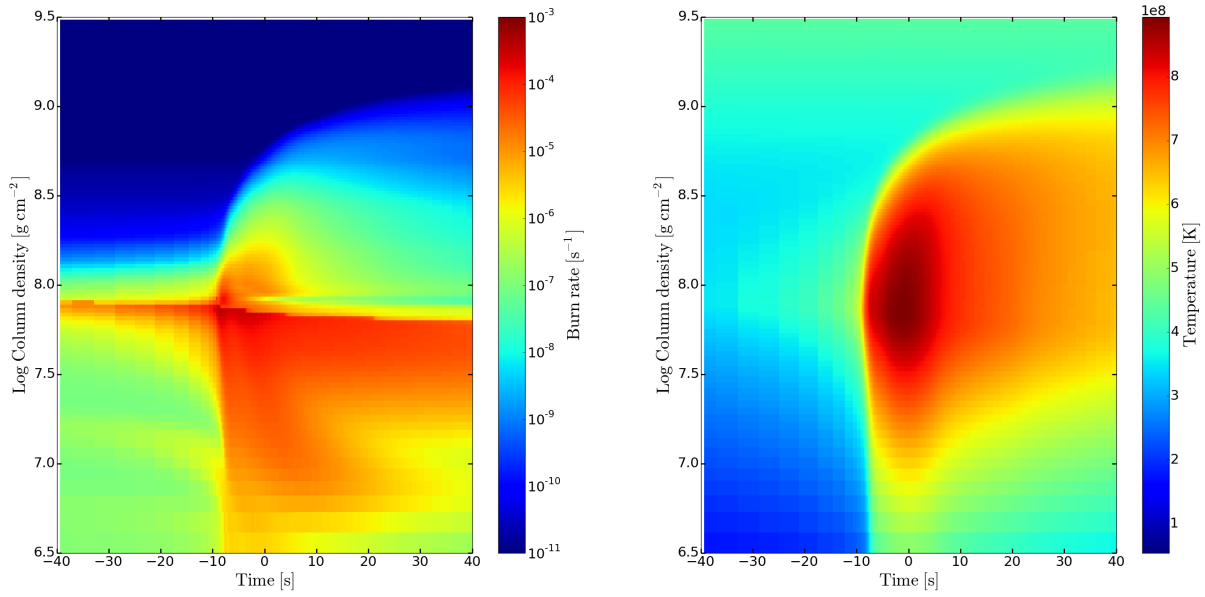
Simulations of X-ray bursts

In general, during a X-ray burst, accreted hydrogen and helium is converted to heavier elements. In this section, we focus on the reaction flow during a single X-ray burst simulation. Understanding the reactions during the accretion of solar abundances will help us to understand how to influence the composition of the ashes. Applying the initial conditions described in 3.1 together with a heating source of $Q_{heat} = 0.5$ MeV/nuc, we find X-ray bursts with a recurrence time of 3.28 h and a burst peak luminosity of $6 \cdot 10^{37}$ erg/s. A typical burst is taking place during a time range of 120 seconds and the quiescence minimal luminosity is of the order of 10^{35} erg/s.

The ignition region is found to be at a density of $3 \cdot 10^5$ g/cm³ and a temperature of $3 \cdot 10^8$ K. The composition in the ignition zone consists of freshly accreted matter mixed with ashes from the previous bursts.

The Kippenhahn diagram 4.1 shows an overview of the temperature and burn rate evolution during a X-ray burst. The time axis is chosen such that the peak burst luminosity coincidence with $t = 0$ s. As different regions in our model burn differently due to different compositions, densities and temperatures while interacting with neighboring regions, one must consider all the burning layers to understand the X-ray burst. Indeed, the burn rate in Figure 4.1a demonstrates that the burning of matter is taking place over a wide range in the outer layer of a neutron star and is proceeding even before the ignition of a X-ray burst.

Based on this fact, we analyze the nuclear reactions in three different regions: the surface layer, the ignition point and the region of the ashes.

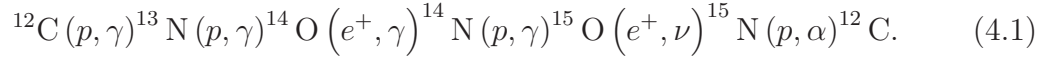


(a) Contour plot of the burn rate in function of the column density and time. (b) Contour plot of the temperature in function of the column density and time.

Fig. 4.1 Kippenhahn diagram of the burn rate and temperature. The time axis is chosen such that the peak burst luminosity is found at $t = 0$ s. The burn rate is described in units of s⁻¹, the temperature in units of K.

4.1 Surface Layer

At the surface, accreted matter is continuously piled on top. The accreted matter is thought to consist mainly of hydrogen and helium. As the temperature and density is increasing, hydrogen starts to burn via the pp -channel and CNO-cycle. At a given depth in the accreted fuel layer, the temperature is high enough such that the CNO-cycle starts to dominate. At even higher temperature, the proton capture on ^{13}N becomes faster than the β^+ -decay and therefore, burning is proceeded via the hot CNO-cycle which can be described by



During our simulations, we accrete matter with solar composition which enters the model through the outermost zone. Such a composition is not in equilibrium in the outermost zone and will immediately start with proton capture on ^{12}C , ^{13}N and ^{14}N . At the same time, the $^{15}\text{N}(p, \alpha)^{12}\text{C}$ reaction of the hot CNO-cycle is releasing ^4He which results in an increase of the abundance of ^4He . The accreted amount of carbon and nitrogen is exhausted quickly while enhancing the fraction of ^{14}O and ^{15}O . Due to the fact that the reaction timescales are limited by the β^+ -decays instead of proton capture, the accreted composition is entering a beta-limited CNO cycle. The helium is transformed to ^{12}C via the strongly temperature-sensitive triple-alpha process which is described by



The energy generation from the triple-alpha reaction heats the matter in the surrounding and is responsible for triggering the break-out reactions of the hot CNO cycle. Hence, it is crucial during our simulations to use the correct reaction rates for the triple-alpha reaction. We use the reaction rates from Fynbo et al. (2005) which have been experimentally determined.

The ^{12}C which is produced due to the triple-alpha process acts as a seed for the hot CNO cycle. On the other side, the (p, α) process in the hot CNO cycle feeds the triple-alpha process.

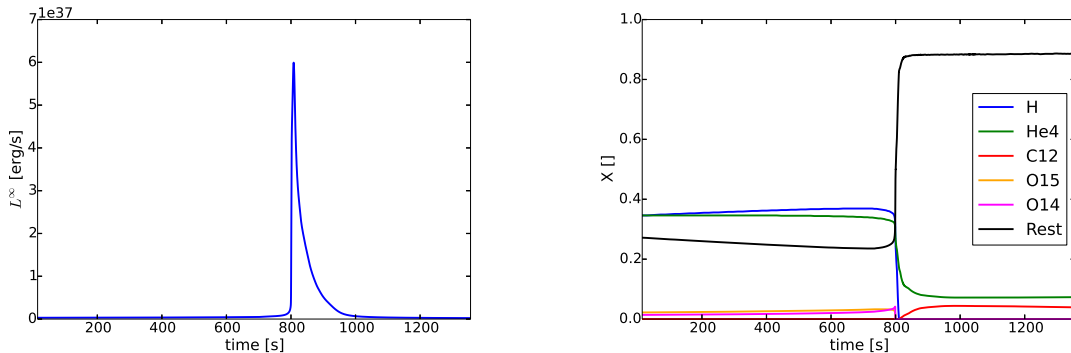
Up to a density of approximately $2 \cdot 10^5 \text{ g cm}^{-3}$, the hydrogen fraction is exhausting at the same rate as the helium fraction increases and can therefore be explained by the beta-limited network. Below this layer, the fraction of hydrogen is decreasing at

a much faster rate than the fraction of helium which indicates that proton capture on others isotopes becomes competitive with the hot CNO-cycle.

Close to the ignition region, the $^{15}\text{O}(\alpha, \gamma)$ reaction is in competition with the β^+ -decay. This early breakout of the hot CNO cycle provides a composition of heavier isotopes and thus consumes the fraction of hydrogen. The quiescence rp -process proceeds up to the double magic ^{40}Ca and hence consumes a large amount of hydrogen prior to the explosive burning. Due to the missing fraction of hydrogen and the composition of better bound nuclei at the ignition zone, the proceeding X-ray burst is weakened. Indeed, the amount of fuel at the ignition plays a crucial in the energetic of a X-ray burst.

In the following section, we will have a closer look at the nuclear reaction at the ignition depth.

4.2 Ignition zone



(a) The time evolution of the X-ray burst luminosity as seen from infinity.

(b) Mass fraction X of the composition in the ignition zone in function of the time.

Fig. 4.2 The change of the composition at the ignition zone during a single X-ray burst.

During explosive burning in the ignition zone, mostly hydrogen and helium are burned via the rp -process (Wallace and Woosley, 1981), resulting in a composition of heavier isotopes. In Figure 4.2b we plotted the time evolution of the composition in the ignition zone. The time scale has been synchronized to match with the time evolution of the red-shifted surface luminosity in figure 4.2a.

Above the ignition layer, the hot CNO cycle transforms hydrogen into helium as described in 4.1. Because the triple-alpha process is running faster with increasing temperature and density, the amount of ^{14}O ($T_{1/2} = 76.4$ s) is growing. On the other

side, the hot CNO cycle produces ${}^4\text{He}$ until the runaway through the triple-alpha occurs.

Shortly before the explosive runaway, as the temperature is increasing above $\sim 10^8$ K ${}^{15}\text{N}$, ${}^{18}\text{O}$, ${}^{18}\text{F}$, ${}^{19}\text{F}$ and ${}^{23}\text{Na}$ start capturing a proton. Furthermore, proton capture takes also place on ${}^{34}\text{S}$ and $N - Z = -1$ isotopes between neon and silicon. Such (p, α) -reactions are responsible for small temperature fluctuations in the ignition layer (Fisker et al., 2008), but are not able to trigger the runaway.

At the ignition zone, the temperature is high enough to enable a reaction flow

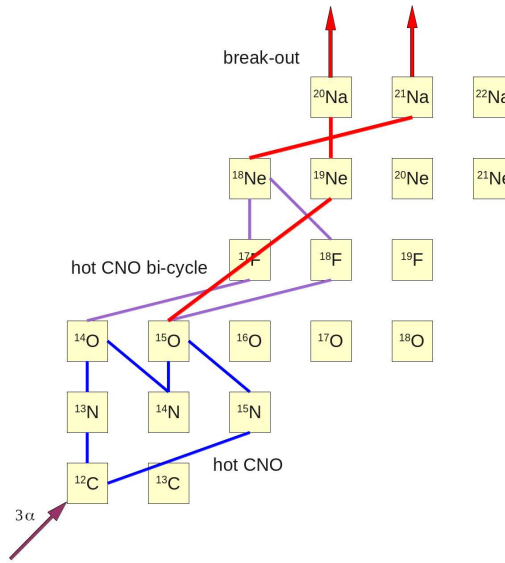


Fig. 4.3 A schematic view of the reaction in the ignition zone.

via the the hot CNO bi-cycle (see Figure 4.3). The bi-cycle further speeds up the conversion of hydrogen to helium and hence influences the composition in the ignition zone. Meanwhile due to the heat generation from the triple-alpha reaction, the ignition layer is heated and at some point, the following condition is fulfilled:

$$\frac{d\epsilon_{nuc}}{dT} > \frac{d\epsilon_{cool}}{dT}, \quad (4.3)$$

where ϵ_{nuc} is the nuclear energy generation rate and ϵ_{cool} is the cooling rate. If the condition is fulfilled at degenerate conditions, the X-ray burst is ignited. A runaway is therefore triggered if the reactions in the matter become thermally sensitive by the triple-alpha reaction or by the rp -process (Schatz et al., 1998; Van Wormer et al., 1994; Wallace and Woosley, 1981).

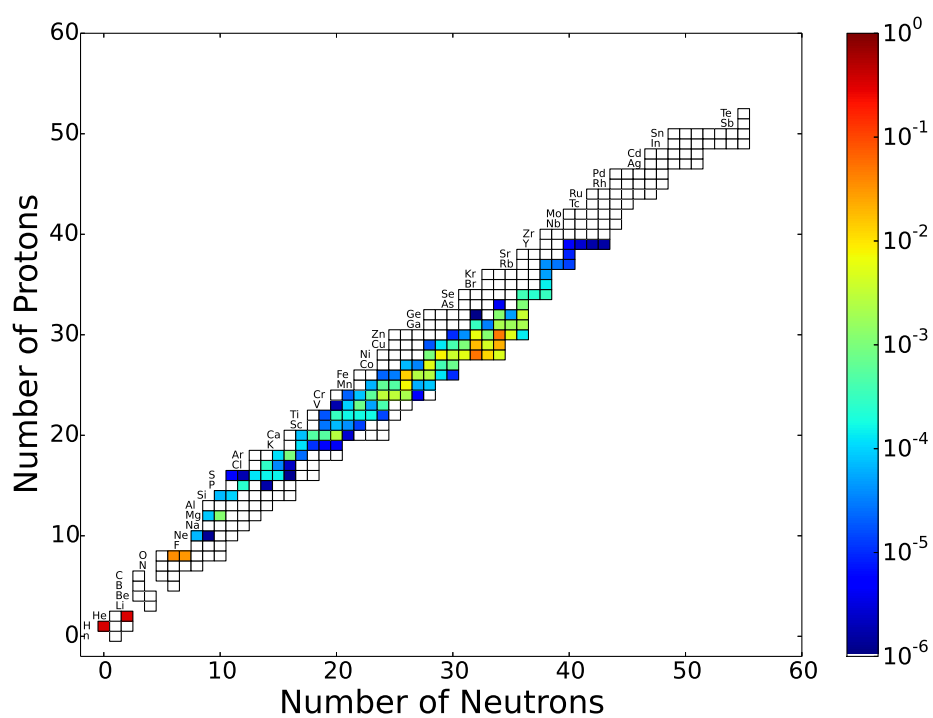


Fig. 4.4 The massfraction of the composition at the ignition zone just before the explosive runaway takes place.

The nuclear chart in Figure 4.4 describes the composition of the matter in the ignition zone just before the explosive runaway takes place. At this stage, we find a mass fraction of hydrogen equals 0.432 whereas the mass fraction of helium is 0.331. In the ignition region, the accreted fuel is mixed with the ashes from the previous burst consisting mainly of ^{56}Ni or ^{60}Zn . You should also note that the abundance of ^{14}O and ^{15}O is increased due to the cycling reactions described above. Further, the quiescence rp -process has already influenced the composition up to ^{40}Ca .

A breakout of the hot CNO bi-cycle is caused via $^{15}\text{O}(\alpha, \gamma)^{19}\text{Ne}$ at a temperature around $\gtrsim 3 \cdot 10^8 \text{ K}$. At even higher temperature, what means at $T \gtrsim 6 \cdot 10^8 \text{ K}$, the breakout flow is also proceeding via $^{18}\text{Ne}(\alpha, \gamma)^{21}\text{Na}$. Such a breakout leads to the rp -process which consists of a consecutive series of proton capture reactions and β^+ decay, resulting in heavier elements. During the rp -process, the proton capture is always in competition with (α, p) reactions: Proton capture consumes the hydrogen in the fuel, whereas (α, p) reactions depletes the helium.

The endpoint of the rp -process is determined by five possible scenarios:

Cycling reaction flows: A (p, α) reaction may lead to a termination circle. If no circle develops, the rp -process might continue up to the SnSbTe-circle which finally terminates the process (Schatz et al., 2001).

Coulomb barrier: The Coulomb barrier for α particles increases rapidly towards heavier nuclei and hinders the rp -process to operate.

Gas of electron stops being degenerate: The nuclear reactions release energy which heats up the gas. At some point, the electron gas is no more degenerate and expands, slowing down the nuclear reactions.

Running out of fuel: The rp -process is terminated as soon as seed nuclei such as the hydrogen or helium are exhausted in the ignition region.

Very fast cooling: If cooling happens too fast, the temperature is not sufficiently high for the (α, p) reaction to occur and hence, the rp -process is terminated.

Waiting points due to slow β^+ decay have a large influence on the reaction flow during an outburst. Due to the slow reactions, the abundances of such waiting points accumulate which makes an even identification easier.

Using our model, we found that none of the accreted hydrogen survives in the ignition zone, whereas a mass fraction of helium of 0.067 remains. The composition in the ignition zone at the peak luminosity is shown in figure 4.5. At a temperature of $9 \cdot 10^8 \text{ K}$,

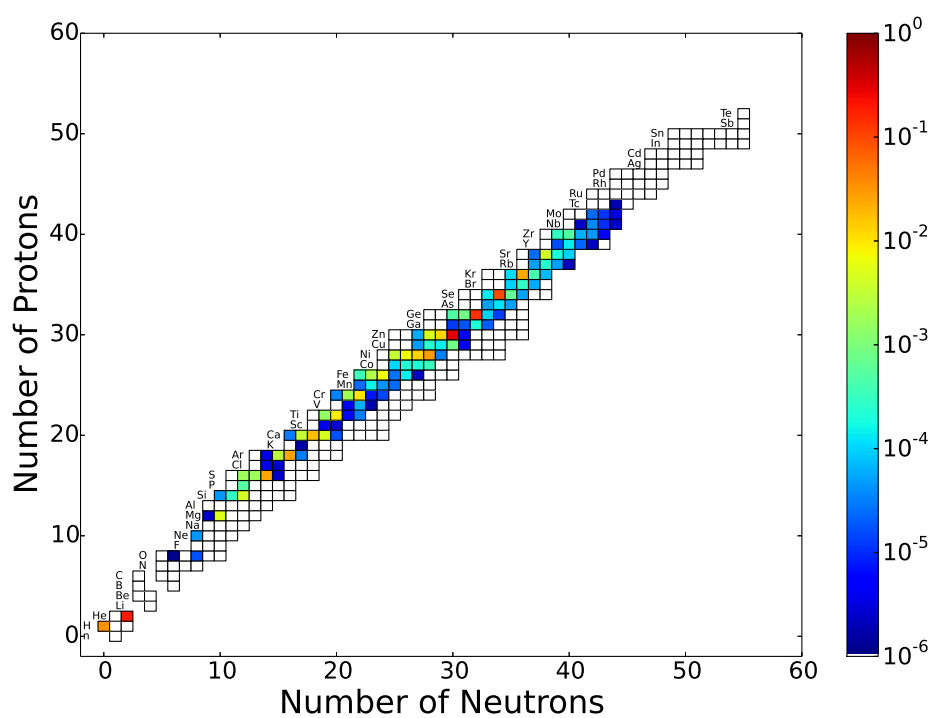


Fig. 4.5 The composition at the ignition zone at peak luminosity. The abundances are shifted to the less neutron rich range.

the composition is shifted towards the proton drip line since the weak interaction is slower than the strong interaction and electromagnetic force. The reaction flow of the rp -process proceeded mainly up to ^{87}Tc . At the peak luminosity, we still find both hydrogen and helium in the ignition zone which indicated that the rp -process might still proceed as there is still some fuel left. However, at the peak luminosity, we find a temperature of $9 \cdot 10^8$ K and a density of $3 \cdot 10^5$ g/cm³ at the ignition zone which indicates that matter is no more behaving as a degenerate gas and hence, the reaction flow is slowing down.

The most abundant isotopes apart from the seed nuclei are ^{60}Zn , ^{64}Ge and ^{68}Se which are waiting point nuclei due to slow β^+ decay.

At high temperatures during the bursts, the matter is no more degenerate and

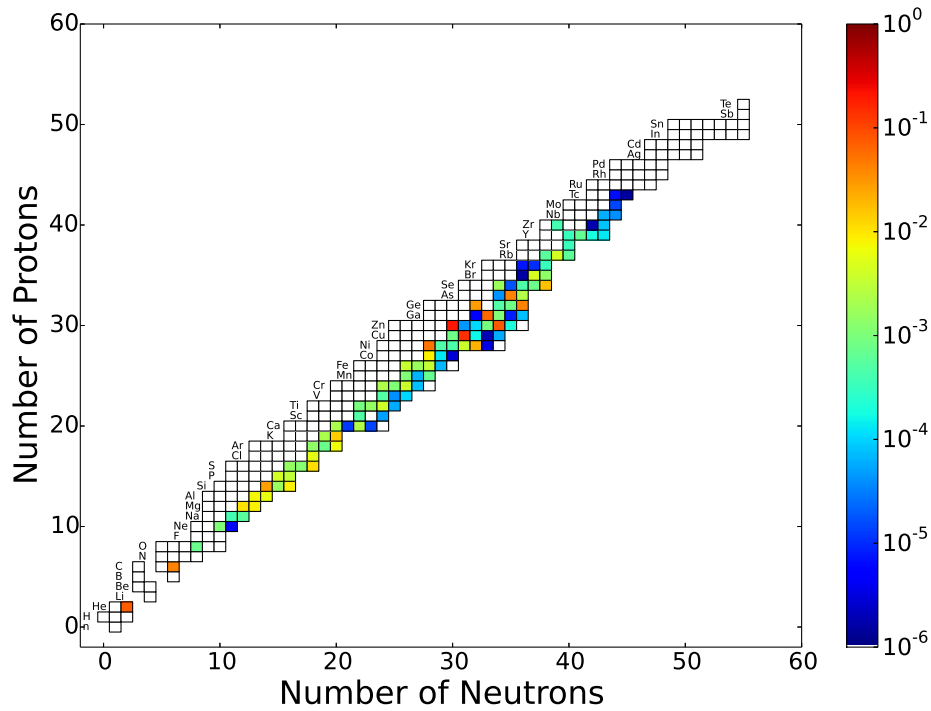


Fig. 4.6 The composition at the ignition zone after the explosive runaway.

expands which terminates the rp -process. The leftover of hydrogen is consumed by proton capture reactions and the composition starts to cool. In figure 4.6, we plotted a chart of the composition at the ignition depth at a temperature of $2.9 \cdot 10^8$ K after the outburst. The previous outburst has burned all the hydrogen in the accreted fuel layer, but left a helium mass fraction of 0.08. As the temperature slowly decreases, the

isotopes do beta decay to a more stable configuration. Due to the reduced network, isotopes with large proton number can not beta decay to the valley of stability, see chapter ?? . Indeed, a full network calculation would allow isotopes with large proton number to do β^+ -decay towards the valley of stability. Such reactions not only lead to the emission of neutrinos but contribute also to the burst decay phase. We note here that previous studies in Chapter 3 showed that the impact of additional beta decays of nuclei seemed to be negligible.

4.3 Ashes

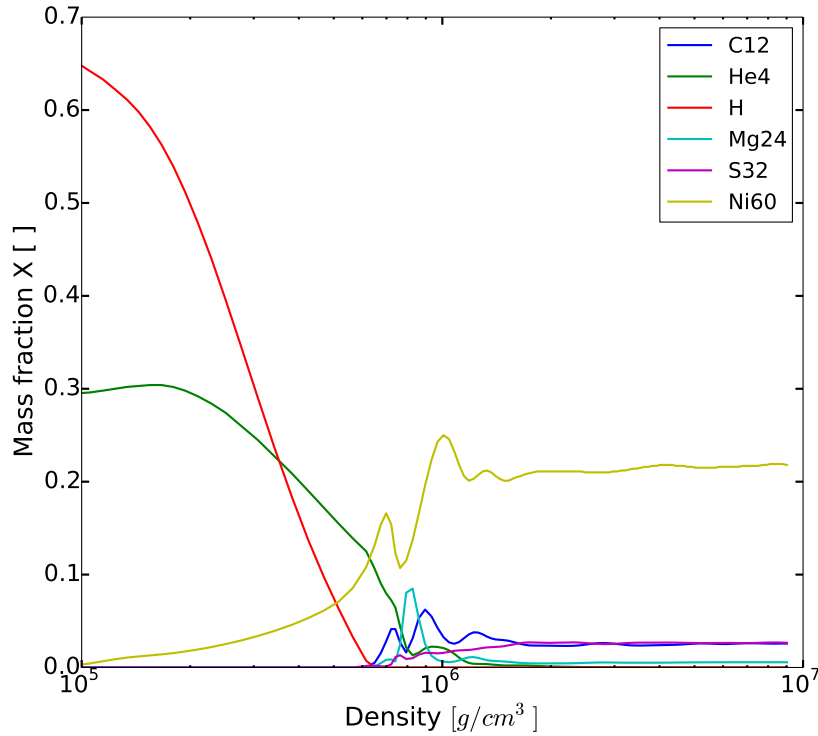


Fig. 4.7 The composition between two bursts in function of the density.

After the explosive rp -process is terminated, the composition starts to stabilize. While cooling, the reaction flows are reducing until burning is frozen because of the decrease in temperature. In fact, nuclear burning is ceased at the inner boundary of our model, see figure 4.7. To ignite self-consistently a superburst at higher densities, one needs a sufficient high mass fraction of carbon in the ashes. The abundance of

carbon in the ashes is created after all hydrogen in the the accreted ignition layer has been consumed. This means, carbon is produced just after the termination of the explosive *rp*-process. Any leftover of hydrogen would simply destroy the ^{12}C in the layer of ashes since carbon would quickly do proton capture. The key essence to create enough carbon is therefore the mass fraction of helium that is able to survive the burning during a X-ray burst. Stable burning of helium would then finally lead to the desired large amount of carbon in the ashes at superburst ignition depth. However, at high temperature ($> 5 \cdot 10^8$ K) carbon fusion occurs, producing magnesium while destroying carbon (figure 4.7). Further, if the temperature is high enough carbon is consumed by alpha capture reactions. As a conclusion, one needs not only enough helium which burns stably to carbon but also a steep temperature gradient which ensures a survival of carbon right after the burst. In general, at a given luminosity, a large temperature gradient is achieved by a large opacity which depends on the composition, temperature and density.

4.4 Opacity

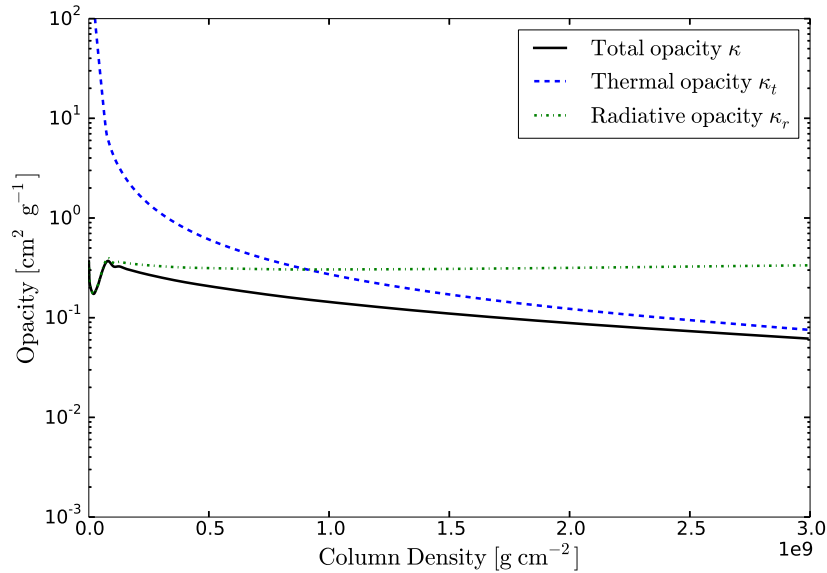


Fig. 4.8 The evolution of the opacities in function of the column density. The green point-dashed line corresponds to the radiative opacity, the blue dashed line is the thermal opacity and the black line corresponds to the total opacity given as the harmonic sum of thermal and radiative opacity. The profile is calculated between two bursts at minimal burst luminosity.

The opacity in simulations of X-ray bursts and superbursts plays a crucial role since it determines the heat transport. In order to study the importance of the heat flux in the outer layers of a neutron star, we need to analyze the contributions to the opacity at different depths. Figure 4.8 shows the total opacity, the thermal and radiative opacity. The opacities are linked in the following manner:

$$\frac{1}{\kappa} = \frac{1}{\kappa_r} + \frac{1}{\kappa_t}, \quad (4.4)$$

where κ is the total opacity, κ_r the radiative opacity and κ_t the thermal opacity

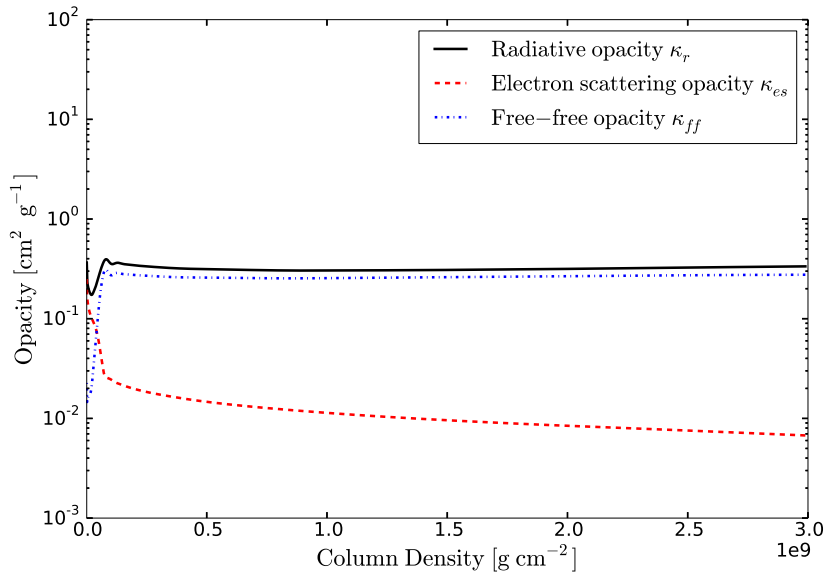


Fig. 4.9 The evolution of the opacities in function of the column density. The blue point-dashed line corresponds to the free-free opacity, the red dashed line is the electron scattering opacity and the black line corresponds to the radiative opacity. The profile is calculated between two bursts at minimal burst luminosity.

(see Chapter 2). At the outer layers of the neutron stars, what means at low column density, the radiative opacity is dominating. Below the ignition depth of X-ray bursts, the total opacity is mainly depending on the thermal opacity. In the ignition zone of X-ray bursts, the heat transport is strongly linked to the radiative opacity.

The radiative opacity is depending on the electron scattering opacity and the free-free opacity (see Chapter 2). Figure 4.9 shows the opacities in function of the column density. We found that at high column density, the radiative opacity is mainly depending on the contribution from the free-free opacity. Whereas at lower depths in the region of the X-ray burst ignition point, the electron scattering opacity is dominating.

As a consequence, in order to understand the steepness of the X-ray burst decay light curve, one would need to study the radiative opacity and thus the contribution due to electron scattering. The heat transport in the region below the X-ray burst ignition down to superburst ignition is linked to the thermal opacity.

In general, the heat transport down to densities of superburst ignition is not yet fully understood. The detailed descriptions of the opacities at conditions of high densities and sophisticated compositions of matter are far from being complete.

Chapter 5

Crustal Heating

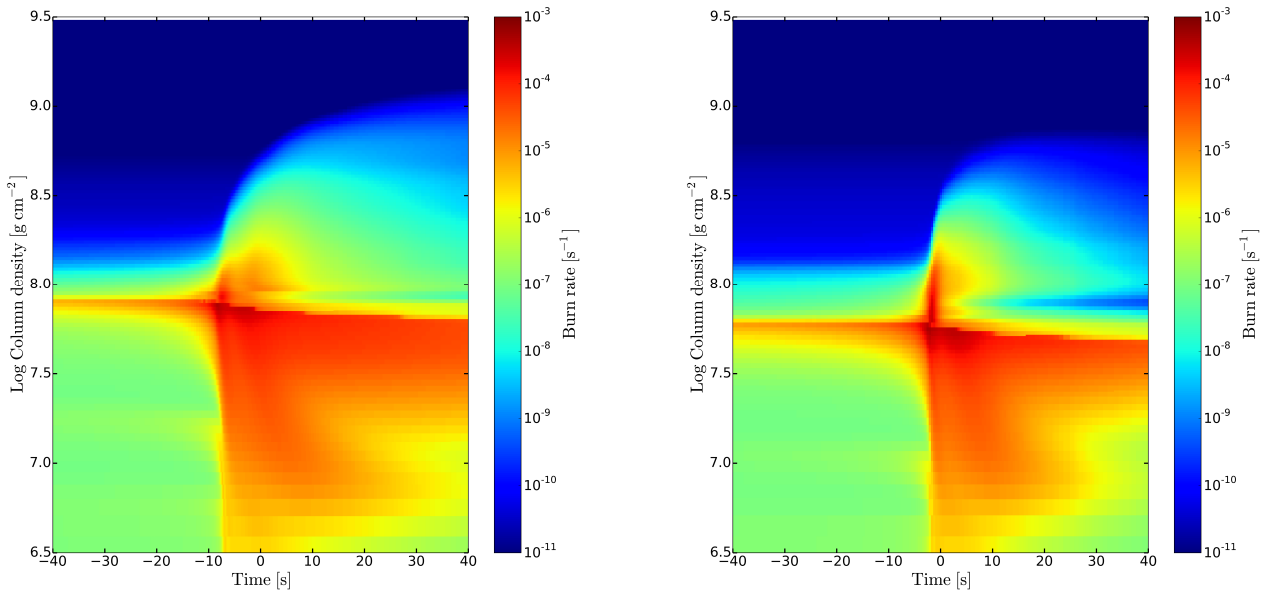
Even though simulations of Keek et al. (2012) have demonstrated that a superburst takes place due to unstable burning of ^{12}C , a self-consistent ignition of a superburst within the observed recurrence time range still remains a puzzle. Currently, simulations of type I X-ray bursts do not reproduce enough ^{12}C in the ashes. According to Cumming et al. (2006), one needs at least a mass fraction of $X_{12\text{C}} \gtrsim 0.1$ to find a superburst recurrence of the orders of a few years. Indeed, simplified simulations of a possible superburst in Hashimoto et al. (2014) confirm that $X_{12\text{C}} \gtrsim 0.1$ is required to ignite self-consistently a superburst.

A method to produce a large mass fraction of ^{12}C in the ashes is to add a heating source in the crust of the neutron star. Calculations of Schatz et al. (2013) indicate that the heating source is independent of the URCA process in the crust and hence, must be located in the ignition region of superbursts.

Also, observations of thermal relaxations of neutron stars suggest that an extra heating source is needed to reproduce the cooling correctly (Shternin et al., 2011). Furthermore, a very recent calculation of the crust of the neutron star in EXO 0748-676 from Turlione et al. (2013) has shown that an extra heat source of approximately 1.8 MeV per accreted nucleon should be placed at a density of the order of 10^9 g/cm^3 . Observations of MAXI J0556-332 support also the theory of a shallow heat source (?). However, the neutron star in EXO 0748-676 exhibits a small recurrence time of X-ray burst, but has never triggered a superburst. Also, transient MAXI J0556-332 did provide the ignition of a superburst. Up to now, the process which generate the extra heat in the crust of neutron stars is still unknown.

In the following sections, we aim to study the impact of crustal heating on the ignition of X-ray bursts and superburst. By the reason that an additional heating in

deeper layers of a neutron star influences observable properties, we will discuss in detail how one can apply different values of crustal heating while still maintaining the basic observable features of X-ray bursts.



(a) Contour plot of the burn rate as a function of the column density and time. The heating at the inner boundary is set to 0.5 MeV/nuc.

(b) Contour plot of the burn rate as a function of the column density and time. The heating at the inner boundary is set to 1.5 MeV/nuc.

Fig. 5.1 Kippenhahn diagram of the burn rate for different crustal heating at the inner boundary. The time axis is chosen such that the peak burst luminosity is found at $t = 0$ s. The burn rate is described in units of s^{-1} and the column density in units of g cm^{-2} .

5.1 Simulations with variations of crustal heating

To study the influence of a heating source on X-ray bursts, we take the initial model as described in 3.1. At the inner boundary of our model, we place an accretion dependent heating source Q_{heat} and apply the outflow boundary conditions. Such a heating at the boundary accounts for known or unknown heating sources at layers below the range of our model and enters the calculations as a crustal luminosity in the innermost zone. The heating Q_{heat} is given in units of MeV per accreted nucleon and is therefore directly linked to the accretion rate. In this section, the accretion rate is set to 10^{17}g/s

and the reaction network used in the calculations consists of 304 isotopes, see Chapter 3.

In order to analyze the variations in X-ray burst evolution due to the additional heating, we start with zero additional heating and increase Q_{heat} in steps of 0.1 MeV/nuc until, at a heating of 1.7 MeV/nuc, the temperature is too high and burning will occur in a stable manner instead of explosive burning. To find initial conditions independent results, we run the simulations till some kind of equilibrium cycle is reached.

To illustrate how heating affects the outer layers of a neutron star and therefore the ignition of an X-ray burst, we made a Kippenhahn diagram of the burn rate for a model with 0.5 MeV/nuc (Figure 5.1a) and for a model with 1.5 MeV/nuc (Figure 5.1b). The burn rate is an useful indicator to define the ignition depth of an X-ray burst, since the burn rate should be maximal at ignition conditions. The burn rate is given as

$$r_{burn} = \frac{E_{nuc}}{\Delta m c^2 \Delta t}, \quad (5.1)$$

where E_{nuc} is the energy release in units of MeV in a given zone due to nuclear burning, Δm is the mass in a zone in grams and Δt is the time step in units of seconds. The burn rate r_{burn} is therefore describing the burning in a zone in units of s^{-1} .

Models with different heating at the inner boundary already show large discrepancies just before the ignition of an X-ray burst takes place. Indeed, at a heating of 1.5 MeV/nuc (Figure 5.1b), we found the appearance of burning in a layer above the ignition depth as well as in the layer of ashes. Reducing the heating at the inner boundary is affecting the width of such a burning layer. The burning rate depends strongly on the composition and the temperature at a given depth and might therefore indicate that the temperature is increased in the layers of a model with increased crustal luminosity at the inner boundary. These conditions are not only found because of the additional heating, but also due to the heating of the previous X-ray burst. A shortening in recurrence time between two bursts does have a large impact on the temperature in our simulation domain. Indeed, as seen in Figure 5.2, the additional heating causes a reduction in recurrence time. However, at $Q_{heat} > 1.0$ MeV/nuc the X-ray burst recurrence time showed large alterations. At those conditions, we found a tendency to an increment of recurrence time with increasing heating at the innermost zone. Such a behavior is in agreement with results found in (Zamfir et al., 2014). A change in recurrence time is an indication that the ignition point of an X-ray burst is shifted to other conditions.

At a crustal heating of 1.5 MeV/nuc, the ignition point, that is the zone in which the

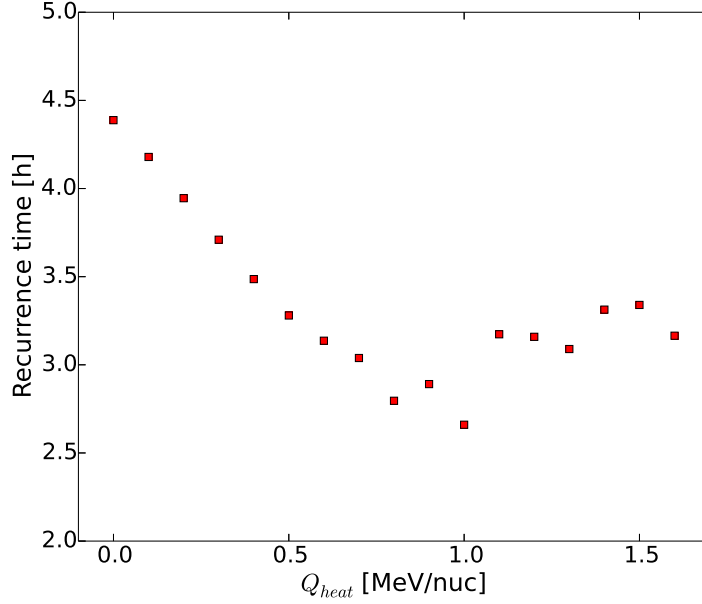
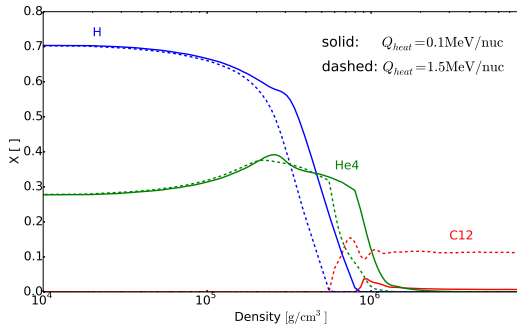
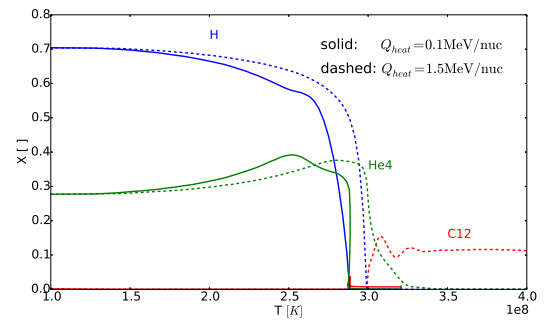


Fig. 5.2 The heating in units of MeV per accreted nucleon at the inner boundary versus the recurrence of X-ray bursts in hours. The recurrence time has been averaged over a sequence of a few hundreds of X-ray bursts.



(a) The mass fraction of carbon, helium and hydrogen versus the density just before ignition takes place.



(b) The mass fraction of carbon, helium and hydrogen versus the temperature just before ignition takes place.

Fig. 5.3 Hydrogen, helium and hydrogen as a function function of density and temperature. The dashed profile corresponds to a crust heating of 1.5 MeV/nuc and the solid profile indicates the solution with a crust heating of 0.5 MeV/nuc.

maximal burn rate appears, is shifted towards a lower column density in comparison with the ignition point at $Q_{heat} = 0.1$ MeV/nuc. This means that the addition of a heating source shifts the ignition point to lower densities but higher temperatures. To manifest this statement, we show the mass fraction of hydrogen, helium and carbon close before ignition as a function of the density and temperature, see Figure 5.3. Since an X-ray burst burns basically hydrogen and helium to heavier ashes, one can approximately define the ignition zone at the drop of the abundances of hydrogen and helium. The heating at the inner boundary pushes the ignition zone to lower densities and higher temperatures. Hence, we can not apply arbitrarily high values of crust heating since at some point, the ignition point is moved to conditions where matter is no more behaving like a degenerate gas.

A change in the ignition depth sensitively determines how efficiently an X-ray burst

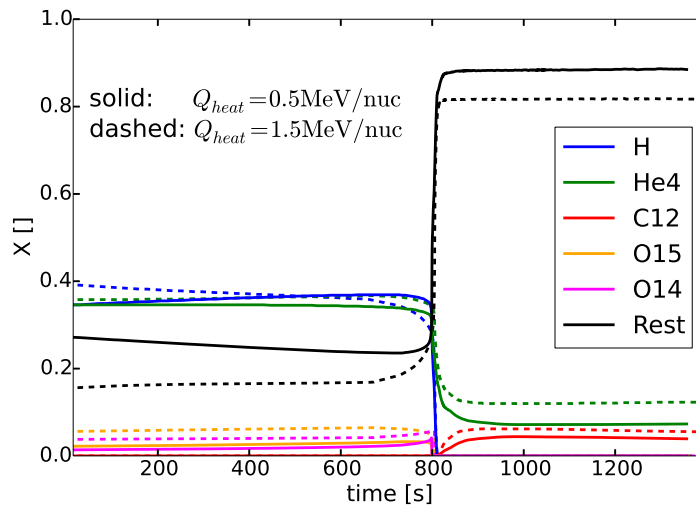


Fig. 5.4 The time evolution of the composition at the ignition point for two different heating sources. The dashed profile corresponds to high heating, whereas the solid profile corresponds to lower heating. The time axis has been chosen such that the peak luminosities of the two model coincident.

generates heavier isotopes. The degeneracy of the electron is weaker at higher temperature and lower densities, thus, models with a strong heating source at the inner boundary exhibit weaker bursts. Figure 5.4 shows the time evolution of isotopes which play a major role during X-ray bursts. The dashed line in Figure 5.4 corresponds to the time development of fuel and ashes with a rather high boundary heating of 1.5 MeV/nuc while the solid line shows the development with a rather moderate heating of 0.5 MeV/nuc. For both models, the composition is taken at the ignition zone

and evolves over one single burst.

In the case of a crust heating of 1.5 MeV/nuc we found an early decreasing of the mass fraction of hydrogen and helium just before the explosive runaway. At the same time, the amount of heavier isotopes starts to increase. We account this effect to the quiescence *rp*-process which destroys the hydrogen and shifts the composition of fuel towards better bound nuclei just before a breakout of the CNO bi-cycle leads to a reaction flow along the *rp*-isotope path. On the other side, at rather moderate heating, hydrogen and helium are accumulated in the ignition zone, producing plenty of fuel which is burned in a very efficient X-ray burst. At low heating, the matter at the ignition zone is more strongly degenerate and therefore, together with the fact that the required fuel is not burned in the quiescence *rp*-process, the explosive *rp*-process is able to proceed up to much heavier isotopes. As a comparison, since at strong heating ignition is shifted to higher temperature and lower densities, the X-ray burst is weakened due to less degenerate conditions and some fraction of the fuel remains.

Since ignition of X-ray burst are proceeding under alternate conditions with varia-

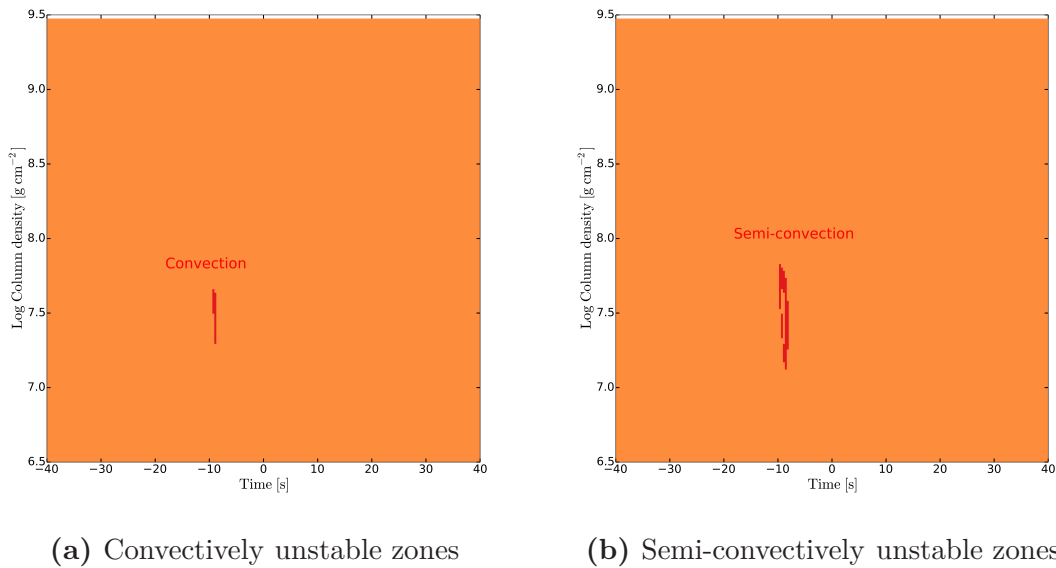


Fig. 5.5 The convection and semi-convection in function of column density and time. The time-axis coincides with the peak burst luminosity. The heating at the inner boundary is set to 0.5 MeV/nuc and the accretion rate is $\dot{M}_{acc} = 10^{17}$ g/s

tions in crustal heating, one should also expect a shift in the convective zone. As seen in Figure 5.5 and Figure 5.6, the convective and semi-convective zone covers a range of a few seconds close to the ignition depth of a X-ray burst. Further, true convection

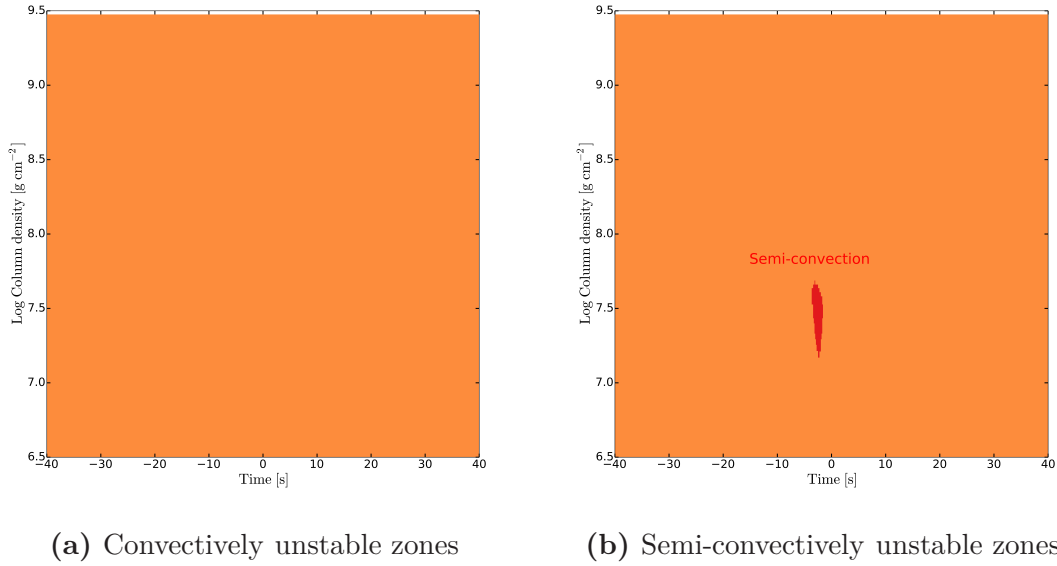


Fig. 5.6 The convection and semi-convection in function of column density and time. The time-axis coincides with the peak burst luminosity. The heating at the inner boundary is set to 1.5 MeV/nuc and the accretion rate is $\dot{M}_{acc} = 10^{17}$ g/s

disappears at strong heating at the inner boundary. We therefore found that the size of the convective zone depends on heating: The stronger we heat, the less prominent the convection appears in our calculations. You should note that semi-convection is not included in our calculations (see Chapter 2). All in all, convection seems not to play a major role in the current setup.

The peak luminosity of an X-ray burst is an indicator of how far the explosive *rp*-process proceeds before being slowed down due to non-degenerate conditions, strong cooling or lack of fuel. It also helps to identify the ratio between hydrogen and helium at the ignition depth. Figure 5.7 shows the quiescence and peak luminosity as a function of crustal heating at the innermost zone. By the reason that in a sequence of burst, peak as well as quiescence luminosities might vary, we took the average over 100 bursts. We define the quiescence luminosity as the minimal redshifted luminosity between two bursts. On the other side, the peak luminosity corresponds to the maximal luminosity during a single burst as seen from infinity.

In general, the increase in heating at the innermost zone leads to a slight increase in quiescence luminosity. Indeed, applying a heating and hence an additional luminosity at the inner boundary results naturally in an enhancement of the quiescence luminosity. Contrariwise, the peak luminosity is decreasing with an additional crustal heating

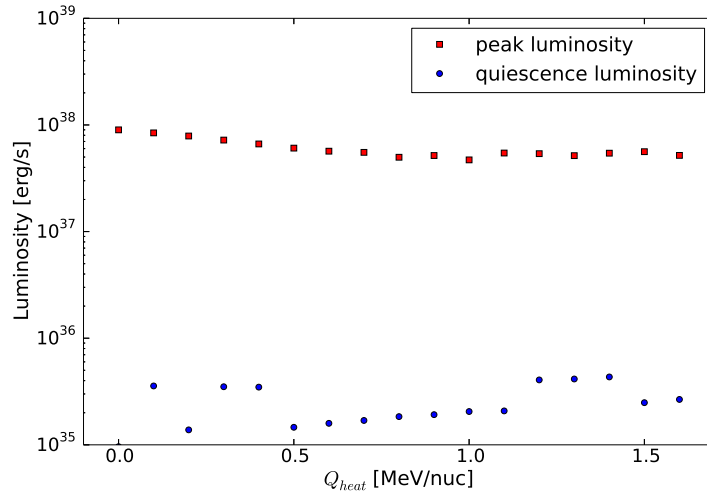


Fig. 5.7 The figure shows the peak luminosity (red squares) and the quiescence luminosity (blue circles) as a function of the heating at the inner boundary. The values have been obtained by averaging over a sequence of 100 bursts.

source. This can be understood by the shift of the ignition point to lower densities and higher temperatures where the explosive rp -process is stopped earlier due to less degenerate conditions.

The shape of the light curve of an X-ray burst can provide even more information about the reaction flow during a burst and the heat transport in the ignition layer. In Figure 5.8 we show a comparison of the burst luminosity between a model with a rather moderate heating of $Q_{\text{heat}} = 0.5$ MeV/nuc and a model with rather high heating of $Q_{\text{heat}} = 1.5$ MeV/nuc. We found not only a weakening of burst peak luminosity but also a faster decay with models of rather high heating at the inner boundary. In fact, the burst decay tail is depending strongly on the boundary heating in our simulations. The lower the heating, the less steep the burst decay after burst peak luminosity.

A slow cooling after the explosive runaway is caused by an inefficient heat transport in the ignition layer. Heat transport is strongly depending on the density, temperature and composition. An appropriate tool to determine the heat transport in the layers of a neutron star is the opacity. Figure 5.9 shows the different contributions to the total opacity as a function of the column density. Independent of the amount of heating at the inner boundary, the radiative opacity is dominating at the X-ray burst ignition depth. However, we found larger total opacities in the ignition layer of models with reduced boundary heating. A low total opacity is more efficiently transporting heat and therefore, models with high crustal heating at the inner boundary are able to cool

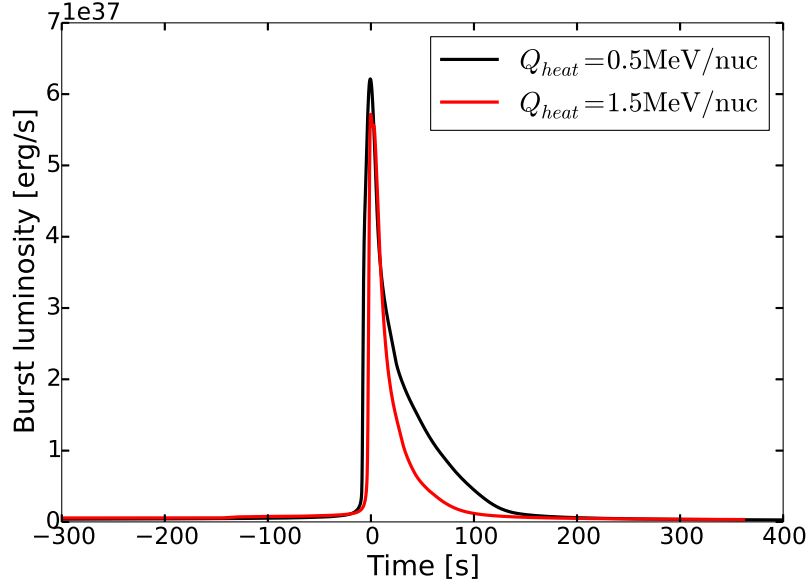


Fig. 5.8 The figure shows the burst luminosities for a model with $Q_{heat} = 0.5$ MeV/nuc (black line) and a model with $Q_{heat} = 1.5$ MeV/nuc (red line). The time axis is chosen such that the peak luminosities of the two bursts coincide.

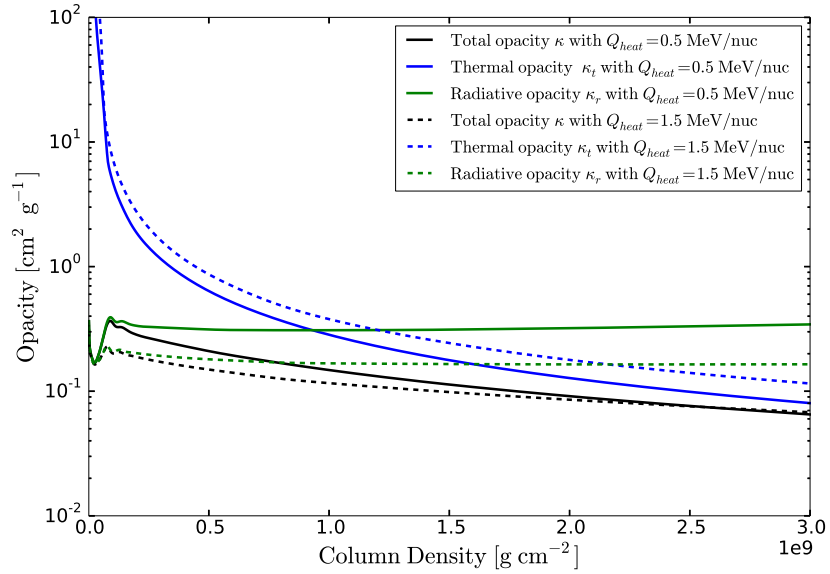


Fig. 5.9 The figure shows a comparison of the opacities between two bursts in function of the column density. The blue line is the thermal opacity, green corresponds to the radiative opacity and the black line is the total opacity. The solid profile shows the solution at $Q_{heat} = 0.5$ MeV/nuc and the dashed profile indicates the solution at $Q_{heat} = 1.5$ MeV/nuc

faster after an outburst.

You should note that a less steep decay of the burst luminosity might also be caused due further nuclear reactions at the ignition zone. Possibly, matter could burn in a stable manner during the cooling phase. Indeed, we found that surviving helium is involved in α -capture reactions during the burst decay.

However, the situation is different at depth where the thermal opacity dominates.

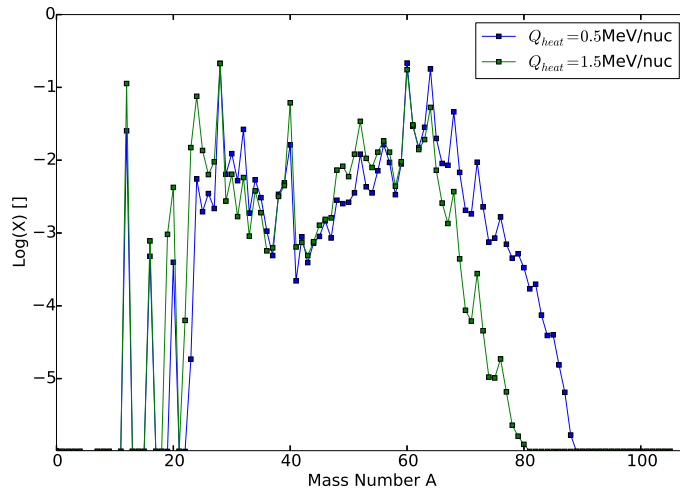


Fig. 5.10 The composition of the ashes at a density of $8 \cdot 10^6 \text{ g/cm}^3$ for a model with 0.5 MeV/nuc (blue line) and a model with 1.5 MeV/nuc (green line). The y-axis indicates the logarithm of the mass fraction of the corresponding isotopes with a given mass number. The profile is shifted to isotopes with higher mass number if the heating is set to a lower value.

Between the ignition layer of X-ray bursts and the ignition zone of superbursts, the thermal opacity is determining the heat transport. At those depths, we found a slight increase in the total opacity by reducing the term of crustal heating. The explanation of such a behavior is simple: X-ray bursts with high peak luminosity and thus with low heating at the innermost zone do produce heavier ashes, see Figure 5.10. X-ray bursts with ignition at high densities and lower temperatures generate compositions with high mass numbers. Since the composition of ashes influences the thermal opacity, heat is transported easier between the X-ray burst and superburst ignition depth in models with low heating at the inner boundary, see also in Figure 5.9.

Models with high values of Q_{heat} generate ashes with a larger abundance of isotopes below the mass number of 40. In terms of the ignitions of superbursts, especially ^{12}C is of great importance. In Figure 5.11, we plotted the crust heating versus the mass

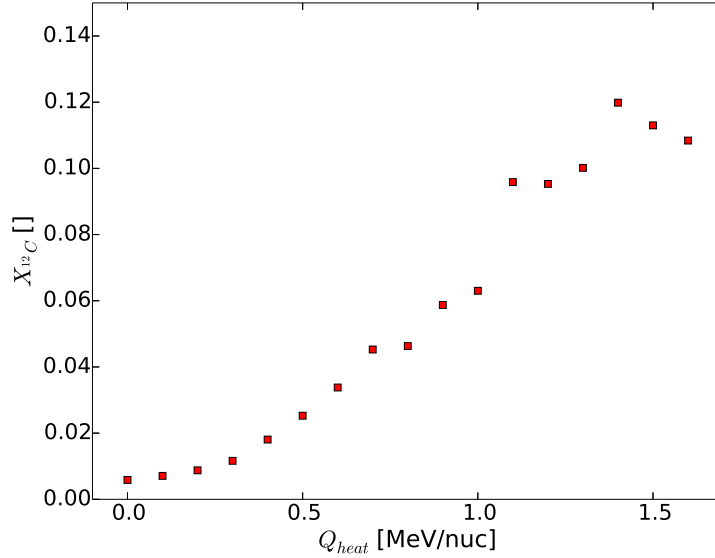


Fig. 5.11 Mass fraction of ^{12}C for different heating sources Q_{heat} using a constant accretion rate. The amount of ^{12}C is calculated at a density of $8 \cdot 10^6 \text{ g/cm}^3$, averaged over a sequence of a few hundreds of X-ray bursts.

fraction of ^{12}C at a density below the X-ray ignition zone, averaged over a time range of a few weeks of regular X-ray bursts. The amount of carbon is calculated at a depth where neither hydrogen nor helium is available for the whole range of Q_{heat} . As a result, the mass fraction of carbon in the ashes of X-ray bursts is increasing with increasing heating at the innermost zone. In order to generate ashes with $X_{^{12}\text{C}} \gtrsim 0.1$, one would need to apply a heating of $Q_{\text{heat}} > 1.0 \text{ MeV/nuc}$ in the current setup.

As a short summary, the additional heating at the inner boundary of our computational domain leads to lower recurrence times of X-ray bursts. The ignition is shifted to layers with higher temperatures but lower densities. Due to this fact, the quiescence rp -process is enhanced which leads to weaker bursts with low peak burst luminosities and thus lighter isotopes in the ashes. Since the opacity is affected by temperature, density and composition, the burst decay phase is depending on the applied crustal heat at the innermost zone of our computational domain. All the effects have a large impact on the mass fraction of ^{12}C in the ashes of X-ray bursts: The higher the crust heating in our model, the more carbon is found in the layers of X-ray burst ashes. While one would in terms of superburst ignition favor models which produce large amount of carbon, the heating does influence observable properties of X-ray bursts. Observations of X-ray bursting objects provide constraints on recurrence times as well

as on the burst luminosity curve. Therefore, we will discuss in the following section, how one can add an additional heating source while still maintaining the basic observed features of an X-ray burst light curve. In a first step, we will vary the accretion rate and compare the resulting properties of simulated X-ray bursts with observational data. In a second step, we will study in more detail the importance of accretion composition.

5.2 Observable properties and crustal heating

A heating source at a density region below the ignition zone of X-ray bursts influences observable properties such as the maximal burst luminosity and the recurrence time. However, the recurrence time is linked to the accretion rate which is poorly known for neutron stars in binary systems. A detailed analysis of X-ray burst sources concluded that typically, bursts have a recurrence time of 2 to 4 hours (Cornelisse et al., 2003; Galloway et al., 2008a; Keek et al., 2010; Stella et al., 1987). Nevertheless, there seems to be no obvious upper or lower limit on the observed recurrence time.

Each X-ray burst light curve is somehow unique and reveals some information about

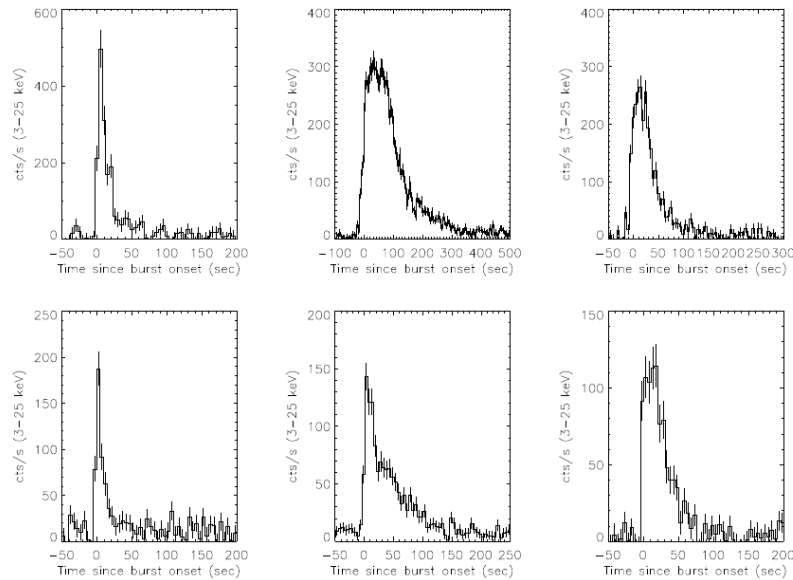


Fig. 5.12 The photon count rate in a energy range of 3 to 25 keV. You should note that each burst is unique, showing different burst durations and peak count rates. The light curves have been extracted from the JEM-X data set (Sánchez-Fernández, 2012).

the ignition conditions. A typical burst consists of a short rise time and a rather long

cooling tail, see Figure 5.12. Typical rise times are usually below 2 s, but some sources exhibit bursts with rise time up to 10 s. The observed X-ray burst decay time ranges from usually 10 s to several minutes, with most bursts having 10 to 80 s decay times (Bhattacharyya, 2010; Galloway et al., 2008b; Keek et al., 2010).

A further observable quantity is the ratio between integrated burst luminosity, L_{burst} , and the integrated accretion luminosity, defined as

$$\alpha = \frac{\int_t^{t+\Delta t} L_{acc} dt}{\int_t^{t+\Delta t} L_{burst} dt}, \quad (5.2)$$

where L_{acc} is the accretion luminosity and Δt the recurrence time between two bursts. A detailed study of observation data discovered that most X-ray burst sources exhibit an alpha value of around 100 (Galloway et al., 2008b). Superburster show significantly high alpha values up to a few thousand (In't Zand et al., 2003) which might indicate that stable burning occurs in the outer layers of such neutron stars.

In the following, we will discuss the impact on observational properties due to accretion rate changes and variation of the accreted composition.

5.2.1 Accretion Rate

An extra heating source at the boundary of our model reduced considerably the recurrence time of X-ray burst. As we would like to compare results with observations, we need models which fulfill the observed properties of accreting neutron stars in binary systems. Indeed, the X-ray burst recurrence time of a binary system is easy and precisely to determine and therefore, it should be a strong constrain for numerical X-ray burst simulation. Unfortunately, most X-ray bursting neutron stars show in long time range observations irregular bursting behavior. It is thought, that such irregular bursts occur due to variation in the accretion rate. Full X-ray burst observations over a whole time range of a few years before the ignition of a superburst are not available and therefore, it is not possible to discuss in details how the irregular X-ray burst influence the production of ^{12}C . Some first simplified attempts of long term accretion rate variation studies have been made in Hashimoto et al. (2014) and show that accretion rate changes might help to explain the ignition of a superburst. However, we adopt here for the discussion of the importance of the accretion rate four different models, each with constant accretion rates:

Model	Accretion rate [g/s]	Accretion rate [\dot{M}_{edd}]
Low accretion rate	$0.5 \cdot 10^{17}$	0.026
Standard accretion rate	$1.0 \cdot 10^{17}$	0.053
Intermediate accretion rate	$1.5 \cdot 10^{17}$	0.079
High accretion rate	$2.0 \cdot 10^{17}$	0.105

Table 5.1 The description of the accretion rate models used in the current study.

As a result of the previous section, we found that heating shifts the ignition point of

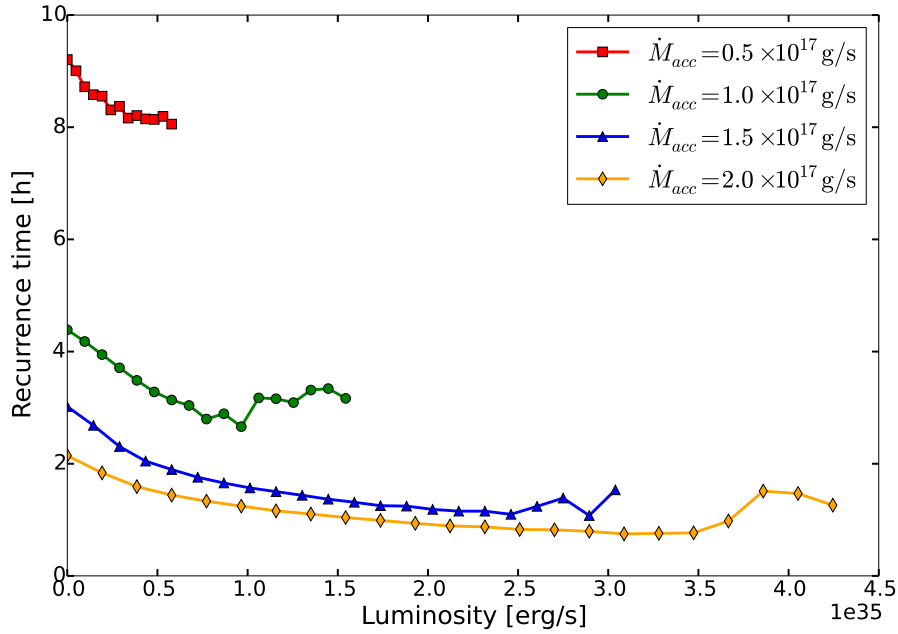


Fig. 5.13 The recurrence time in function of the luminosity at the inner boundary for models with different accretion rates.

X-ray bursts to lower densities but higher temperature, having therefore an impact on the recurrence time of the bursts. To make things even more complicated, a change in accretion rate varies the amount of accreted fuel for a given time range which strongly influences burst recurrence time as well. Figure 5.13 displays the recurrence time of X-ray burst for the different accretion rates. Since Q_{heat} is defined in units of MeV per accreted nucleon and thus linked to the accretion rate, one should compare the recurrence time of the models in function of the boundary luminosity given as

$$L_{crust}^{\infty} = \frac{Q_{heat}}{m_u} \dot{M}_{acc} c^2, \quad (5.3)$$

where L_{crust}^{∞} is the boundary luminosity as seen from infinity, m_u is the atomic mass unit and \dot{M}_{acc} is the accretion rate. For each model, we increase the heating at the inner boundary of our computational domain in steps of 0.1 MeV/nuc until ignitions of X-ray bursts are stopped due to a change from the unstable to the stable burning. We found that recurrence time is strongly linked to the accretion rate: High accretion rates lead to a short recurrence time, whereas very low accretion rates exhibit X-ray bursts with a rather long recurrence time of 8 to 10 hours. Further, the recurrence time tend to decreases with increasing boundary luminosity. Just before the ignition of X-ray bursts ceases due to stable burning, all our models showed large fluctuations in the recurrence times. Such a irregular behavior at high luminosity is in agreement with results found in Zamfir et al. (2014). We account those fluctuations also to an enhancement of the convection at the outer layers of the neutron star. Since the ignition is shifted towards the surface of the neutron star, the contribution of convection is amplified.

A large boundary luminosity above $L_{crust}^{\infty} > 1.5$ erg/s together with the occurrence of explosive burning (X-ray bursts) can only be achieved with accretion rate models which fulfill $\dot{M}_{acc} > 10^{17}$ g/s. As a conclusion, if one would need to apply a high boundary luminosity as found in Turlione et al. (2013), we would be forced to use our current models higher accretion rates in order to do simulations of X-ray bursts. However, this conclusion only holds in case of solar composition accretion in the current setup.

Since each single X-ray burst produces a large amount of heat, short recurrence times imply that the computational domain is not yet cooled down from previous burst and thus, the temperature is elevated in comparison with models with long recurrence times. In Figure 5.14 we compare the temperature of the computational domain just before a X-ray burst ignition takes place. While placing no additional heating at the inner boundary, we found that the temperature just before burst is linked to the accretion rate.

The recurrence time of burst depends sensitively on the ignition conditions. To understand why the accretion rate strongly affects the recurrence time, one has to study the ignition conditions at different accretion rates. Figure 5.16 shows the burn rate at different times and column densities for a model with accretion rate of $5 \cdot 10^{16}$ g/s and $2 \cdot 10^{17}$ g/s. A comparison of the burn rates shows that at high accretion, the ignition point is pushed to higher column densities which is in agreement with Matsuo et al. (2011). This means that while additional heating shifts the ignition conditions to higher temperature but lower densities, an increase in accretion rate results in a X-ray

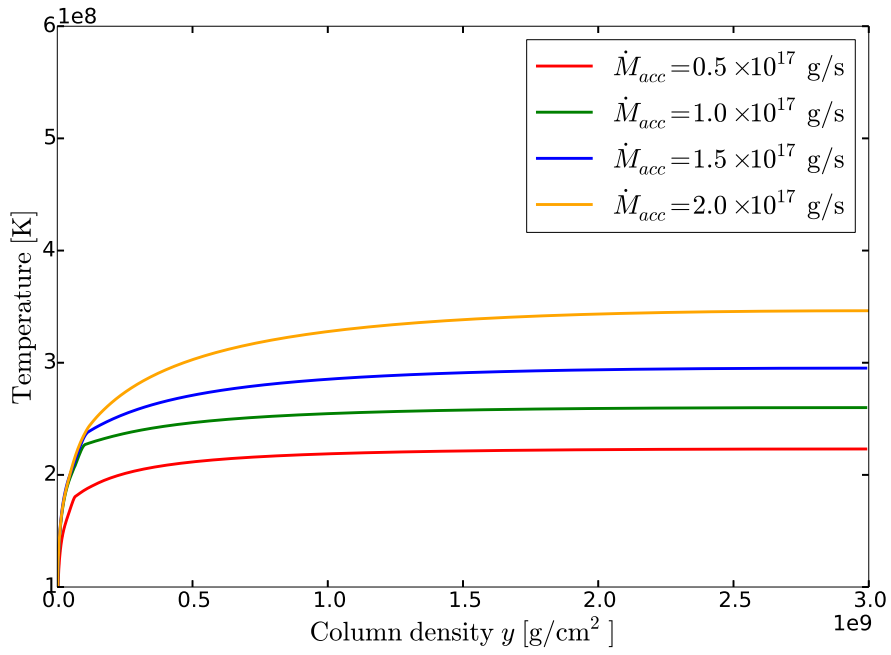
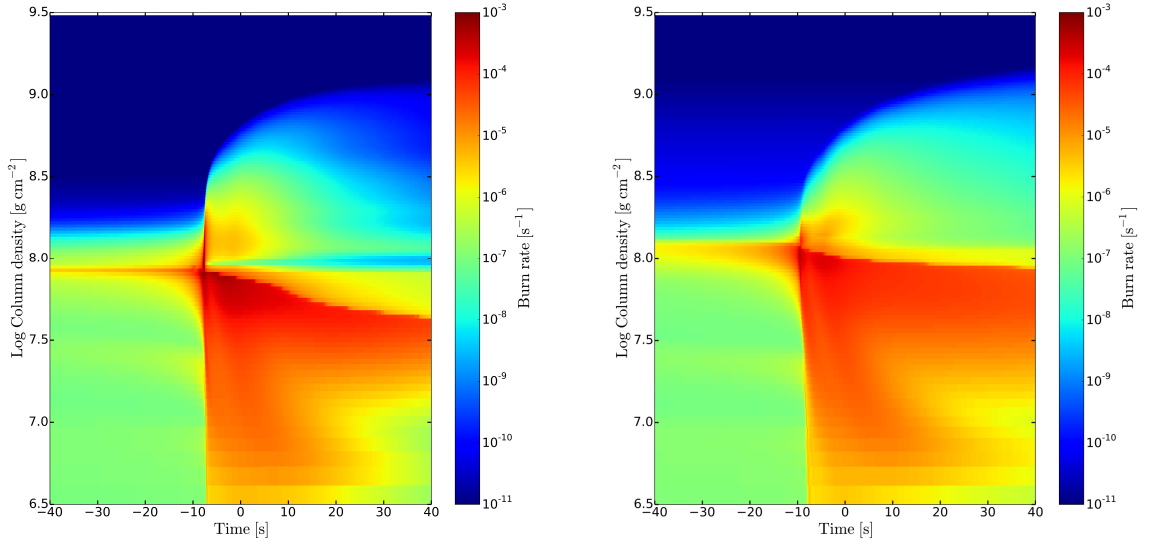


Fig. 5.14 The figure shows the temperature profiles before the ignition of an X-ray burst for $\dot{M}_{acc} = 5 \cdot 10^{16}$ g/s (red line), $\dot{M}_{acc} = 10^{17}$ g/s (green line), $\dot{M}_{acc} = 1.5 \cdot 10^{17}$ g/s (blue line) and $\dot{M}_{acc} = 2 \cdot 10^{17}$ g/s (orange line). For all models, we used no additional heating at the inner boundary ($Q_{heat} = 0$ MeV/nuc).



(a) Kippenhahn diagram of the burn rate with $\dot{M}_{acc} = 5 \cdot 10^{16}$ g/s.

(b) Kippenhahn diagram of the burn rate with $\dot{M}_{acc} = 2 \cdot 10^{17}$ g/s.

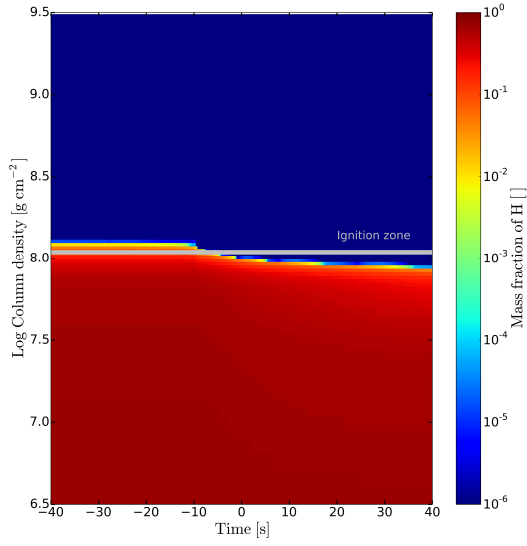
Fig. 5.15 The burn rate in function of the column density and time. The time $t = 0$ s coincides with the burst peak luminosity. For both accretion rate models, we used zero additional heating at the inner boundary.

burst ignition at higher densities but also higher temperature. This is at first sight an unusual behavior since more amount fuel has to be accreted to reach the ignition point at high densities and therefore one would at first sight expect an increase in recurrence time. Why is the recurrence time small at high accretion rate? The answer lies in the ignition zone of the explosive burning. Comparing the mass fraction of hydrogen and helium in function of time and column density (see Figure 5.16), we found that in the ignition zone of a low accretion rate model some hydrogen has been burned to helium even shortly before the burst takes place. In other words, at low accretion, a helium dominated burst is taking place, whereas at higher accretion, we found a mixed hydrogen/helium burst (Keek and in Zand, 2008). The time to accumulate the fuel can be determined by

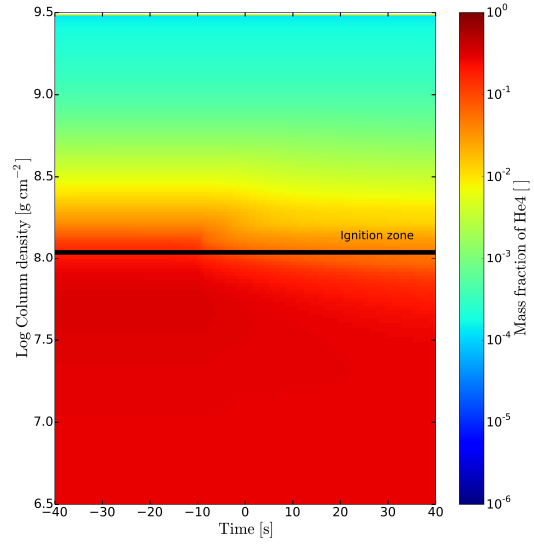
$$t_{fuel} = \frac{4\pi R^2 y_{ign}}{\dot{M}_{acc}}, \quad (5.4)$$

where y_{ign} is the column density in the ignition zone, R is the radius and \dot{M}_{acc} is the accretion rate. Applying the conditions of our accretion rate models, we found:

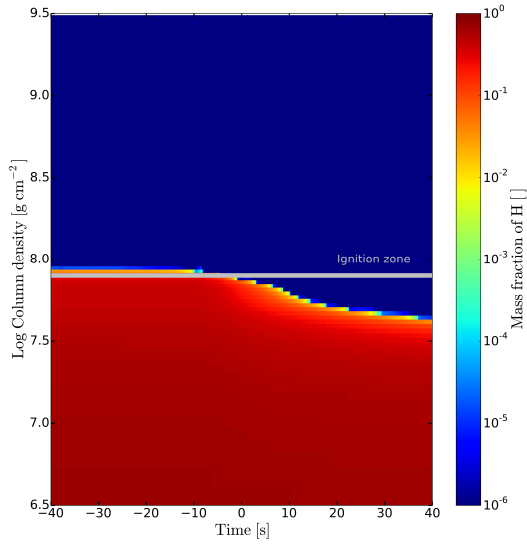
While all helium and hydrogen in a wide range around the ignition zone is depleted during a strong burst with low accretion models (see Figure 5.16c and Figure 5.16d),



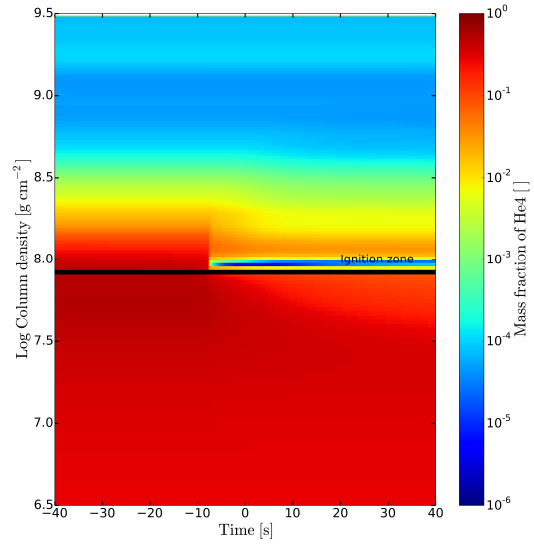
(a) The mass fraction of hydrogen in function of column density and time with $\dot{M}_{acc} = 2 \cdot 10^{17}$ g/s. The silver shaded area indicates the burst ignition layer.



(b) The mass fraction of helium in function of column density and time with $\dot{M}_{acc} = 2 \cdot 10^{17}$ g/s. The black shaded area indicates the burst ignition layer.



(c) The mass fraction of hydrogen in function of column density and time with $\dot{M}_{acc} = 5 \cdot 10^{16}$ g/s. The silver shaded area indicates the burst ignition layer.



(d) The mass fraction of helium in function of column density and time with $\dot{M}_{acc} = 5 \cdot 10^{16}$ g/s. The black shaded area indicates the burst ignition layer.

Fig. 5.16 The time axis is chosen such that the burst peak luminosity is at $t = 0$ s. To get a correct comparison, we used zero additional heating at the inner boundary.

$\dot{M}_{\text{acc}}/\dot{M}_{\text{edd}} [\text{g s}^{-1} \text{ cm}^{-2}]$	$y_{\text{ign}} [\text{g cm}^{-2}]$	$t_{\text{fuel}} [\text{h}]$	$X_H []$	$X_{He} []$
0.026	$7.9 \cdot 10^7$	6.94	0.104	0.312
0.053	$8.4 \cdot 10^7$	3.69	0.332	0.294
0.079	$9.7 \cdot 10^7$	2.84	0.256	0.258
0.105	$1.1 \cdot 10^8$	2.42	0.118	0.155

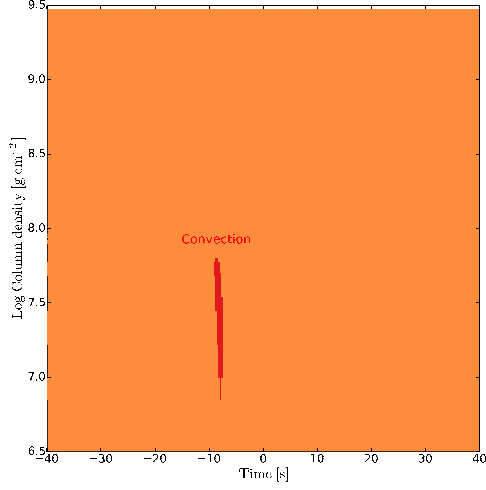
Table 5.2 Ignition conditions at different accretion rates

a significant fraction of helium is surviving the burst at high accretion rate, see Figure 5.16b. The helium which survives the burst is burning in a stable manner to ^{12}C in the layers of X-ray burst ashes.

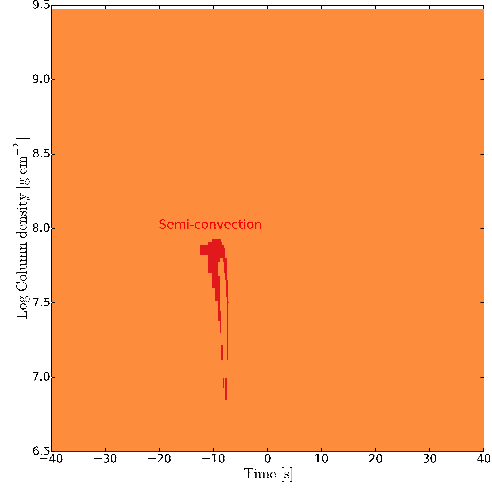
In addition to the change in composition at ignition depth, we found that at high accretion rate, less new fuel is required to ignite a X-ray burst, see above in Table 5.2. Indeed, the time t_{fuel} to accrete a new layer of fuel is decreasing with increasing accretion rate. This is linked to the fact that a breakout of the hot CNO cycle, and therefore the ignition of a X-ray burst, requires hot and dense conditions which are strongly present at high column depths. It is therefore somehow easier to ignite a X-ray burst in deeper layers of a neutron star.

In general, observations of X-ray bursts reveal a typical recurrence time of of 2 to 4 hours (Cornelisse et al., 2003; Galloway et al., 2008a; Keek et al., 2010; Stella et al., 1987). With solar accretion composition in the current setup, simulations with accretion rate between roughly $1.0 - 2.0 \cdot 10^{17} \text{ g/s}$ ($0.053 - 0.105 \dot{M}_{\text{edd}}$) are able to reproduce such typical recurrence times. As a comparison, observations of neutron stars which exhibit superbursts reveal a typical accretion rate in the range of 0.1 to $0.2 \dot{M}_{\text{edd}}$ before the ignition of superburst (see Chapter 1) which indicates that our accretion rates are a factor of two to low. We denote this problem to the fact that we are simulating with a simple 1D setup which does not consider local accretion rate changes and other 3D effects. It is therefore yet very ambitious to conclude from the results of our simulations about the accretion rate which one can observe in a binary system.

The variations in accretion rate change conditions in our computational domain and therefore influence the appearance of convection. The convection is not directly observable, but since it is one of the weakness of our simulation code, one should consider convectively unstable zones in more details. Figure 5.17 and Figure 5.18 show the appearance of convection and semi-convection at a low accretion rate of $\dot{M}_{\text{acc}} = 5 \cdot 10^{16} \text{ g/s}$ respectively at a high accretion rate of $\dot{M}_{\text{acc}} = 2 \cdot 10^{17} \text{ g/s}$. We found that the convection and semi-convection is enable during a short time range at

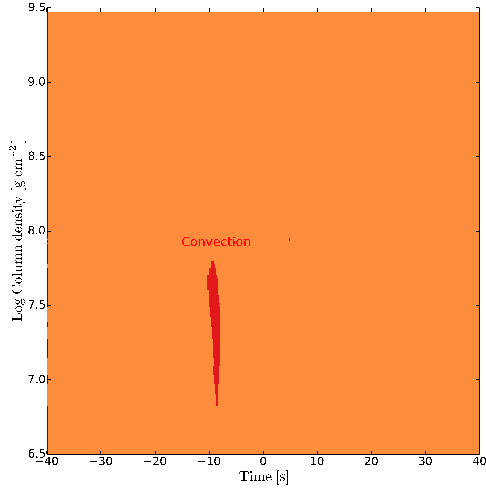


(a) Convectively unstable zones

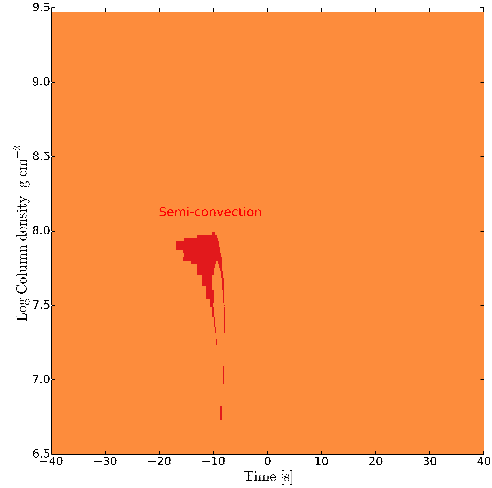


(b) Semi-convectively unstable zones

Fig. 5.17 The convection and semi-convection in function of column density and time. The time-axis coincides with the peak burst luminosity. The heating at the inner boundary is set to zero and the accretion rate is $\dot{M}_{acc} = 5 \cdot 10^{16}$ g/s



(a) Convectively unstable zones



(b) Semi-convectively unstable zones

Fig. 5.18 The convection and semi-convection in function of column density and time. The time-axis coincides with the peak burst luminosity. The heating at the inner boundary is set to zero and the accretion rate is $\dot{M}_{acc} = 2 \cdot 10^{17}$ g/s

the ignition till just before peak luminosity. As denoted in Chapter 2, the simulation does not include semi-convection. In addition, since we assume spherical symmetry, true convection is only included as an crude approximation. Comparing convection at low and high accretion rates, we found that the weakness of our code is more prominent at higher accretion rate. However, since the convection is taking place over a time span of the order of 5 second for low and high accretion rates, we can safely use our crude convection model for this study.

The accretion rate of fuel has not only a strong impact on the recurrence time, but it

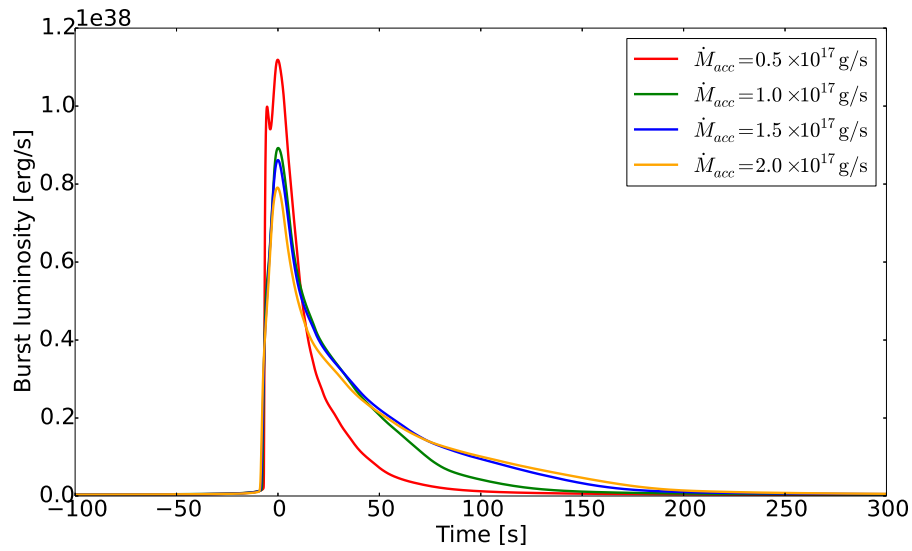


Fig. 5.19 The burst luminosity as seen from infinity for different accretion rate models. The red line corresponds to an accretion rate of $5 \cdot 10^{16}$ g/s and the green corresponds to 10^{17} g/s. Further, the blue line shows the burst luminosity for a model with accretion rate of $1.5 \cdot 10^{17}$ g/s and the orange one shows the burst luminosity for an accretion rate of $2 \cdot 10^{17}$ g/s. All solutions have been obtained with zero additional heating at the inner boundary ($Q_{heat} = 0$ MeV/nuc).

plays also a leading role on the shape of the resulting burst luminosity. By the reason that thousands of X-ray bursts have been observed, the shape of the burst luminosity light curve is a practical feature to compare with numerical simulations. In figure ?? we display typical light curves at different accretion rates with zero additional boundary luminosity ($Q_{heat} = 0$ MeV/nuc). You should note that each X-ray burst is somehow unique and one should expect small deviations in the burst luminosity of a given model and accretion rate. In general, the accretion rate has an eminent influence on the observable luminosity during an X-ray burst. As a result, we found that the maximal burst luminosity is decreasing with increasing accretion rate. While

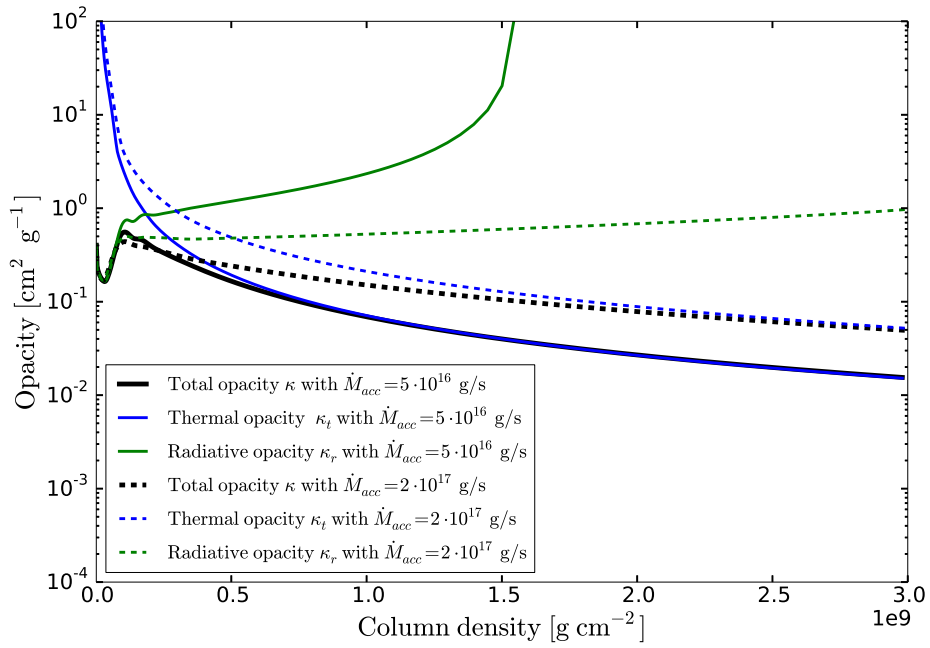
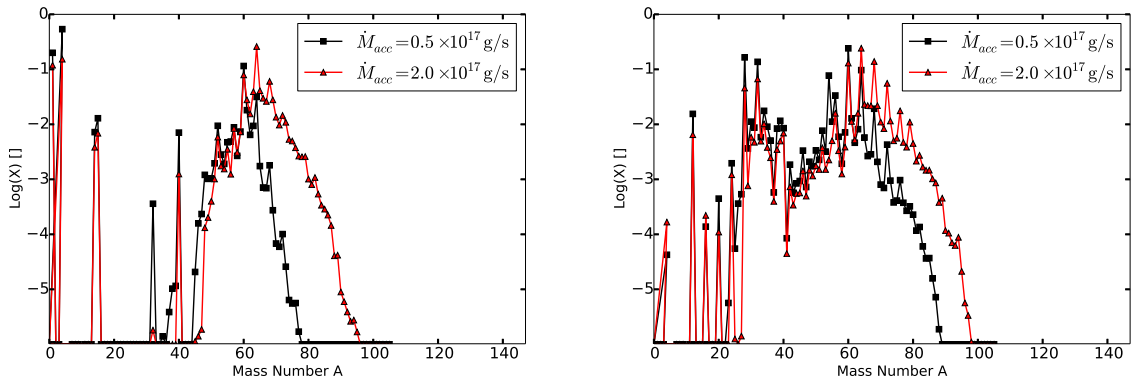


Fig. 5.20 The opacity between two X-ray bursts for a simulation with an accretion of $5 \cdot 10^{16}$ g/s (solid profile) and an accretion of $2 \cdot 10^{17}$ g/s (dashed profile). The x-axis denotes the column density. The black line is the total opacity, the blue line corresponds to the thermal opacity and the green line is the radiative opacity. The solutions have been obtained with zero heating at the inner boundary.

the rise time of the burst luminosity indicates to which isotopes in the higher mass range the explosive reaction flow proceeds, the burst peak luminosity depends mainly on the composition at the ignition zone. As you can see in Table 5.2, the amount of helium in the layer of fuel at the ignition conditions is decreasing with increasing accretion rate. Calculations of helium flashes in Fisker et al. (2004); Hōshi (1980); Matsuo et al. (2011) have demonstrated that helium bursts tend to have high peak luminosities. Further, helium bursts are characterized by a double peak, see also in Figure 5.19. Two major effects are responsible for the appearance of double peaks: Convective transport of the helium flash energy (first peak) and the nuclear waiting point and its subsequent flow out of waiting point (second peak).

The cooling, what means the decay of the luminosity after the peak, is steeper at lower accretion rate. This makes sense since at low accretion rate, the cooling between two bursts is much stronger due to the large recurrence time. Additionally, the ignition of X-ray burst is shifted to lower densities with decreasing accretion rate. Those two burst condition enable in general a very efficient cooling after peak luminosity. The heat transport is not fully determined by temperature, density and temperature gradient. Indeed, the opacity plays a crucial role in physics of the heat flux.

Figure 5.20 shows the opacity of the model with lowest accretion rate in comparison



(a) The composition at ignition depth for high and low accretion.

(b) The composition below the ignition depth for high and low accretion

Fig. 5.21 The composition at the ignition depth just before the ignition takes place (left figure) and the composition below the ignition depth at the inner boundary (right figure). The red line corresponds to an accretion rate of $2 \cdot 10^{17}$ g/s, whereas the black line corresponds to $5 \cdot 10^{16}$ g/s. The x-axis indicates the mass number and the y-axis corresponds to the logarithm of the mass fraction. You should note that the crustal heating has been set to zero for both simulations.

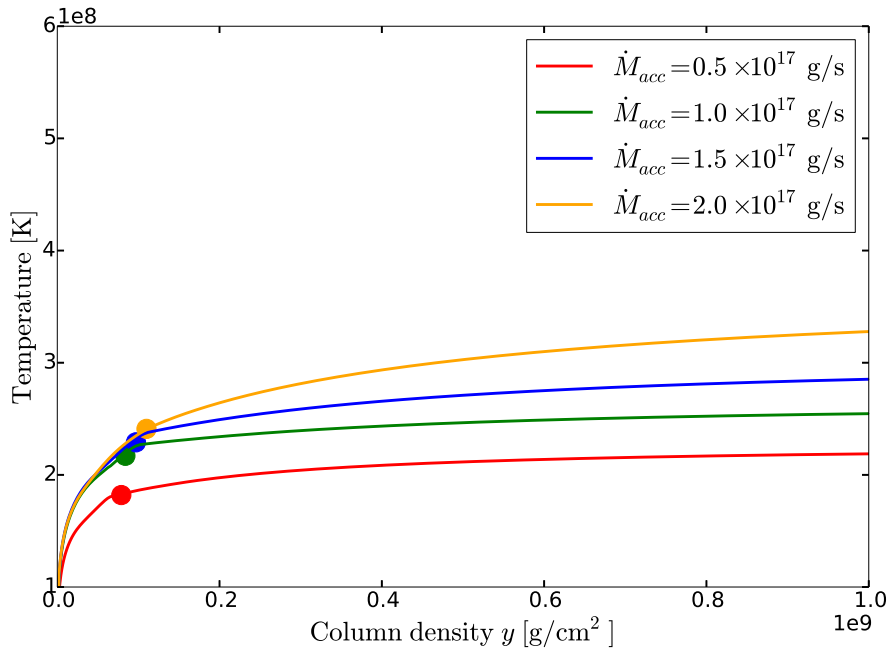


Fig. 5.22 The figure shows the temperature profiles before the ignition of an X-ray burst for $\dot{M}_{acc} = 5 \cdot 10^{16}$ g/s (red line), $\dot{M}_{acc} = 10^{17}$ g/s (green line), $\dot{M}_{acc} = 1.5 \cdot 10^{17}$ g/s (blue line) and $\dot{M}_{acc} = 2 \cdot 10^{17}$ g/s (orange line). The circle indicated the ignition conditions. For all models, we used no additional heating at the inner boundary ($Q_{heat} = 0$ MeV/nuc).

with the one with the highest accretion rate. The opacity is depending on the composition, temperature and density, and thus, due to the large difference in composition (see Figure 5.21), density and temperature (see Figure 5.22), we found significant differences in the opacities for simulations with the different accretion rates.

At low column densities, the radiative opacity is dominating for all accretion rate models. In fact, in the region of ignition, the total opacity of our low accretion rate model is slightly larger than the total opacity at high accretion rate. In principal, this indicates that heat is transported more efficiently in the outer layers of our models with high accretion rates. However, we found that the effect is quite small.

On the other side, in the layers of X-ray burst ashes, we found significant differences in the total opacity due to a different behavior of the thermal opacity. Indeed, the thermal opacity in the deeper layers of the neutron star is increased in our model with large accretion rate. Due to this fact, the total opacity below the ignition layer is larger at higher accretion rate. Such an increase in opacity leads to an rather inefficient transport of heat at given conditions.

While the opacity at the surface layers of a neutron star is not directly observable,

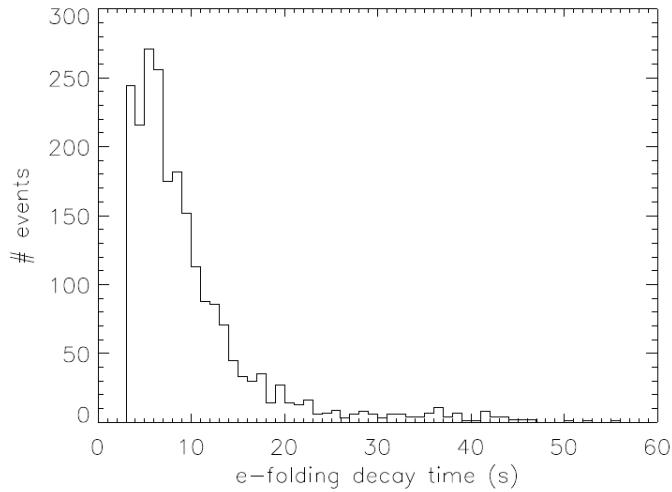


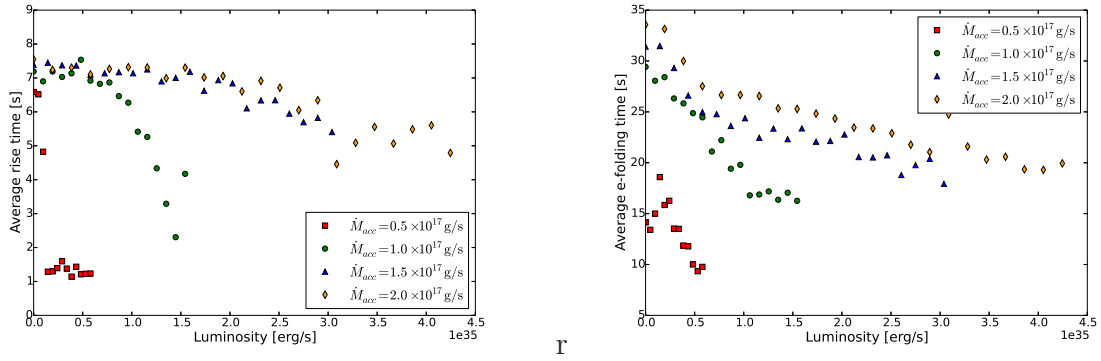
Fig. 5.23 The e -folding time of observations of a number of Type I X-ray bursts. The figure is adopted from Sánchez-Fernández (2012).

one can extract some information about the opacity at the ignition depth by calculating the steepness of the temperature drop after the peak luminosity. In general, the steeper the drop after peak burst luminosity, the higher the radiative conductivity and therefore the lower the opacity. The observed X-ray burst decay time ranges from usually 3 s to a minute (see Figure 5.24a), with most bursts having 6 to 10 s decay

times (Bhattacharyya, 2010; Galloway et al., 2008b).

A typical burst consists of a short rise time and a rather long cooling tail. Typical rise times are usually below 2 s, but some sources exhibit bursts with rise time up to 10 s. The observed rise time is providing some information about the composition at ignition and the constituents of the ashes of X-ray burst.

The average rise time of an X-ray burst in our simulations is given as



(a) Average rise time of X-ray burst with different accretion rates. (b) Average decay e -folding time of X-ray burst with different accretion rates.

Fig. 5.24 The e -folding time and rise time of X-ray bursts with different accretion rates in function of the crust luminosity at the inner boundary.

$$t_{rise} = t_{L=L_{peak}} - t_{L=2 \cdot L_{min}}, \quad (5.5)$$

where L_{peak} is the burst peak luminosity, L_{min} the minimal burst luminosity between two bursts and t the time as observed from infinity. The average decay time as measured from infinity is given as the e -folding time

$$t_{decay} = t_{\ln(L_{peak}/L)=1} - t_{L=L_{peak}}. \quad (5.6)$$

The average rise times of the models at different accretion rates cover a range of 1–8 s, see Figure 5.24a which is in agreement with observations (Galloway et al., 2008b; Paul et al., 2012). In general, we found that models with high accretion rate tend to have larger average rise time. This means that a short rise time of the order of a few seconds can only be achieved by our models with $\lesssim 10^{17}$ g/s. Besides, we found that the rise time of X-ray bursts is decreasing with increasing crust luminosity. At high crust luminosities, just before bursts cease and burning takes place in a stable manner, the rise time for each model shows large fluctuations.

The rise time of a X-ray burst mostly depends on the ratio of hydrogen to helium at the ignition layer, it is somehow less sensitive to the waiting points in the explosive *rp*-process (Fisker et al., 2008). As an example, since there is enough time to burn stably hydrogen to helium at low accretion rate, the burst rise time is much shorter. The additional heating at the inner boundary has an impact on the ratio of hydrogen to helium and thus, one can observe a variation of rise time in function of crustal heating. Further, a long rise time indicates that there is enough time for the explosive *rp*-process to proceed up to isotopes with large proton numbers. In other words, a long rise time enables the production of heavy elements, see Figure 5.21 for a comparison of the ashes.

On the other side, the average *e*-folding time of our simulations is in the range of 8 – 35 s, see Figure 5.24b. Common *e*-folding times of observed X-ray bursts are of the order of 10 s (Keek et al., 2010) and therefore agree well with our simulations. The decay time depends on the conductivity and the energy release from the β^+ -decay. As found in Chapter 3, our reduced 304 isotope network is not properly describing the β^+ -decay towards the valley of stability. One might therefore expect small shifts in the average *e*-folding time of our simulations.

At lower accretion rate, the recurrence time is larger and therefore, the outer layers are cooler. The lower temperature environment at the ignition point enables a faster cooling and thus, the average *e*-folding time is smaller. Increasing the crust luminosity shifts the ignition point of X-ray bursts to higher temperature but lower density. Due to those ignition conditions, bursts are weakened and cooling is much more efficient. Indeed, all our models show a decrease in the average *e*-folding decay time with increasing luminosity (see Figure 5.24b).

The ratio α of persistent fluence to burst fluence is an indicator for the energetics of a burst. To compare our result from simulations with the observed α -parameter, we need to add the accretion luminosity to the burst luminosity. We integrate the total luminosity as seen from infinity between two bursts to find the persistent fluence of a burst. The value of the burst fluence is given as the integrated luminosity during a X-ray burst. However, you should note that our calculations of the α -parameter only consider the bolometric burst energy and excludes neutrino emission from β^+ -decays.

Figure 5.25 shows the evolution of the α -parameter at varying crust luminosity. The majority of observed X-ray bursts have a α -parameter of slightly above 40 (Galloway et al., 2008b; Keek et al., 2010) which is well reproduced with our model at an accretion rate of 10^{17} g/s. However, superbursters have a large α -parameter (in Zand et al.,

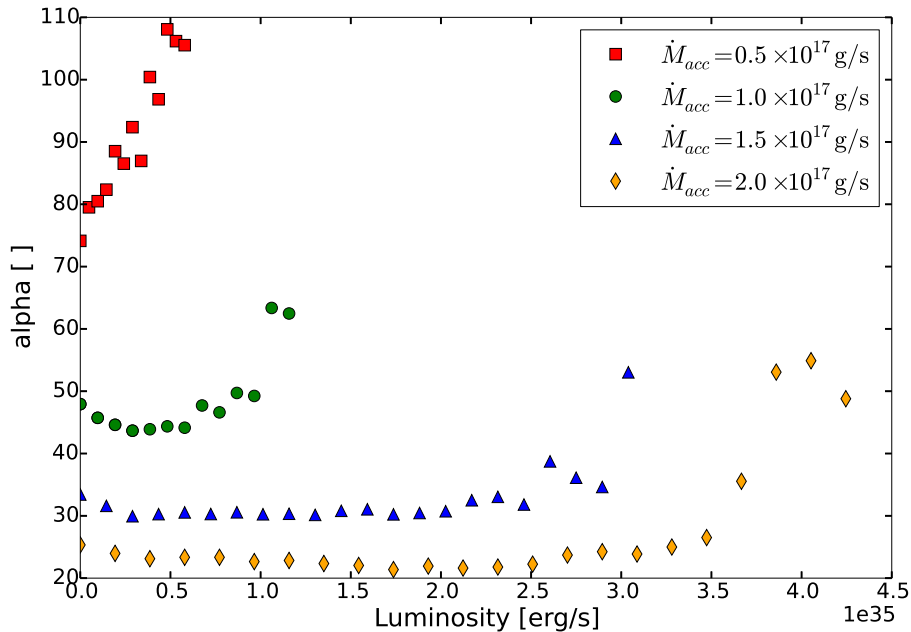


Fig. 5.25 The ratio α of persistent fluence to burst fluence for varying accretion rates and crust luminosities.

2004) which indicate that burning occurs in a stable manner at the surface of a neutron star. Our models with very low accretion rates are able to show α -parameter around 100, values above 110 are not obtained in the current setups. At large crustal heating just before the explosive burst disappears, X-ray bursts are irregular, fluctuating between explosive burning and stable burning. Such fluctuations lead to an increase in α -parameter.

X-ray burst do not ignite spherical symmetric and hence, the ignition generates a burning front which might not ignite the whole surface of a neutron star. The leftover of unburned fuel might then burn in a stable manner, leading to a large α -parameter (Cavecchi et al., 2014). Locally varying accretion rates or accretion rate fluctuations over time might also explain α -parameter of superbursters of the order of 10^3 since stable burning might occur in deeper layers.

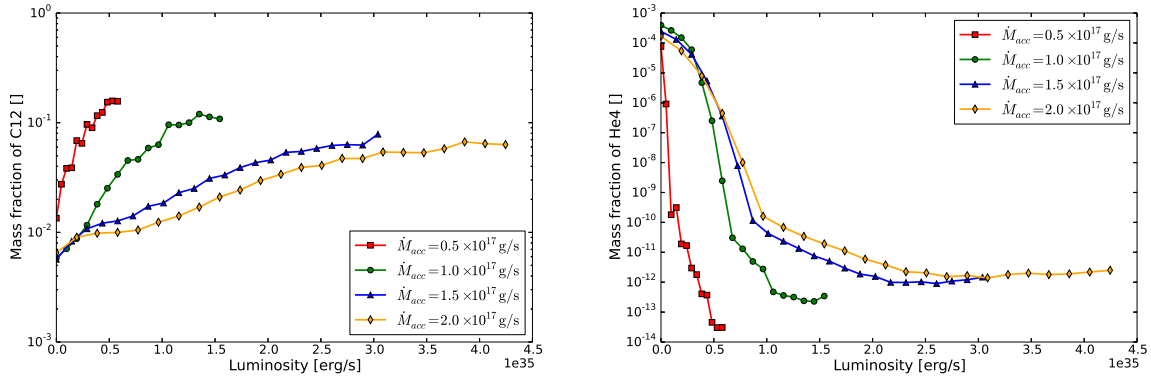
Besides the direct comparison with X-ray burst observations, one can also find further constraints by analyzing observations of superburst. Such long lasting bursts are thought to be ignited by unstable burning of carbon in the ashes of X-ray bursts. Observations reveal a superburst recurrence time of the order of a few years and thus, one

would require one of the following requirements to find enough carbon at the ignition of superburst:

- Helium burning stably to carbon below the ignition layer of X-ray bursts. In addition, a large amount of carbon needs to survive down to the ignition layer of superburst (Stevens et al., 2014).
- Carbon can be produced during an X-ray burst but is mostly destroyed by alpha-capture during the decay phase. Assuming that there would be no stable burning of carbon between the ignition depth of X-ray and superburst, one needs to prevent the destruction of carbon at the X-ray burst ignition region.

We assume here that all hydrogen at the ignition zone is fully burned during a X-ray burst and that there is no additional reservoir of carbon in layers below superburst ignition which could contribute to the fuel of a superburst (Peng et al., 2007). In general, we therefore need either a large fraction of carbon or helium in order to ignite a superburst within the observed time range.

The mass fraction of helium at the inner boundary is below 10^{-3} in all our models



(a) The mass fraction of carbon in the ashes of X-ray burst at the inner boundary of our model.

(b) The mass fraction of helium in the ashes of X-ray burst at the inner boundary of our model.

Fig. 5.26 The mass fraction of carbon and helium at a density of $9 \cdot 10^6 \text{ g/cm}^3$ for different accretion models. The x-axis denotes the crust luminosity at the inner boundary of our model.

and it decreases with increasing crust luminosity, see figure 5.26b. To produce enough carbon down to the ignition zone of superbursts, one would need a significantly higher mass fraction of helium. Calculations of Keek et al. (2012); Stevens et al. (2014);

Zamfir et al. (2014) indicate that one would need a carbon mass fraction of the order of 0.1 at the ignition depth of superburst. Therefore, the amount of helium would not suffice to contribute an important portion to the appearance of carbon at higher densities.

On the other side, while there is only a tiny amount of helium at higher densities, a considerable fraction of carbon survives the explosive runaway and exists in the ashes of X-ray bursts. Indeed, as seen in figure 5.26a, a low accretion rate as well as a high crust heating helps to make certain that a fraction of carbon survives a X-ray burst. The following table lists the maximal mass fraction of carbon and the heating one would require to produce a mass fraction of carbon larger than 0.1 in the ashes:

Model	Max mass fraction of carbon	Min Q_{heat} for $X_{12C} \geq 0.1$
Low accretion	0.158	0.8 MeV/nuc
Standard accretion	0.120	1.3 MeV/nuc
Intermediate accretion	0.078	-
High accretion	0.067	-

Table 5.3 Properties concerning the mass fraction of carbon in the ashes with different accretion rate models.

The setup of the intermediate accretion rate model as well as the setup of the high accretion rate model will not be able to trigger self-consistently a superburst since the carbon mass fraction in the ashes of X-ray bursts is probably too low.

As a short summery of the studies of accretion rate changes, we found a strong dependence between the accretion rate and the recurrence time of X-ray bursts. Therefore, one could in principle reproduce observations of recurrence time changes by applying accretion rate shifts. As an example, reducing the amount of matter accreted per second leads to an increase in burst recurrence time. We found further that the ignition zone is pushed to higher densities and higher temperature with increasing accretion rate. Such a shift influences the composition of fuel at ignition depth and varies the time to accumulate fresh fuel.

Peak luminosity as well as decay and rise time of the simulated X-ray bursts depend on the crustal heating and the accretion rate. We found quite good agreement with common observed X-ray burst luminosity properties. Changes in accretion rate have a significant impact on the composition in the layers of ashes: the lower the accretion rate, the lighter the composition of the ashes. To fulfill the observed superburst recurrence time, a large mass fraction of carbon is required. We found that heating at the

inner boundary as well as a low accretion rates helps to generate the required amount of ^{12}C .

However, the accretion rate is not the only uncertain parameter in our 1D simulations. A detailed description of the accretion composition is not yet available and might vary over time. In the next subsection, we will discuss the factor of the variations in the accretion composition.

5.2.2 Composition

Some of the superbursts are observed in X-ray bursting ultra compact X-ray binaries, for example 4U 0614+91 (Kuulkers et al., 2009) and 4U 1820-30 (Strohmayer and Brown, 2002). Such systems are characterized by a very low orbital period and are thought to have a compact companion star without a hydrogen envelope. This implies that neutron stars in ultra compact X-ray binaries systems accrete a composition consisting mainly of helium. Up to now, the ration between hydrogen and helium in the accreted matter can not be measured precisely and varies from system to system.

To investigate the effect of composition changes, we take the solar abundances and adopt the following abundances for hydrogen and helium in the accretion matter:

Model	Hydrogen mass fraction	Helium mass fraction	Rest
Hydrogen rich	0.824	0.157	0.019
Solar abundance	0.706	0.275	0.019
Helium rich 1	0.588	0.393	0.019
Helium rich 2	0.471	0.510	0.019
Heavy 1	0.693	0.270	0.037
Heavy 2	0.678	0.264	0.058

Table 5.4 Description of the models with variations in the accretion composition

You should note we are restricted by the choice of the accretion composition, as helium rich fuel will lead to very energetic bursts which can not be handled by our radiative zero photosphere boundary conditions at the surface of our model. We adopt here for the discussion two different helium-rich compositions where the mass fraction of hydrogen and helium is changed while keeping the mass fraction of the other isotopes constant. Further, very hydrogen-rich models are rather unrealistic but for completeness, we included a calculation with a hydrogen-rich accretion composition.

The mass fraction of isotopes beyond hydrogen and helium in the solar accretion

composition is below 2%. To test the importance of heavier isotopes in the accreted composition, we create models where we put the mass fraction of heavier isotopes to 4% respectively 6% but keeping the mass fraction ratio between helium and hydrogen constant. In other words, we replace a fraction of helium and hydrogen by heavier isotopes in the accretion composition.

All our accretion composition models accrete matter with a constant accretion rate

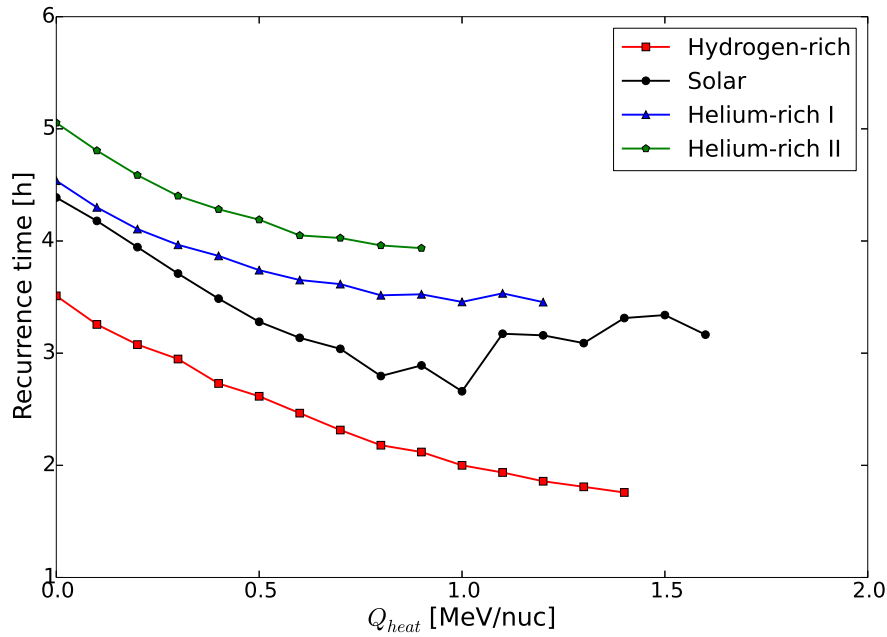


Fig. 5.27 The recurrence time in function of heating at the inner boundary. The red line with square markers corresponds to the hydrogen-rich model and the black line with circle markers indicates the model with a solar composition accretion. Further, the green line and the blue line denote the models with helium-rich accretion compositions. All the models are listed in Table 5.4.

of 10^{17} g/s which corresponds to $0.053\dot{M}_{edd}$ at solar composition accretion. We use outflow boundary conditions and run each simulations until an equilibrium cycle is reached. Due to this procedure, our models are independent of the initial progenitor file.

The hydrogen rich, solar abundance, helium rich 1 and helium rich 2 models enable us to analyze the effect of changes of the helium to hydrogen ratio in the accretion composition, see Table 5.4. A comparison of the solar abundance, heavy 1 and heavy 2 model helps us to determine the importance of the ratio between the mass fraction of hydrogen plus helium and the mass fraction of heavier isotopes.

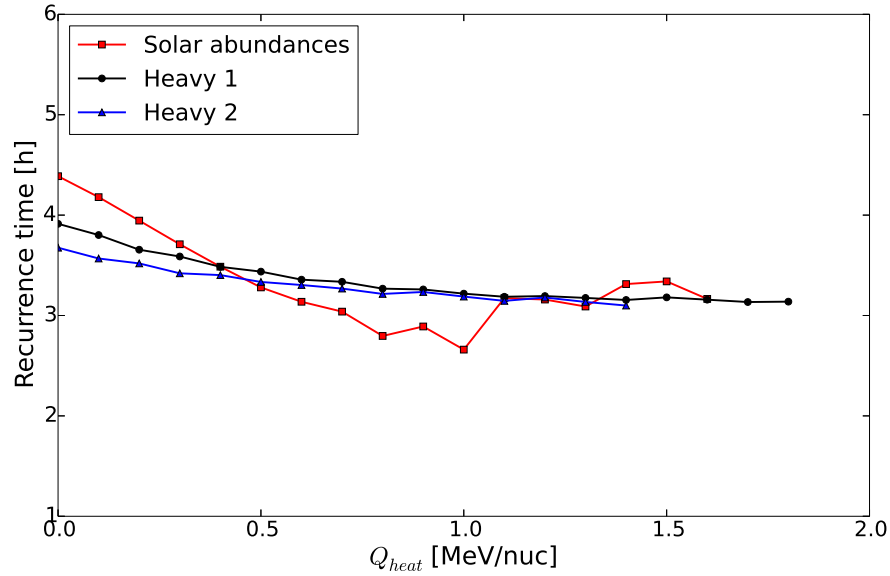


Fig. 5.28 The recurrence time in function of heating at the inner boundary. The red line with square markers corresponds to the model with solar accretion compositions, the black line with circle markers indicates the model heavy 1 and the blue line with triangle markers corresponds to the model heavy 2. All models are listed in Table 5.4.

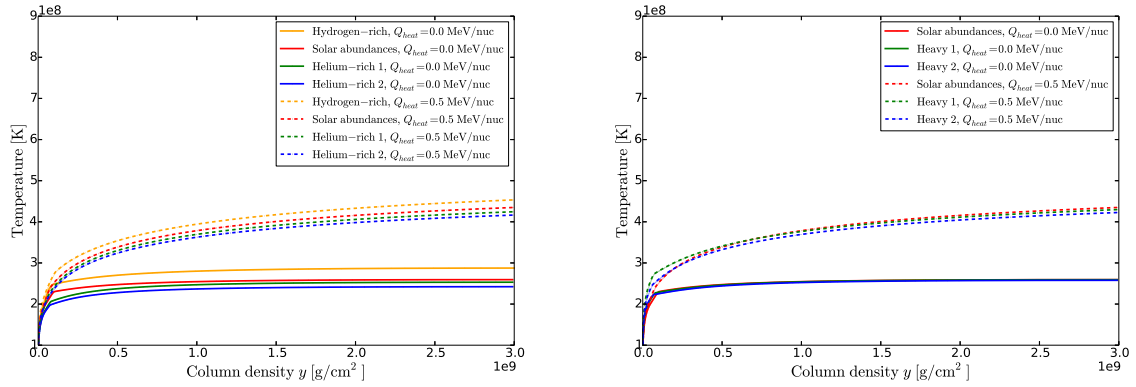
In Figure 5.27, we plotted the evolution of the recurrence time in function of crustal heating. As a result, we found that the recurrence time of X-ray bursts is depending on the ratio of hydrogen to helium mass fraction in the accretion composition. The more abundant the hydrogen in the accretion composition, the shorter the recurrence time. This means that the ignition of an X-ray burst is easier triggered in systems where the accretion composition consists of a considerable amount of hydrogen.

As a comparison, Figure 5.27 shows the recurrence time of X-ray bursts in function of heating at the inner boundary for various hydrogen/helium to heavier isotope ratios (see also Table 5.4). At zero boundary luminosity, the recurrence time of X-ray burst is decreasing with increasing fraction of heavier isotopes. The model heavy 1 and heavy 2 behave very similar with increasing crustal heating. However, the model with the largest mass fraction of heavier isotopes has proven to be much more resistant against stable burning. All three models in Figure 5.27 differ at maximum one hour in recurrence time. Therefore, as a result, recurrence times are more or less robust against variations in hydrogen/helium to heavier isotope ratios, but very sensitive to changes in the hydrogen to helium ratio. In other words, the amount of fuel (hydrogen and helium) is less important in the study of recurrence times of X-ray bursts than

the ratio of hydrogen to helium in the accretion composition.

Calculations of observational data of cooling neutron stars indicate that a large heating source is acting below the X-ray burst ignition zone (Shternin et al., 2011; Turlione et al., 2013). Using those results, our current setup would therefore exclude solution with large mass fraction of helium since burning occurs in stable manner at a boundary heating of $Q_{heat} > 1$ MeV/nuc. However, you should note that it is not yet clear how much heat of such a heating source is transported to the surface. The heating at our inner boundary is transported to the surface, while a real heating source would also heat the underlying layers. This means that we are only applying a fraction of the real heating calculated for example in Turlione et al. (2013).

Recurrence times of X-ray burst are not only easy to observe, but they also play a



(a) Temperature profile of different ratio of helium to hydrogen in the accretion composition

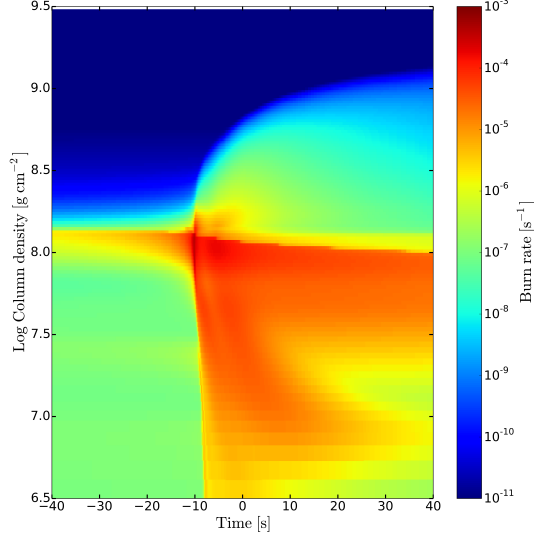
(b) Temperature profile of different ratio of mass fractions of hydrogen/helium to heavier isotopes in the accretion composition

Fig. 5.29 The temperature profile for different accretion compositions. The solid line corresponds to zero boundary heating, whereas the dashed line indicates the solutions with $Q_{heat} = 0.5$ MeV/nuc. For all models, the temperature has been calculated just before the ignition of a X-ray burst. All models are listed in Table 5.4.

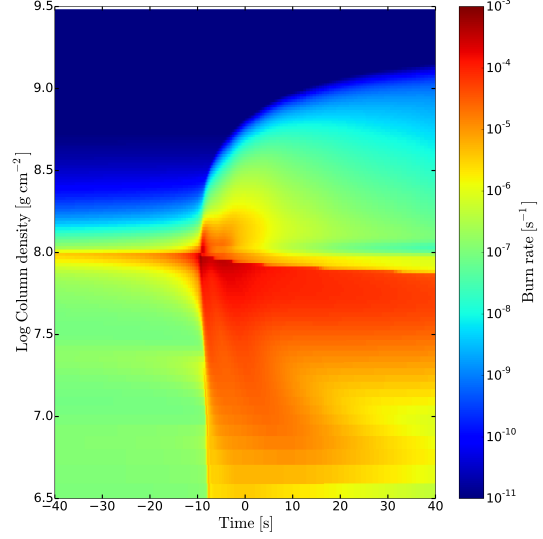
major role in the resulting temperature profile of the outer layers of a neutron star. As demonstrated in Figure 5.29a and Figure 5.29b, short recurrence time produce rather hot conditions in our computational domain. If the time between two subsequent burst is enlarged, the profile will be able to cool down considerably, resulting in a cooler profile just before the ignition of X-ray bursts take place. Since the recurrence time is strongly depending on the ratio of hydrogen to helium in the accretion composition, we found large variations in the temperature profiles at different hydrogen to helium ratios. As a comparison, the ratio of the mass fraction of hydrogen and helium to the

mass fraction of heavier matter seems not to play a crucial role in resulting temperature profile before burst ignition. In fact, the models with accretion composition of solar abundances, heavy 1 and heavy 2 have similar recurrence times of X-ray bursts, see Figure 5.28.

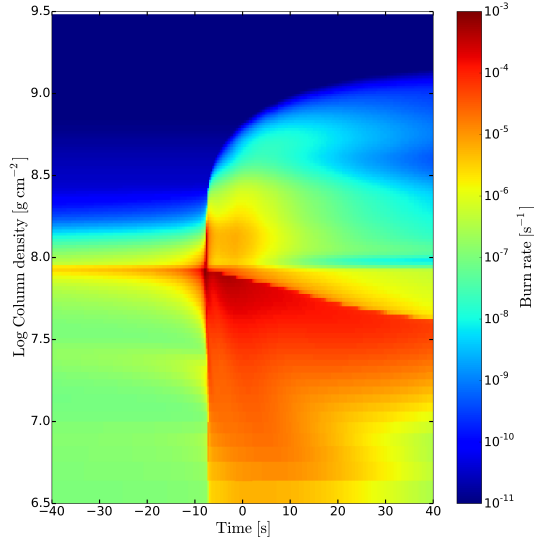
The time between two X-ray bursts is strongly linked to the ignition conditions such as temperature, density and composition of matter at the ignition depth. The burn rate is the fraction of nuclear energy release divided by the total available energy times the time step, and therefore describes the burning in a given zone in units of s^{-1} . One can use the burn rate for example to locate the ignition depth or to determine the strength of an X-ray burst. Comparing the burn rates of different accretion composition models, we found that the ratio of hydrogen to helium in the accreted matter defines the ignition column depth, see Figure 5.30. The larger the fraction of helium, the smaller the ignition column depth. In other words, low values of the hydrogen to helium ratio shifts the ignition point to lower temperatures and lower densities. However, models with low values of hydrogen to helium ratio have long recurrence times. At first sight, this seems to be a contrary behavior, since fresh fuel is accumulated faster at low depths, and thus one would expect a decrease in recurrence time with a decreasing ignition column depth. The explanation of increasing recurrence times with decreasing ignition column density can be found in the layer of fuel (see below). Just before the ignition of the burst, one can observe an increase in burn rate at the ignition depth. This account mainly for the hydrogen burning, triple-alpha process, hot CNO cycle and quiescence *rp*-process before the ignition. Especially the hydrogen-rich accretion composition model shows an increase in burn rate over a wider region around the ignition zone. Such a behavior indicates also that the temperature around the ignition zone is increased, enabling burning also in a stable manner before the explosive runaway. Comparing the hydrogen and helium mass fraction in function of the column density and time for the different accretion composition models (see above), we found significant differences especially in the ignition layers. If the amount of helium is raised compared to the hydrogen, one can observe an enlargement of the width of the burning layer during a X-ray burst. In fact, helium rich fuel generates an explosive runaway which depletes efficiently the hydrogen and helium over a large range. Hydrogen-rich bursts on the other side destroy the fuel only in a small surrounding of the ignition zone. This means that helium-rich bursts acquire a long recurrence time in order to fill up the previously burned layer of fuel, while hydrogen-rich bursts only need to regain a thin layer of fuel which can be accumulated during a shorter



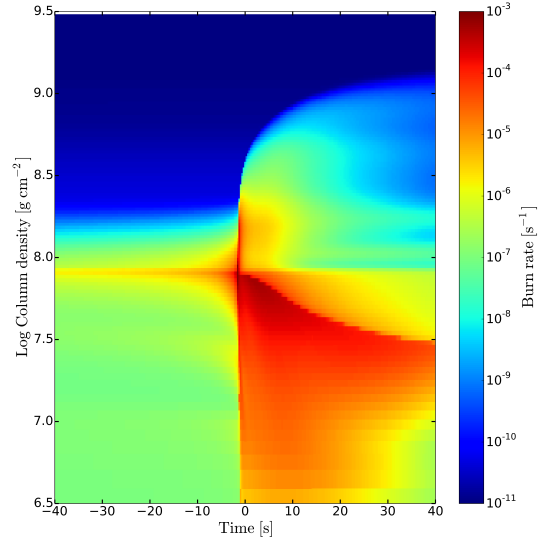
(a) Kippenhahn diagram of the hydrogen-rich accretion composition model.



(b) Kippenhahn diagram of the solar abundance accretion composition model



(c) Kippenhahn diagram of the helium-rich 1 accretion composition model.



(d) Kippenhahn diagram of the helium-rich 2 accretion composition model

Fig. 5.30 The burn rate in function of column density and time. For all models, we use no additional heating at the inner boundary. The time axis is chosen such that the burst peak luminosity takes place at $t = 0$ s. All models are listed in Table 5.4.

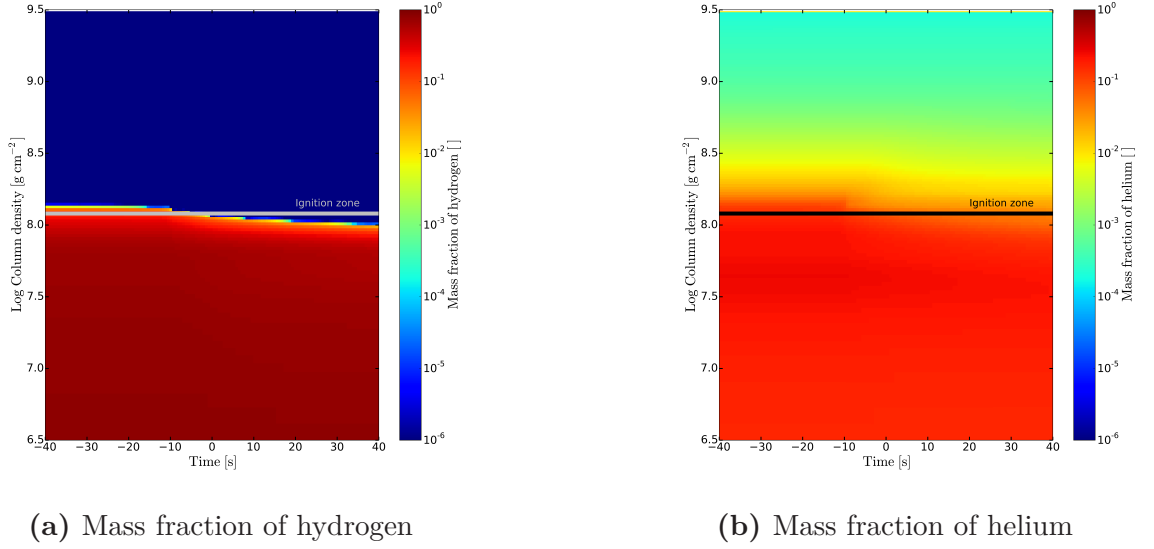


Fig. 5.31 The mass fraction of hydrogen and helium in function of time and column density for the model with hydrogen-rich accretion composition (see Table 5.4). The time axis is chosen such that the peak burst luminosity takes place at $t = 0$ s. The black respectively silver line indicates the ignition column density. For both models, we do not apply an additional heating ($Q_{\text{heat}} = 0$ MeV/nuc) in order to compare results with other setups.

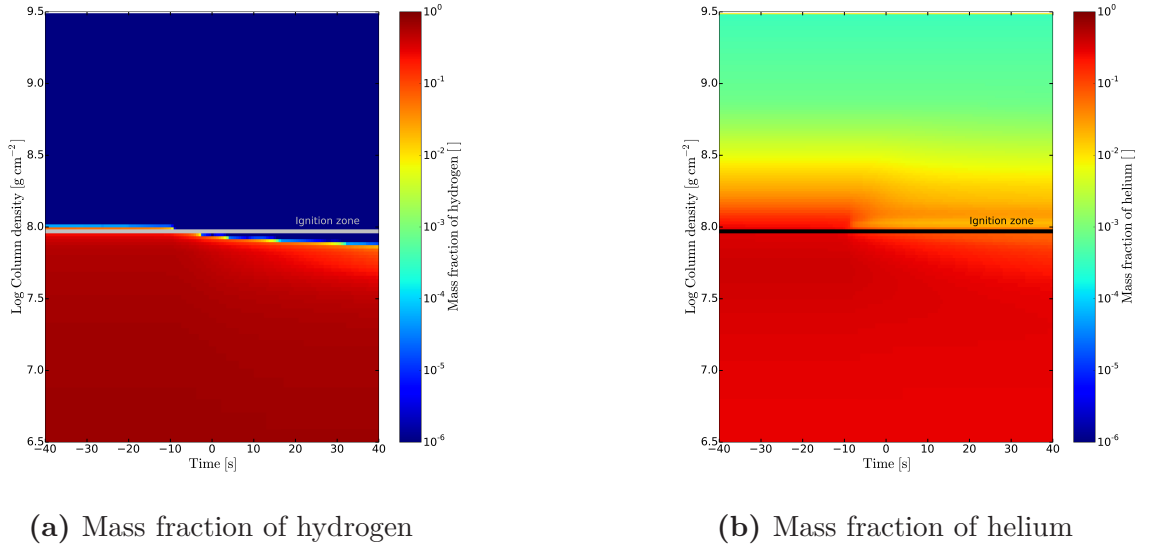
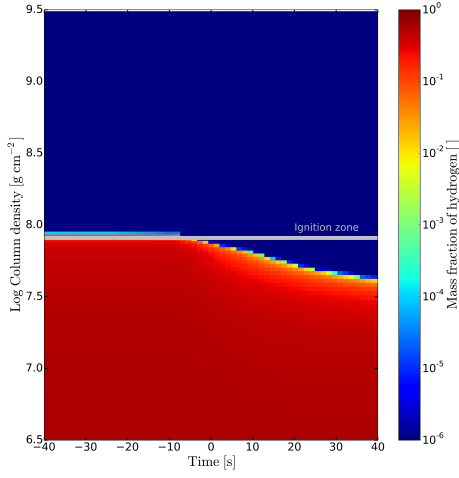
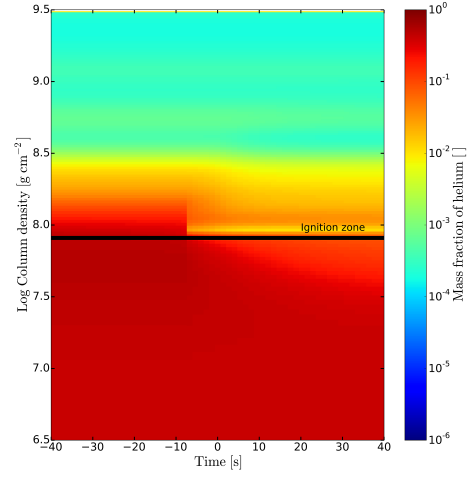


Fig. 5.32 The mass fraction of hydrogen and helium in function of time and column density for the model with solar accretion composition (see Table 5.4). The time axis is chosen such that the peak burst luminosity takes place at $t = 0$ s. The black respectively silver line indicates the ignition column density. For both models, we do not apply an additional heating ($Q_{\text{heat}} = 0$ MeV/nuc) in order to compare results with other setups.

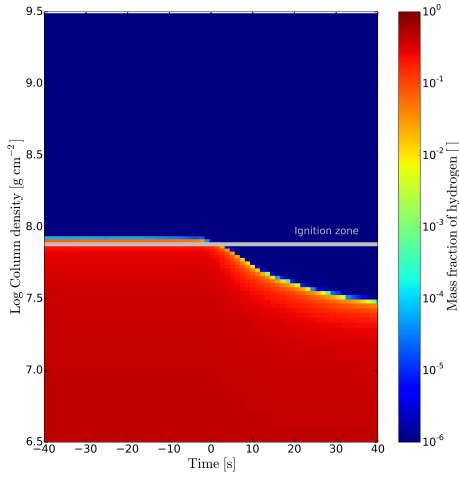


(a) Mass fraction of hydrogen

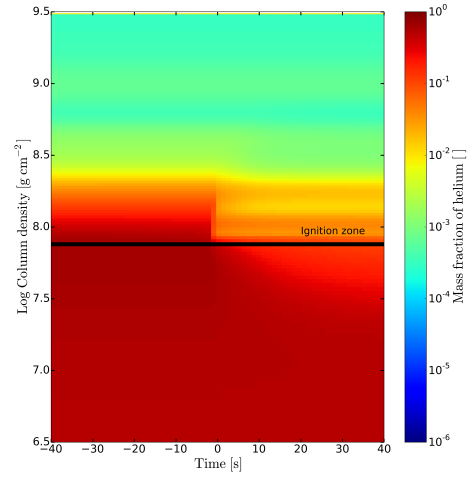


(b) Mass fraction of helium

Fig. 5.33 The mass fraction of hydrogen and helium in function of time and column density for the model with helium 1 accretion composition (see Table 5.4). The time axis is chosen such that the peak burst luminosity takes place at $t = 0$ s. The black respectively silver line indicates the ignition column density. For both models, we do not apply an additional heating ($Q_{\text{heat}} = 0$ MeV/nuc) in order to compare results with other setups.



(a) Mass fraction of hydrogen

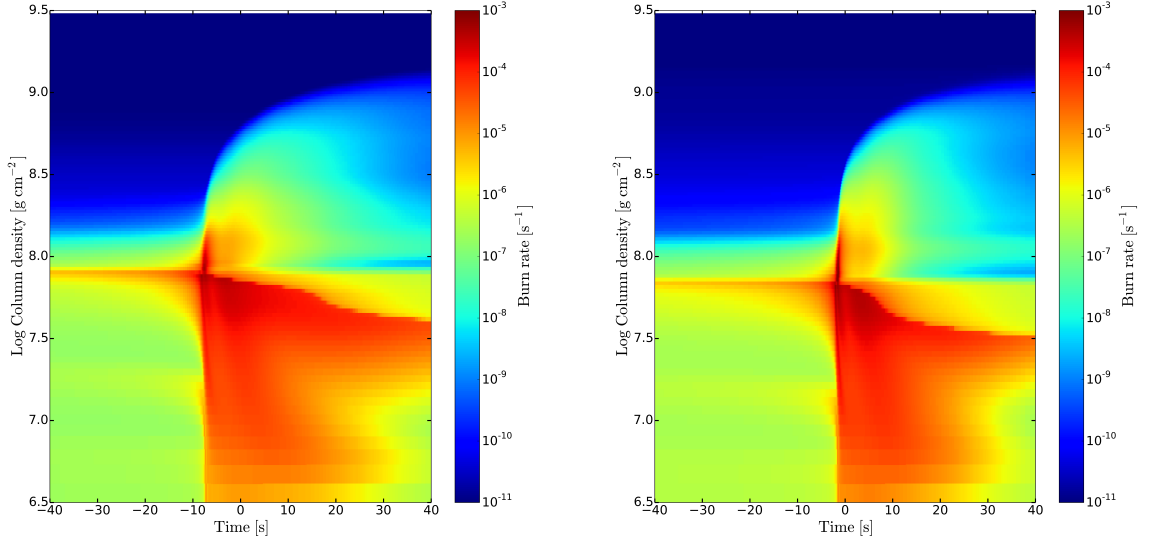


(b) Mass fraction of helium

Fig. 5.34 The mass fraction of hydrogen and helium in function of time and column density for the model with helium 2 accretion composition (see Table 5.4). The time axis is chosen such that the peak burst luminosity takes place at $t = 0$ s. The black respectively silver line indicates the ignition column density. For both models, we do not apply an additional heating ($Q_{\text{heat}} = 0$ MeV/nuc) in order to compare results with other setups.

time.

We found that the ratio of hydrogen to helium defines the width of a burning zone and



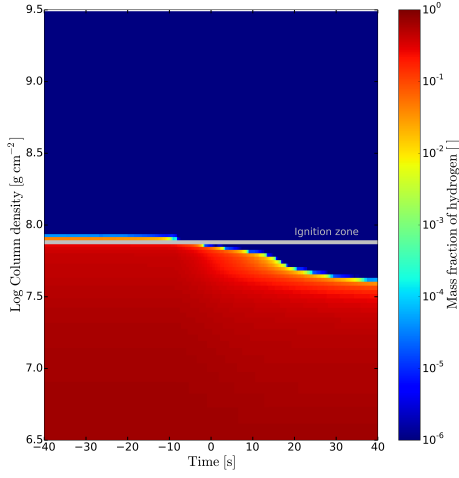
(a) Kippenhahn diagram of the heavy 1 accretion composition model, see Table 5.4.

(b) Kippenhahn diagram of the heavy 2 accretion composition model, see Table 5.4

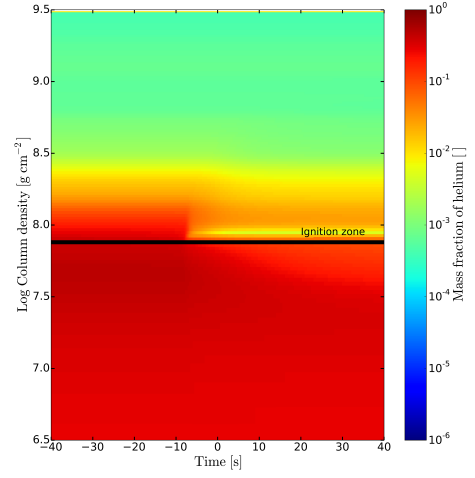
Fig. 5.35 The burn rate in function of column density and time for the heavy 1 and heavy 2 model (see Table 5.4). For both models, we do not apply an additional heating ($Q_{\text{heat}} = 0$ MeV/nuc) in order to compare results with other setups. The time axis is chosen such that the peak burst luminosity takes place at $t = 0$ s.

the recurrence time of X-ray bursts. However, previous study with the heavy 1 and heavy 2 accretion model did not largely influence the recurrence time. By the reason that the temperature profiles of the solar abundance, the heavy 1 and heavy 2 accretion models do not differ considerably, ignition column density and the composition at the ignition layer should be quite similar. Comparing the ignition depth of models with changes in the ratio of hydrogen/helium to heavier isotopes, we found a slight shift towards lower column densities with decreasing amount of helium and hydrogen. This result is in agreement with the variations we found in the recurrence times at zero heating (Figure 5.28). Therefore, the burning layer should be of approximately same size (not influencing the recurrence time to a large extend) for all the models with variations of accretion composition with constant ratio of hydrogen to helium.

Indeed, a comparison of Figure 5.36 and Figure 5.37 shows that the burning layers is of similar size. However, we found that the hydrogen as well as the helium is burned on a faster time scale with models of a larger fraction of heavier isotopes in the accre-

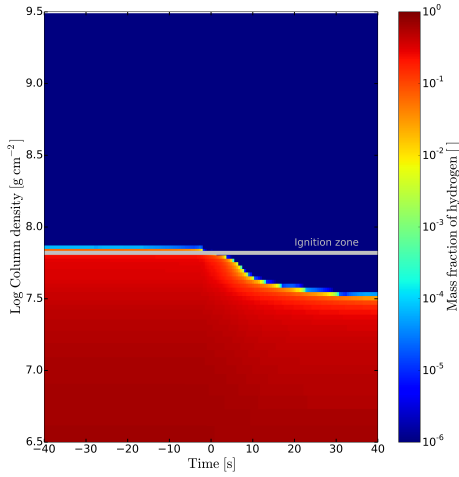


(a) Mass fraction of hydrogen

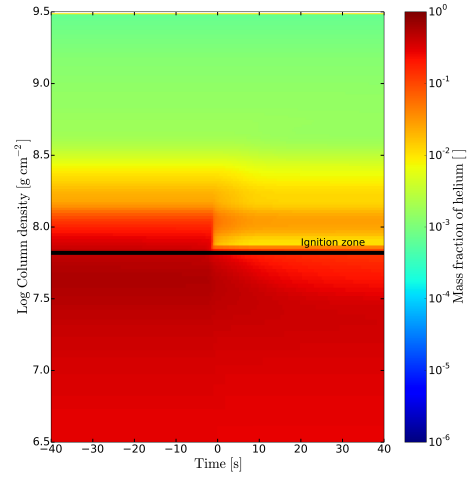


(b) Mass fraction of helium

Fig. 5.36 The mass fraction of hydrogen and helium in function of time and column density for the model with heavy 1 accretion composition (see Table 5.4). The time axis is chosen such that the peak burst luminosity takes place at $t = 0$ s. The black respectively silver line indicates the ignition column density. For both models, we do not apply an additional heating ($Q_{heat} = 0$ MeV/nuc) in order to compare results with other setups.



(a) Mass fraction of hydrogen



(b) Mass fraction of helium

Fig. 5.37 The mass fraction of hydrogen and helium in function of time and column density for the model with heavy 2 accretion composition (see Table 5.4). The time axis is chosen such that the peak burst luminosity takes place at $t = 0$ s. The black respectively silver line indicates the ignition column density. For both models, we do not apply an additional heating ($Q_{heat} = 0$ MeV/nuc) in order to compare results with other setups.

tion matter. That means that the accretion of heavier isotopes influence the resulting burst luminosities.

The burst luminosity is a useful feature to compare observed burst in low mass binary

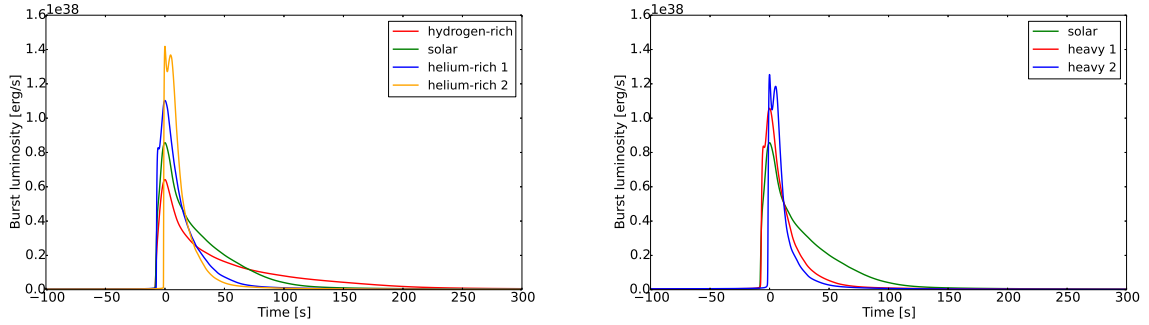


Fig. 5.38 The burst luminosities in function of the time since burst peak for different accretion composition models. The heating at the inner boundary is set to zero.

systems with simulations of X-ray bursts. While each burst is somehow unique, one can still make out some general properties of the X-ray burst light curve. An important feature is especially the occurrence of a double peak (Fisker et al., 2004) or the rarely appearance of triple peaks (Zhang et al., 2009). Our simulations indicate that not only helium-rich accretion compositions provide a double peak but also accretion of matter with heavier isotopes lead to double peak features. Such double peaks are thought to appear in helium bursts.

Model	$y_{ign} [g \text{ cm}^{-2}]$	$t_{fuel} [h]$	$t_{rec} [h]$	$X_H []$	$X_{He} []$
Hydrogen-rich	$1.2 \cdot 10^8$	5.27	3.51	0.102	0.117
Solar abundances	$9.3 \cdot 10^7$	4.08	4.39	0.039	0.196
Helium-rich 1	$8.1 \cdot 10^7$	3.56	4.54	0.111	0.304
Helium-rich 2	$7.6 \cdot 10^7$	3.34	5.05	0.084	0.366
Heavy 1	$7.6 \cdot 10^7$	3.34	3.91	0.076	0.289
Heavy 2	$6.6 \cdot 10^7$	2.90	3.68	0.030	0.408

Table 5.5 The ignition column density, accretion time of fuel, actually measured recurrence time, mass fraction hydrogen respectively helium at the ignition depth for different accretion composition models. The heating at the inner boundary is zero.

A study of the ignition conditions reveals that the model heavy 1 and heavy 2 are indeed generating a helium burst, see Table 5.5. A previous study of the computational domain revealed that a change in hydrogen/helium to heavier isotopes ratio does not

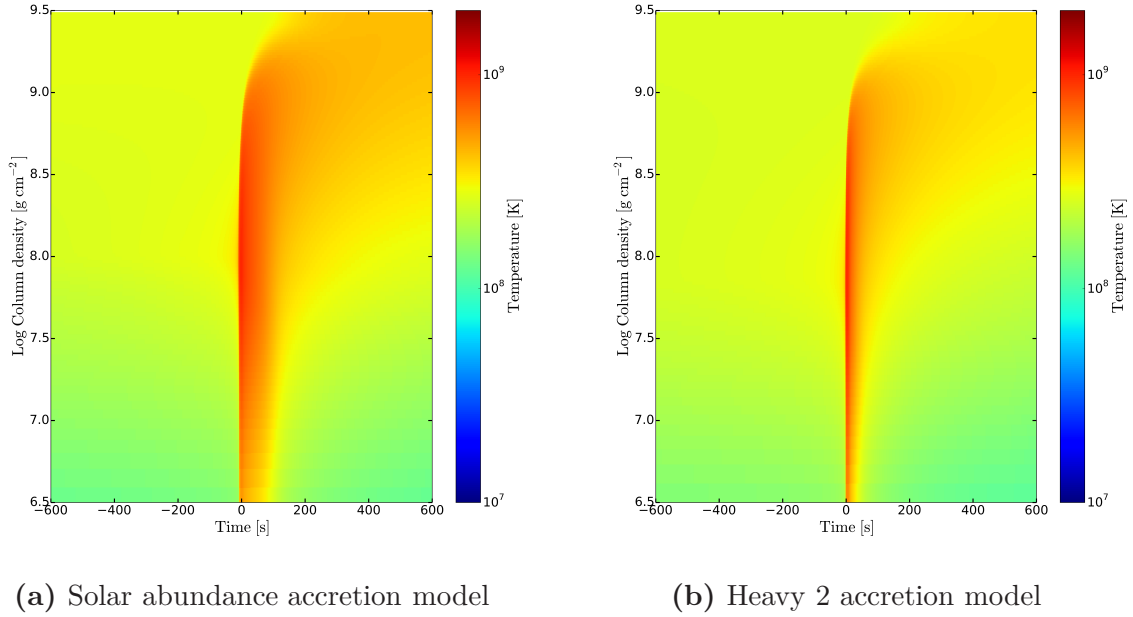


Fig. 5.39 The evolution of the temperature in the computational domain of the solar abundance and the heavy 2 accretion model. The additional luminosity at the inner boundary is set to zero and the time is scaled to the peak luminosity.

strongly affect the temperature before the ignition. Further, the reduction of helium and hydrogen in the accretion composition should rather lead to less amount of helium at the ignition depth. Since the recurrence time only varies in a range of approximately 1 h for the solar abundance, heavy 1 and heavy 2 model, the time between two burst seems not to be a plausible explanation for the helium-rich ignition environment of model heavy 1 and heavy 2. The solution is found before the ignition of an X-ray burst: Hydrogen is burning in a stable manner above the ignition density, generating additional helium in the layer of fuel. But why is stable burning of hydrogen active only in models with an increased amount of heavier isotopes in the accretion composition?

Comparing the temperature evolution of the solar abundance and heavy 2 model reveals part of the solution, see Figure 5.39. We found that the heavy 2 model cools down much faster after a burst in contrast to the solar abundance accretion model. In fact, the accretion composition has an important impact on the degeneracy of the electron gas. In a degenerate electron gas, the number of available low energy states is too small and many electrons are forced into high energy states. Therefore, the degeneracy depends not only on temperature and density but also on the number of

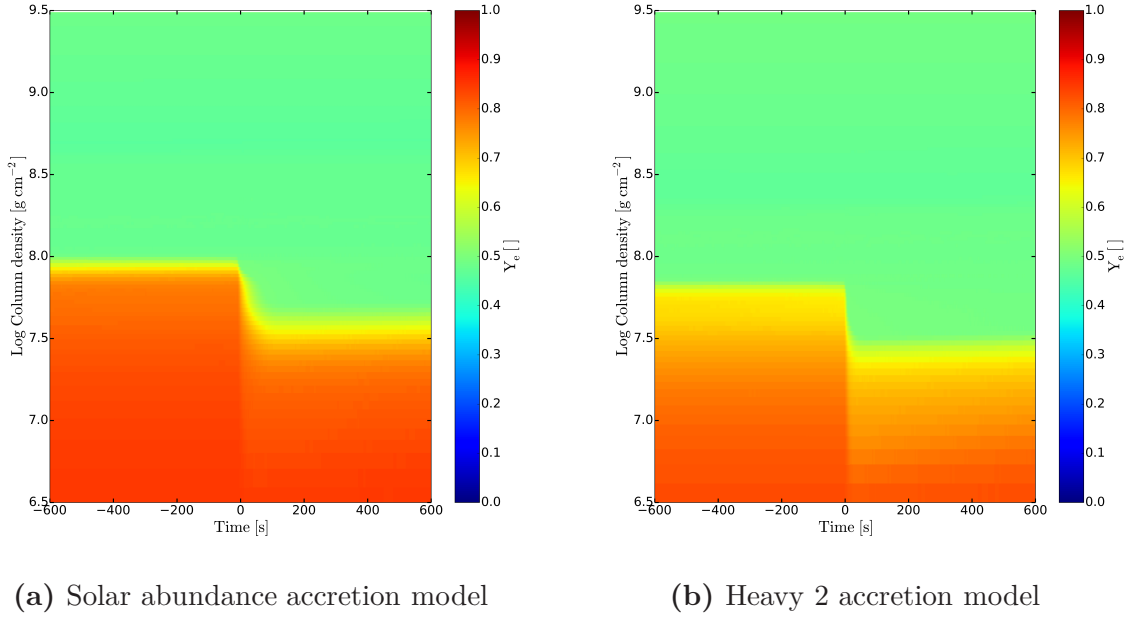


Fig. 5.40 The evolution of the electron abundance in the computational domain of the solar abundance and the heavy 2 accretion model. The additional luminosity at the inner boundary is set to zero and the time is scaled to the peak luminosity.

electron. Different accretion composition influence the electron density which changes the degeneracy of the electron gas at a given column density. To qualitatively measure the pressure due to the degeneracy of the electrons at a given temperature and density, one needs to calculate the electron abundance of a fully ionized gas, given by

$$Y_e = \sum_i \frac{X_i Z_i}{A_i}, \quad (5.7)$$

where X_i is the mass fraction, Z_i the proton number and A_i the mass number. A comparison of the electron abundance reveals that the degeneracy pressure with the accretion of a heavier isotope composition is less strong at the outer layers than with the accretion of solar abundance composition (see Figure 5.40). While the nuclear burning is stable in non degenerate regimes, it is highly explosive in degenerate conditions. Therefore, stable burning is much more prominent in the model heavy 1 and heavy 2 since conditions are less degenerate in comparison with the solar abundance model.

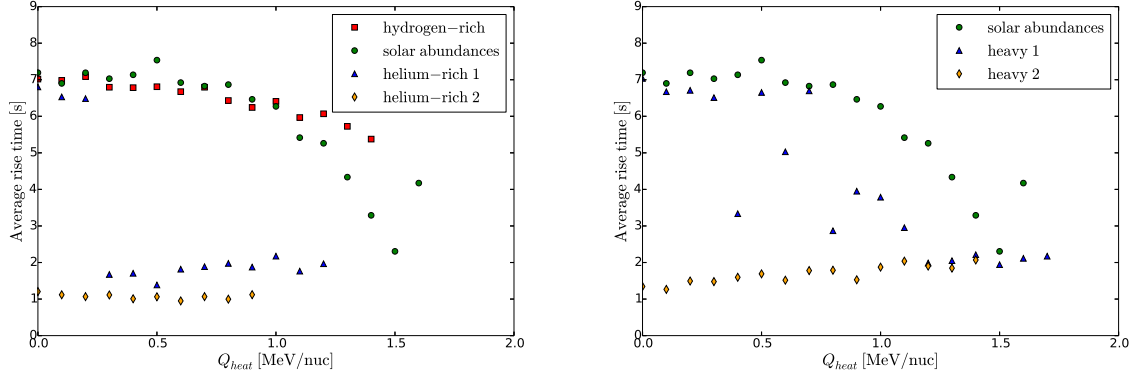
Whether burning is stable or unstable depends on the temperature dependence of the energy generation rate and the cooling rate (Keek et al., 2014). Comparing the accre-

tion time of fuel with the actually measured recurrence time in Table 5.5, we conclude that unstable burning is triggered less easily in the model heavy 1 and heavy 2 in comparison to the solar abundance model. Indeed, the difference between accretion time of fuel and recurrence time is 18 minutes in the case of solar abundance accretion and 47 minutes in the case of the heavy 2 model. Since the difference in accretion time and recurrence time is increasing with decreasing mass fraction of hydrogen in the constant sum of hydrogen and helium mass fraction (from the hydrogen-rich model to the helium-rich 2 model), we account the ignition problem to the lack of hydrogen in the layer of fuel. Helium bursts have shown to burn the fuel in a wide range, while weak hydrogen bursts are not able to destroy fully the helium close to the ignition zone. Therefore, helium bursts acquire to fill up the layers with fresh fuel even far below the ignition depth, thus resulting in an enlargement of the recurrence time.

Even though the degeneracy pressure is less prominent at given conditions in the outer layers of a heavy 1 and heavy 2 model, helium burst show significant higher burst luminosities than mixed hydrogen/helium bursts, see Figure 5.38. In addition, helium bursts need a larger fraction of fuel than hydrogen or mixed hydrogen/helium bursts. Indeed, thermally unstable hydrogen burning ignites helium as well and produces a mixed hydrogen/helium burst (Cooper and Narayan, 2007). However, with hydrogen-rich accretion compositions unstable hydrogen burning may not ignite helium and thus triggers only a weak hydrogen burst, see Figure 5.31. On the other side, if we apply a hydrogen-deficient accretion composition, the lack of heating due to the missing stable burning of hydrogen makes it more difficult to ignite a burst. This means that hydrogen-deficient bursts are triggered in an environment with plenty of fuel, thus resulting in a increase in burst luminosity.

Most observed X-ray bursts are though to be mixed hydrogen and helium bursts (Cornelisse et al., 2003; Galloway et al., 2008b; van Paradijs and Lewin, 1988), disfavoring the models helium-rich 2 or heavy 2. Nevertheless, observations of pure helium bursts found in for example Galloway and Cumming (2006) demonstrate that one can not simply disregard the models with ignition in a helium-rich environment. But we can conclude that in the current setup, a sufficient amount of hydrogen is required to reproduce typical mixed hydrogen/helium bursts.

The properties of an observed burst can not only be described by the maximal burst luminosity and its double peak features, but also by the rise and decay time. As described in the previous section, typical rise times are in the range of 1 – 10 s and e -folding times are of the order of 10 s (see Figure 5.23). We compute the rise time of



(a) Different mass fraction ratios of hydrogen to helium

(b) Different mass fraction ratios of hydrogen/helium to heavier isotopes

Fig. 5.41 The average rise time in function of crustal heating for different accretion compositions.

our simulated bursts follows:

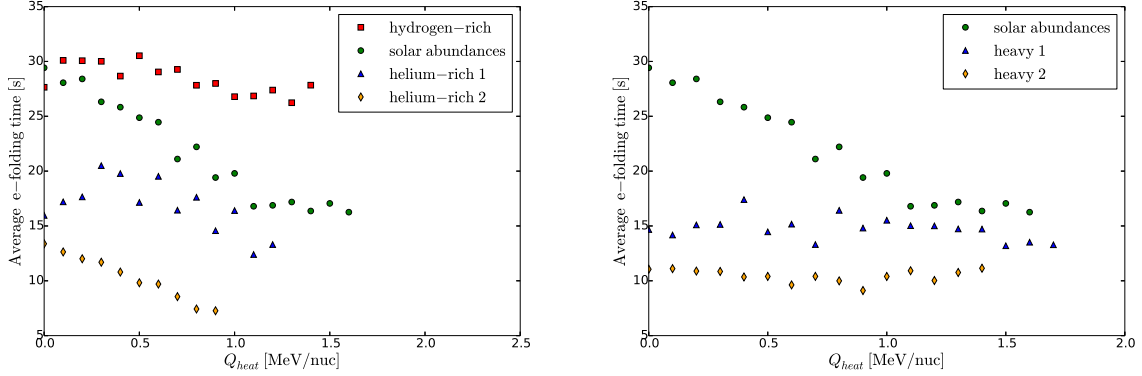
$$t_{rise} = t_{L=L_{peak}} - t_{L=2 \cdot L_{min}}, \quad (5.8)$$

where L_{peak} is the burst peak luminosity, L_{min} the minimal burst luminosity between two bursts and t the time as observed from infinity. The decay time as measured from infinity is given as the e -folding time

$$t_{decay} = t_{\ln(L_{peak}/L)=1} - t_{L=L_{peak}}. \quad (5.9)$$

Figure 5.41 shows the rise time of different accretion composition models. You should not that the double peak feature influences the calculation of the rise as well as the decay time. Depending whether the first or second peak is responsible for the maximal burst luminosity, the rise times of the helium-rich 1 and the heavy 1 model show some jumps. Therefore, a comparison of rise time makes only sense if we compare the rise times in function of the second peak which might not be the maximal luminosity. As a result, we found that the change in the accretion composition is not affecting the rise time at lower crust heating. All computed burst rise times are located in the range of typical observed rise times. Very short rise times are achieved with models which show the ignition of a helium burst with a maximal burst luminosity at the first peak.

In Figure 5.42, we plotted the e -folding time in function of the heating at the inner boundary. A comparison reveals that the e -folding time is depending on the mass



(a) Different mass fraction ratios of hydrogen to helium

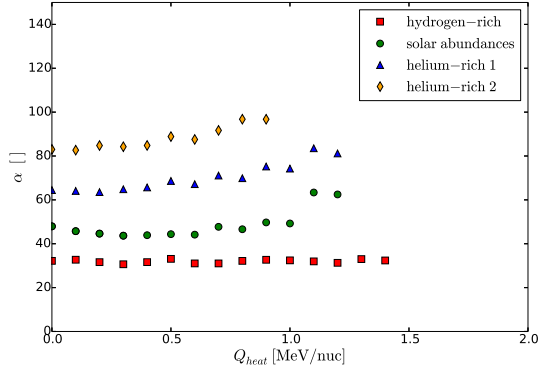
(b) Different mass fraction ratios of hydrogen/helium to heavier isotopes

Fig. 5.42 The average e -folding time in function of crustal heating for different accretion compositions.

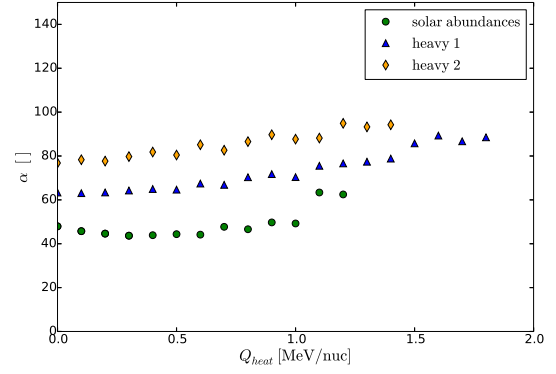
fraction of hydrogen in the accretion composition. The more hydrogen is accreted, the longer the e -folding time. In fact, the property of a reduction in the e -folding with decreasing amount of hydrogen is mainly linked to the ignition column depth (see Table 5.5). At a high value of the column depth, the density is large and thus, cooling is less efficient.

Comparing our simulations with typical observed e -folding decay times, we found that one should rather favor models with less hydrogen in the accretion composition. Using the solar abundance model, we would require a boundary heating of 1 MeV/nuc to achieve typical observed e -folding decay times. By the reason that e -folding decay times around 30 s are only rarely observed, solar abundance models with low crustal heating as well as the whole hydrogen-rich model do not reproduce observations.

Another important observable parameter is the ration α of persistent fluence to burst fluence. While typical X-ray bursts have α values slightly above 40 (Galloway et al., 2008b; Keek et al., 2010), superburst sources indicate α values of the order of 10^3 (in Zand et al., 2004). The α values of the current setup with different accretion compositions is displayed in Figure 5.43. The lack of hydrogen in the accretion composition leads to an increase in the α parameter. On the other hand, heating at the inner boundary does not strongly influence the range of the α value. The burst fluence (Figure ??) in hydrogen-rich accretion compositions is increased due to the fact that the decay in burst luminosity is slowed down. Further, a short recurrence time in hydrogen-rich models leads to a reduced persistent fluence as there is not enough time

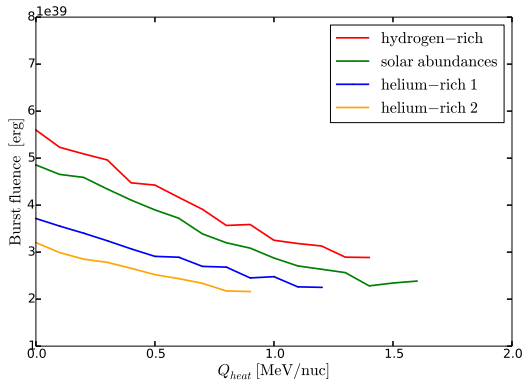


(a) Different mass fraction ratios of hydrogen to helium

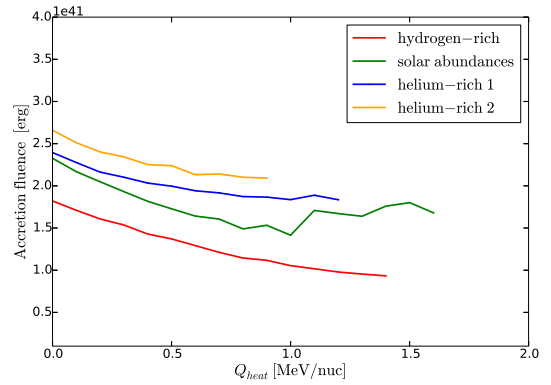


(b) Different mass fraction ratios of hydrogen/helium to heavier isotopes

Fig. 5.43 The α value in function of the crustal heating for different accretion compositions.



(a) The burst fluence of different accretion composition models.



(b) The accretion fluence of different accretion composition models.

to burn matter in a stable manner between the bursts.

By the reason that most X-ray bursts have α values slightly above 40, the solar abundance model seems to reproduce quite well the observations of the ratio of persistent fluence to burst fluence. Using the current setup, we could not reproduce α values well above 100. We account this problem to the simplifications of a 1D model which neglects the locally varying accretion rates and additional 3D effects.

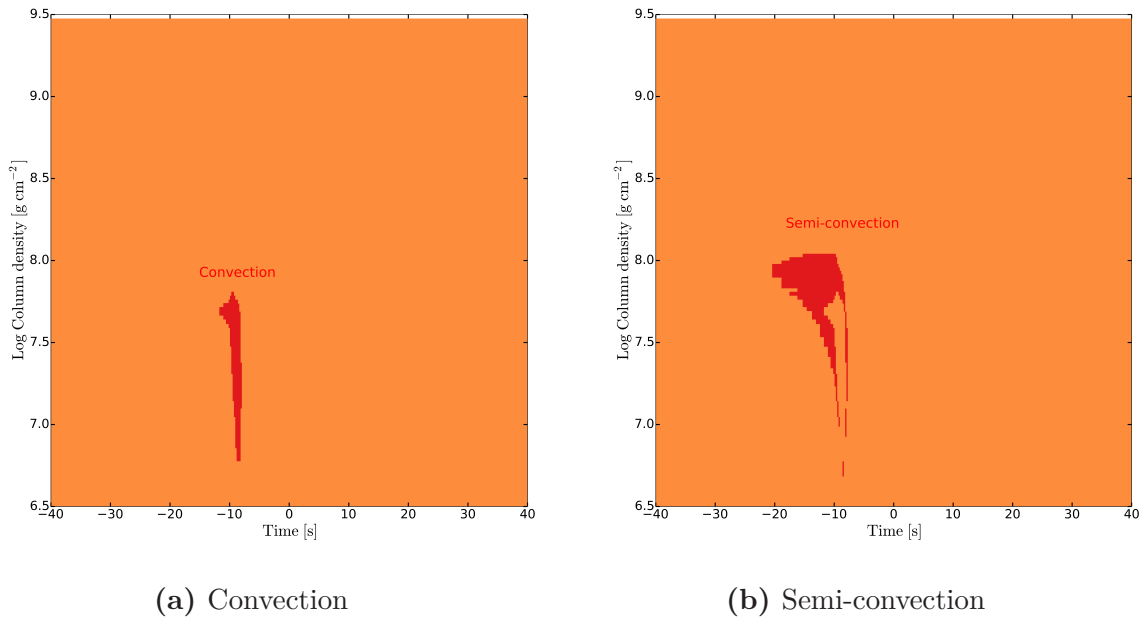


Fig. 5.45 The convective zone during a single bursts for the hydrogen-rich accretion composition. Additional heating is set to zero and the time axis coincides with the peak luminosity.

In Chapter 2, we discussed the weakness of the simplified convection approach. In order to verify whether convection or semi-convection plays a crucial role during our simulations, we identified the convective region during a single X-ray bursts, see Figure ?? to 5.50. We found that semi-convection and convection is prominent in simulations with hydrogen rich accretion compositions. Furthermore, increasing the mass fraction of heavier isotopes in the accretion composition reduces significantly the appearance of convection and semi-convection. We note here therefore that due to the drawback of a simplified convection approach, simulations with hydrogen-rich accretion compositions might introduce some errors. Fortunately, hydrogen-rich accretion compositions are rather unrealistic and are only studied in this chapter to understand the importance of hydrogen in the accreted matter.

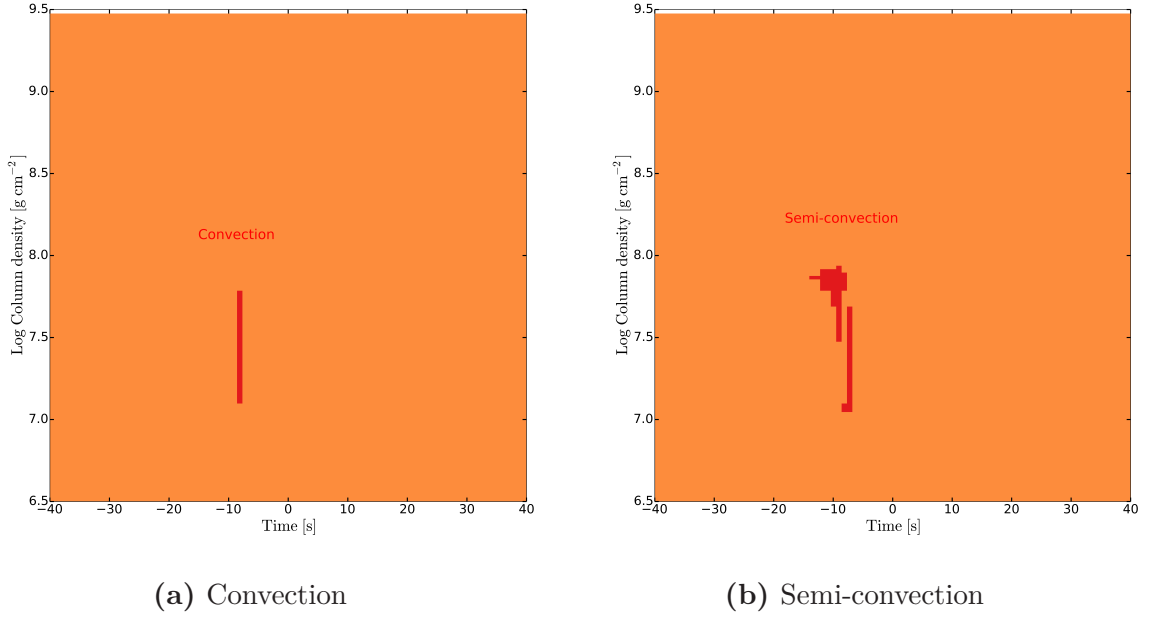


Fig. 5.46 The convective zone during a single bursts for the solar abundance accretion composition. Additional heating is set to zero and the time axis coincides with the peak luminosity.

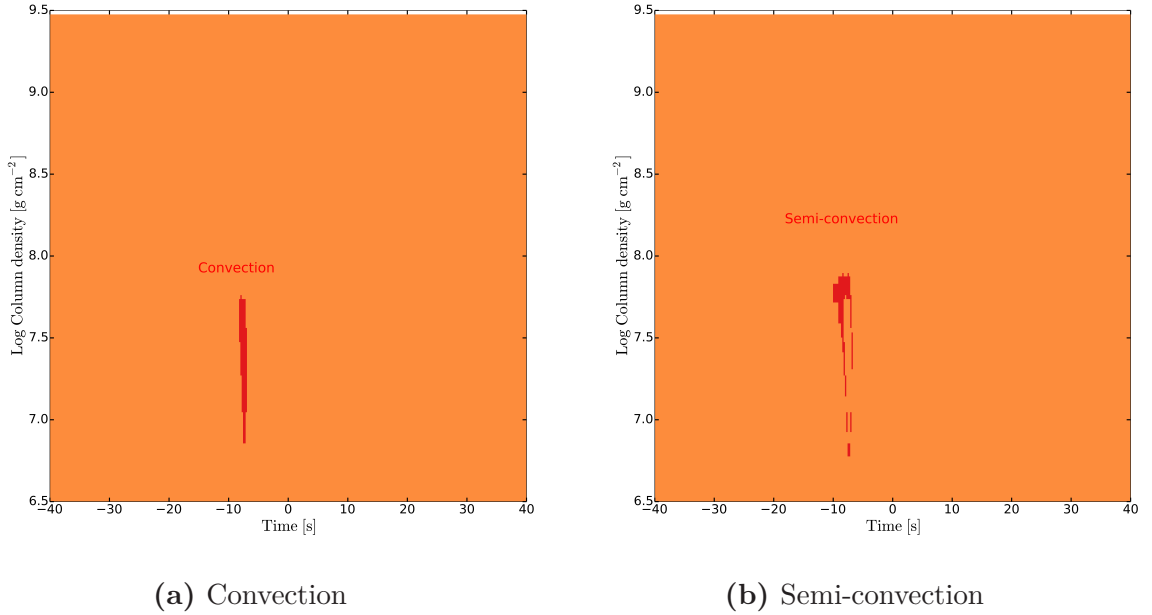


Fig. 5.47 The convective zone during a single bursts for the helium-rich 1 accretion composition. Additional heating is set to zero and the time axis coincides with the peak luminosity.

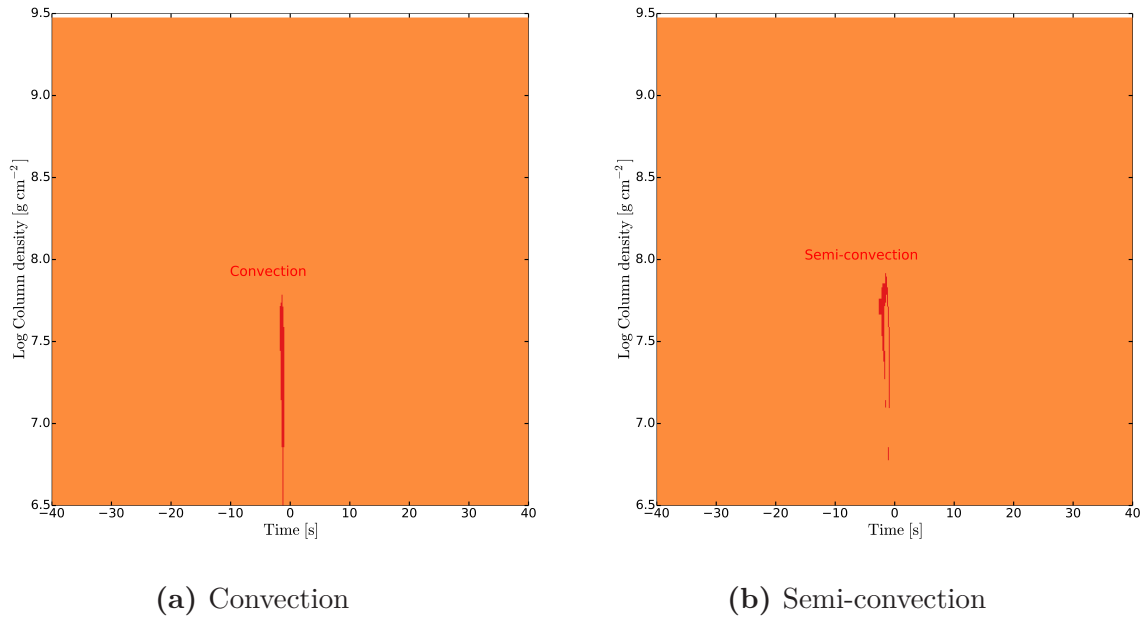


Fig. 5.48 The convective zone during a single bursts for the helium-rich accretion composition. Additional heating is set to zero and the time axis coincides with the peak luminosity.

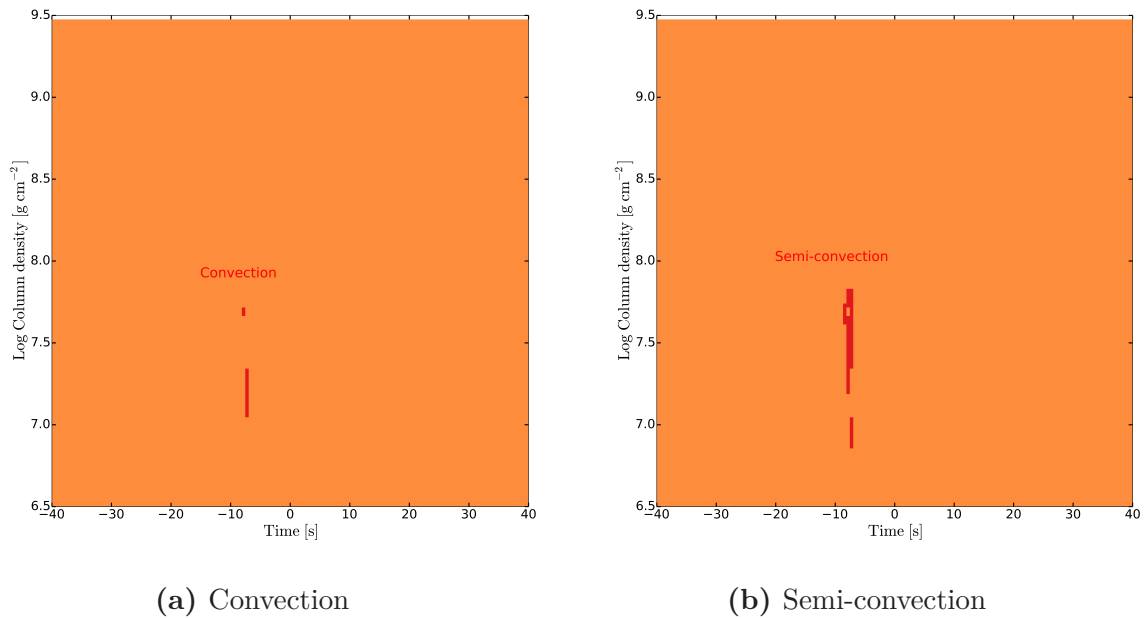


Fig. 5.49 The convective zone during a single bursts for the heavy 1 accretion composition. Additional heating is set to zero and the time axis coincides with the peak luminosity.

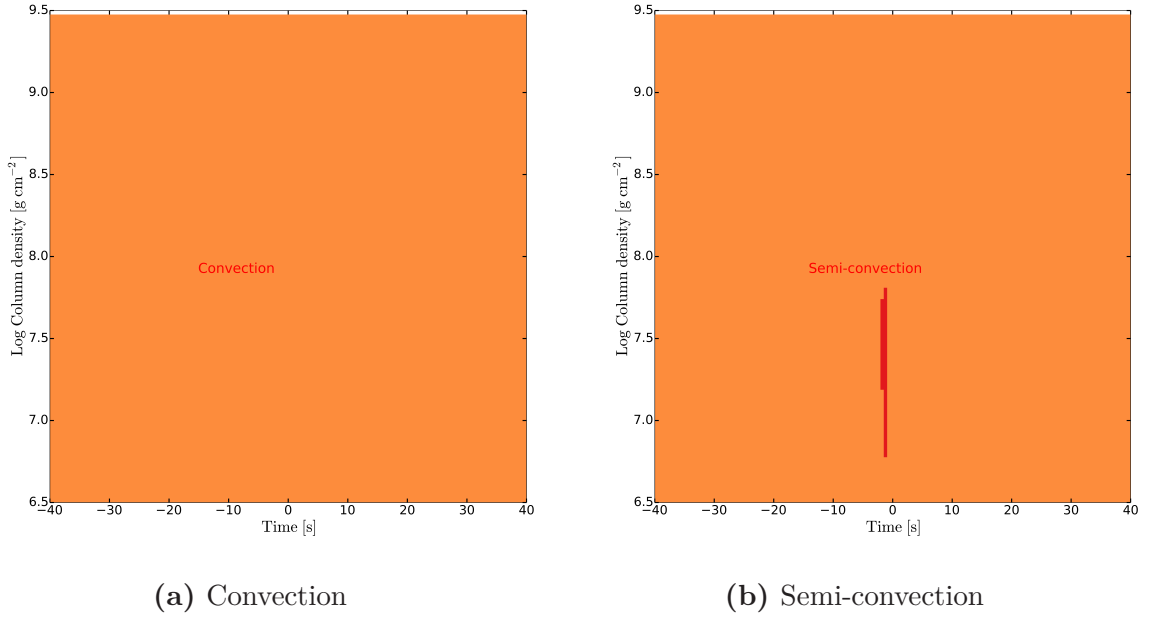


Fig. 5.50 The convective zone during a single bursts for the heavy 2 accretion composition. Additional heating is set to zero and the time axis coincides with the peak luminosity.

The heat flux in the computational domain plays a crucial role in the study of X-ray

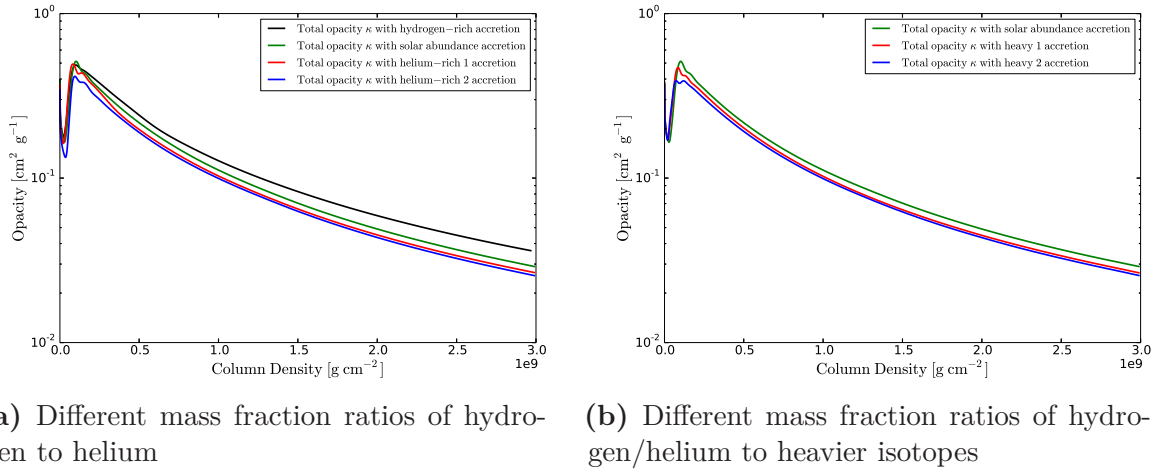
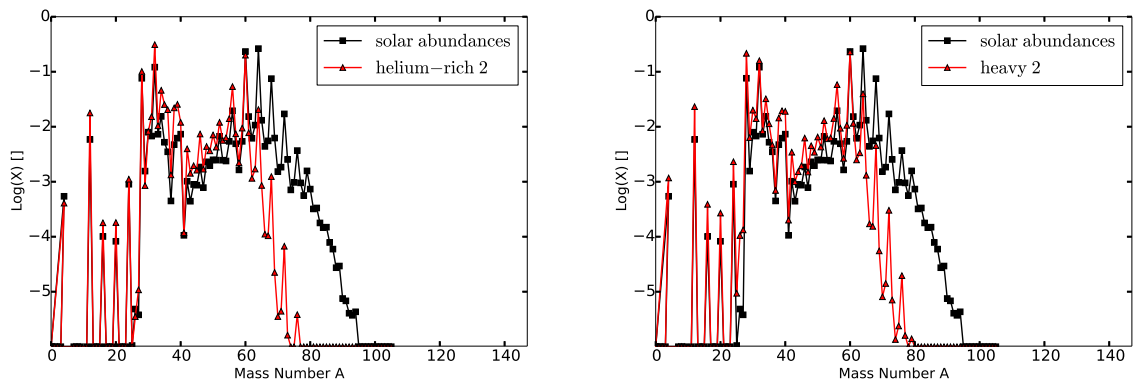


Fig. 5.51 The total opacity in function of the column density for different accretion compositions.

bursts as well as in the discussion of superbursts. The heat transport ability can be described by the opacity. It is therefore important to make out the basic changes in opacity as a result of different accretion compositions. In Figure 5.51 we display

the total opacity for different accretion composition models. The total opacity at a depth below the X-ray burst ignition zone shows a dependence of the mass fraction of hydrogen in the accretion composition. The more hydrogen-rich the accretion composition, the higher the total opacity below the X-ray burst ignition layer and thus, the more efficient the heat flux. However, we note here that the change in opacity is quite small and will not contribute meaningfully to the conditions at the superburst ignition depth.

Considering the possible ignition of a superburst, one needs to study carefully the



(a) The composition of the ashes with solar abundance and helium-rich 2 accretion composition.

(b) The composition of the ashes solar abundance and helium-rich 2 accretion composition

Fig. 5.52 The compositions of the ashes with different accretion compositions. The heating at the inner boundary has been set to zero for all models.

composition of the ashes. Figure 5.52 compares the composition of the ashes at a column density of $3 \cdot 10^9 \text{ g/cm}^2$. Hydrogen in the accretion composition shifts the ashes of X-ray bursts towards a heavier isotope composition. While one can not directly observe the composition of the ashes, a self-consistent ignition of a superburst within the observed recurrence time of a few years would manifest our model. Besides the required density and temperature at the ignition of a superburst, one needs a large amount of carbon which survives the cooling after an X-ray bursts as well as stable burning down to superburst column densities. The required amount of carbon in the fuel of superburst can also be achieved by stable burning of helium which would increase the mass fraction of carbon. In the following, we therefore analyze the mass fraction of carbon and helium in the ashes at a column density of $3 \cdot 10^9 \text{ g/cm}^2$.

The simulations of X-ray burst with different accretion compositions revealed that the lack of hydrogen in the accretion of matter generates an increasing amount of carbon

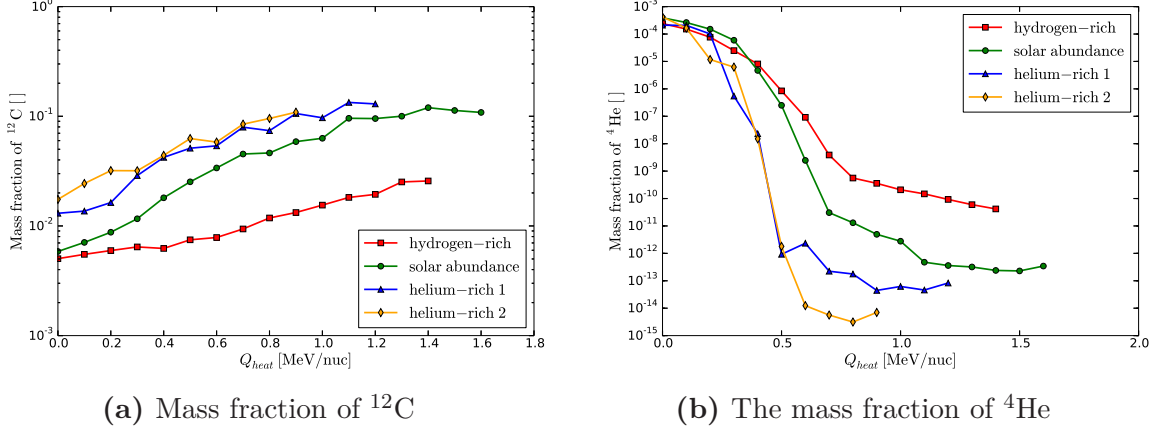


Fig. 5.53 The mass fraction of carbon and helium in the ashes at a column depth of $3 \cdot 10^9 \text{ g/cm}^2$ with different ratios of hydrogen to helium in the accretion compositions. Q_{heat} is the heating at the inner boundary which accounts for the heat flux generated at depths below the computational domain.

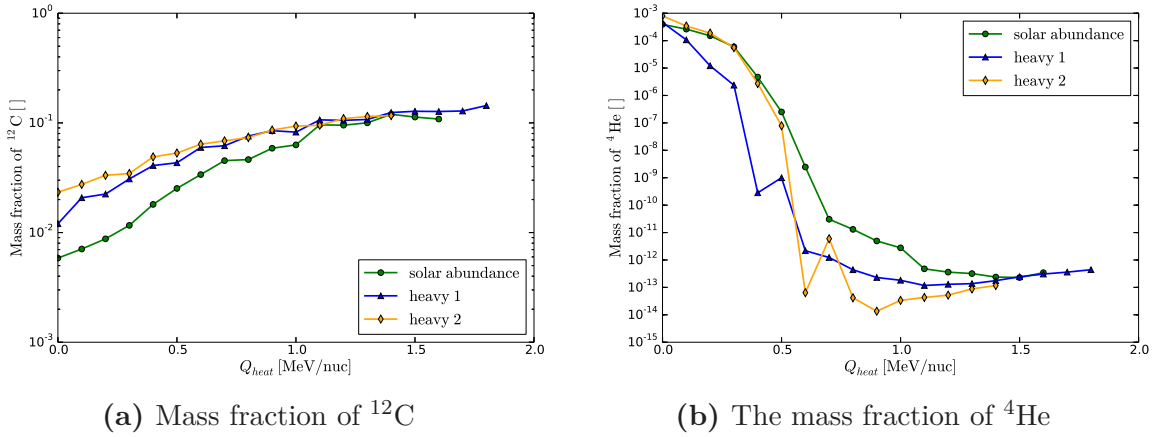


Fig. 5.54 The mass fraction of carbon and helium in the ashes at a column depth of $3 \cdot 10^9 \text{ g/cm}^2$ with different ratios of helium/hydrogen to heavier isotopes in the accretion compositions. Q_{heat} is the heating at the inner boundary which accounts for the heat flux generated at depths below the computational domain.

in the ashes, see Figure 5.53 and 5.54. Indeed, as indicated by the steep decay of the observable burst luminosity after the peak, a considerable amount of carbon is surviving the burning after the explosive runaway. Further, additional heating at the inner boundary of the computational domain helps to prevent the destruction of carbon. On the other side, helium does not survive down to column density of $3 \cdot 10^9$ g/cm² if one considers strong heating sources as found in for example Turlione et al. (2013). Since the mass fraction of helium in the ashes is at maximum of the order of 10^{-3} , one can conclude that stable burning of helium between the X-ray burst and the superburst ignition layer is not able to produce a significant amount of carbon using the current setup.

Surprisingly, the mass fraction of carbon seems to have an upper bound in our simulations with unstable burning. The table below lists the maximal mass fraction of carbon:

Model	Max mass fraction of carbon	Min Q_{heat} for $X_{12C} \geq 0.1$
hydrogen-rich	0.026	-
solar abundance	0.120	1.3 MeV/nuc
helium-rich 1	0.134	0.9 MeV/nuc
helium-rich 2	0.109	0.9 MeV/nuc
heavy 1	0.144	1.1 MeV/nuc
heavy 2	0.117	1.2 MeV/nuc

Table 5.6 Properties concerning the mass fraction of carbon in the ashes with different accretion compositions.

Assuming that one needs a mass fraction of carbon above 0.1 (Hashimoto et al., 2014) in the ashes of X-ray bursts and assuming further that carbon is not destroyed down to the ignition zone of superbursts, the applied crustal heating should be roughly 1 MeV/nuc. The maximal carbon mass fraction we could achieve with our accretion composition models is 0.14, see Table 5.6. Above that value, the simulations resulted in stable burning of fuel, no X-burst could be triggered. However, you should note that stable burning is able to produce a carbon mass fraction well above 0.2.

As a short summary of studying the composition of the accretion, we found that the recurrence time of X-ray bursts is depending sensitively on the ratio of hydrogen to helium in the accretion material. Increasing the mass fraction of heavier isotopes by a factor two or three of the solar abundance accretion does not largely affect the recurrence time. By the reason that the models heavy 1 and heavy 2 vary in hydrogen and

helium mass fraction below 5% in comparison with solar abundances, we conclude that in the current setup, the recurrence time depends mainly on the amount of hydrogen in the accreted layer. In general, all our simulated X-ray burst recurrence times agree with the values found in X-ray binary systems. The burst luminosity of our models show a evolution towards double peak bursts (helium bursts) with increasing mass fraction of helium in the accretion composition. Further, we found that heavier isotopes in the accretion composition enhance the appearance of a double peak feature. You should note that most observed X-ray bursts do not show an obvious double peak features.

All the accretion composition models discussed in the current section have average rise time in a range which agrees well with observations. The rise time is depending on the heating at the inner boundary: The more heat we apply, the shorter the average rise time. While the rise time is not changing significantly with the use of different accretion compositions, the average e -folding decay time is depending on the choice of the accretion composition. The lack of hydrogen in the accretion composition as well as heavier isotopes in the accreted matter reduce the e -folding decay time. Using the current setup, observations of e -folding decay times do rather disable all hydrogen-rich models as well as solar abundance models with low crustal heating at the inner boundary.

A very important parameter in the discussion of self-consistent superburst ignition is the mass fraction of ^{12}C in the ashes of X-ray bursts. As a result, we found that the lack of hydrogen as well as heavier isotopes in the accretion composition generates efficiently carbon in the ashes of X-ray bursts. In addition, heating at the inner boundary helps to prevent the destruction of carbon after peak luminosity.

After doing separate studies of the influence of different accretion rates and accretion compositions with our 1D code, we will combine both results in the next chapter to create an adequate superburst model.

Chapter 6

Simulations of Superbursts

To study the self-consistent ignition of superburst, one needs to adopt an initial model which provides the conditions down to a column density of the order of 10^{12}g/cm^2 . Keeping a high grid resolution at the X-ray burst ignition region as well as at superburst ignition depth is very challenging and requires a large number of grid cells. By the reason that the number of grid cells affects the speed of a simulation, we are forced to set the number of grid cells as low as possible. Indeed, we increase the number of grid cells from our X-ray burst model from 129 to 218 which should satisfyingly resolve the X-ray burst but also give us information about what is happening before and at the superburst ignition region. Previous superburst simulations have used a resolution of 150 grid cells (Fisker, private communication), thus the number of grid cells should suffice to study the ignition of a superburst.

Basically, to solve the puzzle of the appearance of superburst, we need not only to fulfill the requirements for the successful ignition, but also to realize the constrains of the observations. Unfortunately, studying the observations of X-ray bursts one finds indications of large variations in the accretion rate over a large time scale. Therefore, the constrains such as recurrence time, burst energetics or quiescence luminosities might vary over a time range between two superbursts. Calculations of Hashimoto et al. (2014) with a reduced network have shown that accretion rate might be a key essence in the study of superburst ignition.

A simulation of a model with one year of X-ray bursts requires a simulation wall clock time of one month on our server (Intel 2.7GHz, running with MPI and OpenMP on 8 nodes). One therefore has to choose the parameters carefully to make sure that the models might lead to a useful conclusion or possibly even the successful ignition of a superburst. It is therefore crucial to make the right choice of parameters which

might lead to the ignition of a superburst. The main goal of this study is to ignite self-consistently a superburst, while still maintaining the observational constraints.

The system of parameters which we have to set for the superburst simulations is very complex and but still crucial for this work. Since some of the parameters, such as accretion rate and crustal heating, might not be constant over time, we first try to model the general relations in the network of parameters. Understanding the sophisticated impact on the choice of parameters will help us to model a simulation which is in agreement with a future long term observation of X-ray bursts. Especially observations of superburster might be of great importance since the ignition of a superburst puts a further constrain on the choice of parameters in our 1D model.

In the following subsection, we will analyze how accretion rate, accretion composition and crustal heating can be combined to a realistic superburst model. In contrast to the chapter before, we try to combine the results found with different accretion rates and accretion compositions.

6.1 Increasing the computational domain

In order to simulate both X-ray bursts as well as the superburst ignition depth, we need to enlarge our computational domain towards the center of the neutron star. This means that the crustal heating used in the previous sections need to be shifted down to the superburst depth. In the previous chapter, we found that the temperature below the ignition zone of X-ray bursts is slightly increasing with increasing column depth. However, superbursts are thought to be triggered at a column depth of the order of $10^{12} \text{ g cm}^{-2}$ (Hashimoto et al., 2014; Keek and Heger, 2011; Zamfir et al., 2014) which means that one has to shift the crustal heating as follows:

$$Q_{heat}^{SB} = Q_{heat}^{X-ray} + \Delta Q_{heat}, \quad (6.1)$$

where Q_{heat}^{SB} is the additional heating at the inner boundary of a superburst model, Q_{heat}^{X-ray} is heating of the X-ray burst model (see previous Chapter) and ΔQ_{heat} accounts for the shift due to an enlargement of the computational domain. Assuming that the temperature continuously increasing down to the superburst ignition layer, ΔQ_{heat} has to be negative. Starting with an initial profile which consists of pure iron, the heat transport during the first ignition of a superburst is varying over time since the ashes of X-ray bursts are continuously replacing the initial iron. As a consequence,

one would require at least two superbursts to make sure that the simulation is not depending on the choice of the initial composition. Since the simulations of two successive superbursts would need approximately half a year of X-ray burst simulations (wallclock time), we focus on a single superburst while keeping in mind that the initial conditions are influencing the result.

As the initial composition is continuously shifted out of the computational domain due to the accretion of fresh matter, the heat transport is changing significantly over time. In order to find the appropriate value of ΔQ_{heat} , we did several fast test runs with an accretion rate of $2 \cdot 10^{17}$ g/s and an accretion rate of $1 \cdot 10^{17}$ g/s. Thereby, we used solar accretion composition and different crustal heating values. After running until equilibrium cycle, we compared the mass fraction of carbon at a column density of 10^9 g cm $^{-2}$ with the profile of the X-ray bursts simulations used in previous chapter. As an approximation, we found that $\Delta Q_{heat} = -0.5$ MeV/nuc with $\dot{M}_{acc} = 2 \cdot 10^{17}$ g/s and $\Delta Q_{heat} = -0.4$ MeV/nuc with $\dot{M}_{acc} = 10^{17}$ g/s. However, you should note that the test run was performed with a poor resolution profile and a quite large time step. In the following, we will set $\Delta Q_{heat} = -0.5$ MeV/nuc for all accretion rates and accretion compositions. However, as our superburst simulations showed strong turbulence and easily triggered stable burning during the first hundreds of X-ray bursts, we start with $\Delta Q_{heat}^{init} = -0.7$ MeV/nuc until bursting gets regular. Future work should be done on verifying the correct and precise value of ΔQ_{heat} for all models.

A superburst will generate a considerable heat flux towards the surface as well as towards the center of the neutron star. To handle this strong heat flux, one should change the inner boundary conditions to allow the transportation of heat towards the crust. In the current work, we will rather focus on the ignition of a superburst and leave therefore the adjustment of the inner boundary conditions for future work.

6.2 Models

The basic constrain to generate a superburst is the production and survival of carbon in the ashes of X-ray bursts. However, recurrence time, decay and rise time and the α value are further properties which allow a comparison with observations. In the following, we will focus on two different models:

Fast accretion model: $\dot{M}_{acc} = 2 \cdot 10^{17}$ g/s

Standard accretion model: $\dot{M}_{acc} = 10^{17}$ g/s

Slow accretion model: $\dot{M}_{acc} = 5 \cdot 10^{16}$ g/s

In a future work, we plan to cover further accretion rate regimes. Due to the lack of time, we are able to discuss only three accretion rates. In the following subsections, the three models are described in more details.

6.2.1 Fast accretion model

Models with an accretion rate $\gtrsim 1.5 \cdot 10^{17}$ g/s lead to discrepancies with observed properties, see Section 5.2.1. However, combining the results we found with accretion rate changes (Section 5.2.1) and different accretion compositions (Section 5.2.2), we can eliminate the problems. As illustrated in Table 6.1, additional helium in the

Property	Problem	Possible Solution
Recurrence time	too short	- accretion of more helium and less hydrogen
e -folding decay time	too long	- additional heating - accretion of more helium and less hydrogen - accretion of heavier isotopes
α value	too small	- strong heating - accretion of more helium and less hydrogen - accretion of heavier isotopes
Carbon in the ashes	not enough for superburst	- accretion of more helium and less hydrogen - accretion of heavier isotopes

Table 6.1 The problems of our high accretion rates models by comparing with observations and possible solutions. The table summarizes the result found in the previous chapter.

accretion composition would provide X-ray burst properties which are in agreement with observations. Heating as well as slightly more heavier isotopes in the accretion composition is supporting the production of carbon. That means that we can increase the accretion rate but need apply changes in the accretion compositions and crustal heating.

We define a new superburst model which uses an accretion rate of $1.5 \cdot 10^{17}$ g/s while still fulfilling basic observable properties. This fast accretion model is therefore combined with a crust heating of 1.2 MeV/nuc and an accretion composition consisting of 0.471 hydrogen, 0.510 helium and 0.019 remaining isotopes. In order to verify the observable properties of the fast accretion model, we took the X-ray burst model and simulated several hundreds of bursts. The resulting features are demonstrated in Table 6.2. The test X-ray burst model shows obvious irregular bursting behaviors, see Figure

Property	Value
Recurrence time	2.18 h
Average rise time	2.01 s
Average e -folding time	10.92 s
α value	74.43
Mass fraction of carbon in the ashes	0.12

Table 6.2 Features of the fast accretion superburst model. All the values lay in the range which one observed in typical accreting binary systems.

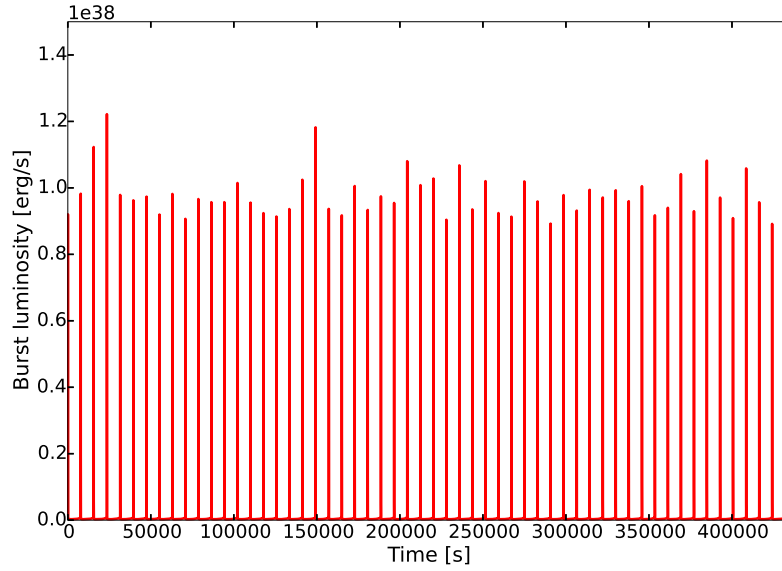


Fig. 6.1 The burst luminosity as seen from infinity of the test X-ray burst model with a fast accretion rate

6.1.

Remarkably, our test model does not show typical double peaked burst features

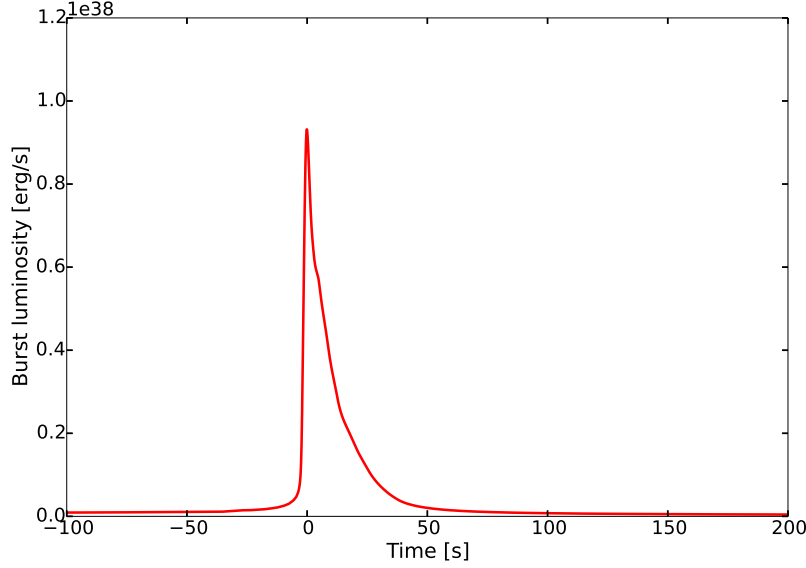


Fig. 6.2 A typical burst luminosity as seen from infinity of the test X-ray burst model with a fast accretion rate. The time axis coincides with the peak luminosity.

despite the helium rich accretion (Figure 6.2).

Concerning the superburst model, we need to shift the crustal heating at the inner boundary towards the center of the neutron star. As described above, $Q_{heat}^{X-ray} = 1.2$ MeV/nuc converts therefore to $Q_{heat}^{SB} = 0.7$ MeV/nuc.

6.2.2 Standard accretion model

The standard accretion rate model ($\dot{M}_{acc} = 10^{17}$ g/s with a solar accretion composition) does already fulfill the main observable properties. However, to generate enough fuel for the ignition of a superburst, we need to apply additional heating. In the following study, we will apply a boundary heating of $Q_{heat}^{X-ray} = 1.4$ MeV/nuc respectively $Q_{heat}^{SB} = 0.9$ MeV/nuc which provides a carbon mass fraction of 0.12 in the ashes of X-ray bursts (see Chapter 5).

6.2.3 Slow accretion model

Models with a low accretion rate of $\dot{M}_{acc} = 5 \cdot 10^{16}$ g/s do indeed generate a large mass fraction of carbon at even lower boundary heating. However, the models with

low accretion rates lead to very large recurrence times. Increasing the recurrence time could be maintained by additional hydrogen in the accretion composition. As the additional amount of hydrogen in the layer of fuel would destroy the carbon during the burst, slow accretion models seem not to be able to reproduce observable properties of superbursters in the current setup.

6.3 Simulation of superbursts

A simulation of thousands of X-ray burst and the ignition of a single superburst requires a wall clock time of approximately 3 months on the server at the University of Basel in 2015 (8 nodes, 2.7 GHz). At the time point of the submission of this work, simulations of the superburst have not yet been finished and might be the task of a future PhD project.

Chapter 7

Summary and outlook

In this work, we have updated and optimized the former X-ray burst code of J. Fisker (2006) in order to obtain a powerful tool for the study of X-ray bursts and superbursts. The use of parallel programming reduced the simulation time very effectively, enabling us the study of the self-consistent ignition of a superburst within a reasonable time. Further, we did update the description of the opacity according to calculations of Potekhin and Yakovlev (2001). Including the fast PARDISO solver of Schenk et al. (2001) in the calculations reduced the simulation time considerably. Finally, we did some small transformations of input variables which enables a user-friendly handling of the code.

The simulation of bursts in the surface layers of accreting neutron stars require the use of a sufficiently large nuclear network. By the reason that small network sizes are computed faster, we tried to minimize the size of the network used in the current work. Previous work of J. Fisker in 2006 suggests that a 304 isotope network is suitable for the simulations of bursts. Since the reaction rates used in the current work have been updated, the validation of J. Fisker in 2006 holds no more. Therefore, we tested the different sizes of the nuclear network by simulating hundreds of X-ray bursts at different accretion rates and comparing the results. We found that besides a small increase of carbon mass fraction in the ashes of X-ray bursts and the missing of beta decay reactions toward the valley of stability, the reduced 304 isotope network reproduces the results of a full network quite well.

After checking the nuclear network, we discussed in Chapter 4 the processes which take place during and between X-ray bursts. Studying the reaction flow during an X-ray burst and the resulting composition, we could get a general understanding of the conditions which are important in analyzing the bursts at the surface layer of

accreting neutron stars. We note here that further investigations should be done on the uncertainties of the *rp*-process reaction rates. A change in the reaction rate of certain important processes might produce slightly different results. However, studying additionally the reaction rates of processes involved in X-ray bursts is beyond the scope of a 4-year PhD work. We therefore fully relied on the reaction rates found in REACLIB V2.0 which has been submitted by Cyburt et al. in 2012.

The main focus of this work has been put on recent observation of thermal relaxations of neutron stars which suggest that an extra heating source in the layers just beyond the superburst ignition zone is needed to reproduce the observed cooling correctly (Shternin et al., 2011; Turlione et al., 2013). Indeed, we found that an extra heating source might not only solve the problems concerning neutron star cooling, but also possibly solves the puzzle of superburst recurrence times and ignitions. The survival of carbon right after the explosive runaway of an X-ray burst is enhanced in models with strong crustal heating. In fact, we found that additional heating is able to generate X-ray burst ashes which provide a carbon mass fraction above 0.1 at an accretion rate of 10^{17} g/s. As simulations of Hashimoto et al. (2014) demonstrate, a mass fraction of carbon above 0.1 in the layer of superburst fuel should be sufficient to ignite self-consistently a superburst. Assuming that the carbon in the ashes of X-ray bursts is not destroyed until a superburst ignites, we found that while accreting matter with solar abundance a crustal heating above 1.0 MeV/nuc at the inner boundary of our computational domain would generate the required amount of carbon in the superburst fuel layer.

Calculations of Turlione et al. (2013) suggest that the heating source is located below the superburst ignition depth. Such a heating source should be of the order of several MeV per accreted nucleon to explain observations of thermal relaxations of neutron stars. The heating which enters our calculations might be only a fraction of the actual heating source since heat might be as well transported towards the center of the neutron star. Indeed, we found that the heating at the inner boundary of our computational domain should be below 1.7 MeV/nuc since above that value, burning takes place in a stable manner and the occurrence of X-ray bursts stops.

Property	Additional heating	Increase in accretion rate
Peak luminosity	Decreasing	Decreasing
Recurrence time of X-ray bursts	Decreasing	Decreasing
Rise time of X-ray bursts	Decreasing	Increasing
Decay time of X-ray bursts	Decreasing	Increasing
α -value	Constant for high accretion, increasing at low accretion	Decreasing
Mass fraction of ^{12}C in the ashes	Increasing	Decreasing
Mass fraction of ^4He in the ashes	Decreasing with a slight increase at high of heating	Increasing
Mass fraction of heavier ashes	Decreasing	Increasing
Ignition density	Decreasing	Increasing
Ignition temperature	Increasing	Increasing

Table 7.1 A short summary of how the accretion rate and the heating affects the X-ray burst properties. You should note that we ignored for simplicity reasons the measurements close to the point where stable burning occurs. At those conditions, the profile started to fluctuate and general conclusions are no more valid.

Property	Increasing ratio of helium to hydrogen	Increasing mass fraction of heavier isotopes
Peak luminosity	Increasing	Increasing
Recurrence time of X-ray bursts	Increasing	Slightly decreasing
Rise time of X-ray bursts	Almost no effect	Almost no effect
Decay time of X-ray bursts	Decreasing	Decreasing
α -value	Increasing	Increasing
Mass fraction of ^{12}C in the ashes	Increasing	Increasing with low heating, no change with strong heating
Mass fraction of ^4He in the ashes	Decreasing	Increasing with low heating, decreasing with strong heating
Mass fraction of heavier ashes	Decreasing	Decreasing
Ignition density	Decreasing	Decreasing
Ignition temperature	Decreasing	Decreasing

Table 7.2 A short summary of how the accretion composition affects the X-ray burst properties. You should note that we ignored for simplicity reasons the measurements close to the point where stable burning occurs. At those conditions, the profile started to fluctuate and general conclusions are no more valid.

During our simulations, crustal heating had a strong impact on observable properties such as X-ray burst recurrence time, peak luminosity and ratio between burst and accretion fluence. In order to model a sequence of X-ray bursts which fulfills general observable X-ray burst properties, we studied different accretion rate and accretion composition setups. Running the simulations for hundreds of X-ray burst, we could extract general tendencies of X-ray burst properties with varying accretion rates, accretion composition and crustal heating. Table 7.2 shows a general overview of the results we found in Chapter 5. The fact that we make use of a one-dimensional description of the X-ray bursts limits us to rather general and averaged features of X-ray bursts since a detailed reproduction of observed X-ray burst light curves should rather be done with a realistic three-dimensional simulation. We found that heating, a low accretion rate as well as the lack of hydrogen in the accretion composition helps to produce carbon-rich X-ray burst ashes. As an interesting discovery, we found that the mass fraction of carbon in the ashes of X-ray bursts is somehow limited to a value slightly below 0.15. Above that value, burning was proceeding in a stable manner, the ignition of X-ray bursts was ceased.

In general, in order to simulate the self-consistent ignition of a superburst within the observed recurrence time of a few years, the ashes of X-ray bursts should be either carbon- or helium-rich. Therefore, strong heating at the inner boundary of the computational domain, accretion of insufficient hydrogen and lower accretion rates provide useful conditions for the analysis of superburst ignitions. However, understanding the influence of changes in the conditions such as accretion rate, heating and accretion composition helped us to generate an initial simulation setup which might be able to ignite self-consistently a superburst while still maintaining general observable X-ray burst features.

Increasing the number of grid points in the computational domain and accreting iron for a few years in the time frame of the neutron star, we expanded the X-ray burst model down to superburst ignition depth. Having discussed possible superburst setups and generated an adequate computational domain, we started running several superburst models. Since the proper simulation of thousands of X-ray bursts and the ignition of a single superburst requires the time of a few months, we have not been able to present the result in this current work by the reason that the simulations are still running.

7.0.1 Future projects

The main focus of this current simulations was put on the parameters of crustal heating, accretion rate and accretion composition. However, due to the very limited number of different models, we did not cover the whole range of possible conditions. In future, one should complete the study by running a large number of X-ray burst models in order to understand the link between conditions which influence the X-ray bursts. Having a detailed study of the ignition conditions would provide a powerful knowledge of how one could possibly trigger superbursts while still maintaining basic observable X-ray burst and superbursts features.

On the other side, more work should be done concerning the reaction rates and the size of the network. In the current work, we relied on the available reaction rates which determine also the size of the network. Possibly, the size of the network would not be sufficient to describe the ignition and reaction flows during a superburst. In addition, changes in the reaction rates might influence the important features of X-ray bursts (Fisker et al., 2006). Therefore, one should analyze and discuss the nuclear reaction in the computational domain more carefully.

Concerning the superburst ignition, one should run a bunch of different models to analyze whether applied conditions lead to the ignition of a superburst or not. An important obstacle one will encounter during the simulations of thousands of X-ray bursts will be the stable burning of carbon which would destroy the fuel of a possible superburst. Therefore, future superburst simulations should also focus on how accreted matter is behaving while compressed due to the accretion of fresh matter. Knowing which conditions lead to burning of X-ray burst ashes in a stable manner will put further constraints on the network of unknown parameters.

To simulate and analyze a single superburst properly, one has to adjust the inner boundary of our computational domain to allow transportation of heat towards the center of the neutron star. In the current work, we were rather interested in the self-consistent ignition of a superburst and left the detailed study of a superburst simulation to future projects.

The work of Hashimoto et al. (2014) has shown that variations in the accretion rate might be of great importance. Future work should therefore concentrate also on time dependent accretion rates. Additionally, the work of Horowitz et al. (2007) indicates that the missing carbon could also be provided by phase separations in the crust. Future superburst simulations might include an additional carbon source as a boundary condition.

References

- Amthor, A. M., Galaviz, D., Heger, A., Sakharuk, A., Schatz, H., and Smith, K. (2006). Sensitivity of Type I X-Ray Bursts to rp-Process Reaction Rates. page PoSNIC.
- Baiko, D. A. and Yakovlev, D. G. (1995). Thermal and Electric Conductivities of Coulomb Crystals in Neutron Stars and White Dwarfs. *Astron.Lett.*, 21:709.
- Bhattacharyya, S. (2010). Measurement of neutron star parameters: A review of methods for low-mass X-ray binaries. *Advances in Space Research*, 45(8):949–978.
- Cavecchi, Y., Watts, A. L., Levin, Y., and Braithwaite, J. (2014). Rotational effects in thermonuclear Type I Bursts: equatorial crossing and directionality of flame spreading.
- Chenevez, J., Brandt, S., Kuulkers, E., Alfonso-Garzon, J., Beckmann, V., Bird, T., Courvoisier, T., Del Santo, M., Domingo, A., Ebisawa, K., et al. (2011). First superbust observed by INTEGRAL, from SAX J1747. 0-2853. *The Astronomer’s Telegram*, 3183:1.
- Cooper, R. L. and Narayan, R. (2007). Hydrogen-Triggered Type I X-ray Bursts in a Two-Zone Model. *Astrophys.J.*, 661:468–476.
- Cornelisse, R., Heise, J., Kuulkers, E., Verbunt, F., and Zand, J. i. (2000). The longest thermonuclear X-ray burst ever observed?(A BeppoSAX Wide Field Camera observation of 4U 1735-44). *arXiv preprint astro-ph/0003454*.
- Cornelisse, R., in Zand, J. J. M. t., Verbunt, F., Kuulkers, E., Heise, J., den Hartog, P. R., Cocchi, M., Natalucci, L., Bazzano, A., and Ubertini, P. (2003). Six years of BeppoSAX Wide Field Cameras observations of nine galactic type-I X-ray bursters. *Astron.Astrophys.*, 405:1033–1042.
- Cornelisse, R., Verbunt, F., Zand, J. i., Kuulkers, E., Heise, J., Remillard, R., Cocchi, M., Natalucci, L., Bazzano, A., and Ubertini, P. (2002). BeppoSAX Wide Field Cameras observations of six type I X-ray bursters. *arXiv preprint astro-ph/0207135*.
- Cox, J. P. (1968). *Principles of stellar structure - Vol.1: Physical principles; Vol.2: Applications to stars*.
- Cumming, A. and Macbeth, J. (2004). The Thermal Evolution following a Superburst on an Accreting Neutron Star. page Astrophys.J.
- Cumming, A., Macbeth, J., in Zand, J. J. M. t., and Page, D. (2006). Long Type I X-ray Bursts and Neutron Star Interior Physics. *Astrophys.J.*, 646:429–451.

- Cybert, R. H., Amthor, A. M., Ferguson, R., Meisel, Z., Smith, K., Warren, S., Heger, A., Hoffman, R., Rauscher, T., Sakharuk, A., et al. (2010). The JINA REACLIB database: its recent updates and impact on type-I X-ray bursts. *The Astrophysical Journal Supplement Series*, 189(1):240.
- Fisker, J. L., Gorres, J., Wiescher, M., and Davids, B. (2006). The importance of $^{15}\text{O}(\text{a,g})^{19}\text{Ne}$ to X-ray bursts and superbursts. *Astrophys.J.*, 650:332–337.
- Fisker, J. L., Schatz, H., and Thielemann, F.-K. (2008). Explosive hydrogen burning during type I X-ray bursts. *The Astrophysical Journal Supplement Series*, 174(1):261.
- Fisker, J. L., Thielemann, F.-K., and Wiescher, M. (2004). The nuclear reaction waiting points: ^{22}Mg , ^{26}Si , ^{30}S , and ^{34}Ar and bolometrically double-peaked type I X-ray bursts. *The Astrophysical Journal Letters*, 608(1):L61.
- Fowler, W. A., Caughlan, G. R., and Zimmerman, B. A. (1967). Thermonuclear Reaction Rates. *Annu. Rev. Astron. Astrophys.*, 5:525–570.
- Fuller, G. M., Fowler, W. A., and Newman, M. J. (1980). Stellar weak-interaction rates for sd-shell nuclei. I - Nuclear matrix element systematics with application to Al-26 and selected nuclei of importance to the supernova problem. *Astrophys.J.Suppl.*, 42:447–473.
- Fynbo, H. O., Diget, C. A., Bergmann, U. C., Borge, M. J., Cederkäll, J., Dendooven, P., Fraile, L. M., Franchoo, S., Fedosseev, V. N., Fulton, B. R., et al. (2005). Revised rates for the stellar triple- α process from measurement of ^{12}C nuclear resonances. *Nature*, 433(7022):136–139.
- Galloway, D. and Cumming, A. (2006). Helium-rich thermonuclear bursts and the distance to the accretion-powered millisecond pulsar SAX J1808.4-3658. *Astrophys.J.*, 652:559–568.
- Galloway, D., Ozel, F., and Psaltis, D. (2008a). Biases for neutron-star mass, radius and distance measurements from Eddington-limited X-ray bursts.
- Galloway, D. K., Muno, M. P., Hartman, J. M., Psaltis, D., and Chakrabarty, D. (2008b). Thermonuclear (type-I) X-ray bursts observed by the Rossi X-ray Timing Explorer.
- Glen, G. and Sutherland, P. (1980). On the cooling of neutron stars. *The Astrophysical Journal*, 239:671–684.
- Gupta, S., Brown, E. F., Schatz, H., Moeller, P., and Kratz, K.-L. (2007). Heating in the Accreted Neutron Star Ocean: Implications for Superburst Ignition. *Astrophys.J.*, 662:1188–1197.
- Hōshi, R. (1980). Helium Flash Model for X-Ray Bursts. *Progress of Theoretical Physics*, 64:820–830.
- Hansen, C. and Van Horn, H. (1975). Steady-state nuclear fusion in accreting neutron-star envelopes. *The Astrophysical Journal*, 195:735–741.

- Hashimoto, M.-a., Kuromizu, R., Ono, M., Noda, T., and Fujimoto, M. Y. (2014). Numerical Experiments for Nuclear Flashes toward Superbursts in an Accreting Neutron Star. *Journal of Astrophysics*, 2014.
- Hix, W. R. and Thielemann, F. K. (1999). Computational Methods for Nucleosynthesis and Nuclear Energy Generation.
- Horowitz, C. J., Berry, D. K., and Brown, E. F. (2007). Phase separation in the crust of accreting neutron stars. *Phys.Rev.E*, 75:066101.
- in Zand, J. J. M. t., Cornelisse, R., and Cumming, A. (2004). Superbursts at near-Eddington mass accretion rates. *Astron.Astrophys.*, 426:257–265.
- in Zand, J. J. M. t., Kuulkers, E., Verbunt, F., Heise, J., and Cornelisse, R. (2003). A superburst from 4U 1254-690. *Astron.Astrophys.*, 411:L487–L492.
- In’t Zand, J., Kuulkers, E., Verbunt, F., Heise, J., and Cornelisse, R. (2003). A superburst from 4U 1254-69. *Astronomy and astrophysics*, 411(3):L487–L491.
- Keek, L., Cyburt, R., and Heger, A. (2014). Reaction Rate and Composition Dependence of the Stability of Thermonuclear Burning on Accreting Neutron Stars. *Astrophys.J.*, 787:101.
- Keek, L., Galloway, D. K., in Zand, J. J. M. t., and Heger, A. (2010). Multi-Instrument X-ray Observations of Thermonuclear Bursts with Short Recurrence Times.
- Keek, L. and Heger, A. (2011). Multi-Zone Models of Superbursts from Accreting Neutron Stars.
- Keek, L., Heger, A., and in Zand, J. J. M. t. (2012). Superburst Models for Neutron Stars with Hydrogen and Helium-Rich Atmospheres. page The Astrophysical Journal.
- Keek, L. and in Zand, J. J. M. t. (2008). On burning regimes and long duration X-ray bursts. *PoS Integral*, 08:032.
- Kuulkers, E. (2002). A superburst from GX 3+ 1. *Astronomy and Astrophysics*, 383:L5–L8.
- Kuulkers, E. (2005). Probable superbursts in 4U 0614+ 091 and 4U 1608-522. *The Astronomer’s Telegram*, 483:1.
- Kuulkers, E., den Hartog, P. i., Zand, J. i., Verbunt, F., Harris, W., and Cocchi, M. (2002). Photospheric radius expansion x-ray bursts as standard candles. *arXiv preprint astro-ph/0212028*.
- Kuulkers, E., Zand, J., Atteia, J.-L., Levine, A., Brandt, S., Smith, D., Linares, M., Falanga, M., Sánchez-Fernández, C., Markwardt, C., et al. (2009). What ignites on the neutron star of 4U 0614+ 091? *arXiv preprint arXiv:0909.3391*.
- Langanke, K., Martinez-Pinedo, G., and Sampaio, J. M. (2001). Neutrino spectra from stellar electron capture. *Phys.Rev. C*, 64:055801.

- Langer, N., El Eid, M. F., and Fricke, K. J. (1985). Evolution of massive stars with semiconvective diffusion. *Astron. Astrophys.*, 145:179–191.
- Liebendoerfer, M., Rosswog, S., and Thielemann, F.-K. (2002). An Adaptive Grid, Implicit Code for Spherically Symmetric, General Relativistic Hydrodynamics in Comoving Coordinates. *Astrophys.J.Suppl.* 141:229-246, 2002.
- Liebendörfer, M., Thielemann, F., and Rosswog, S. (2001). A Conservative Implementation of Shift Vectors in Spherically Symmetric General Relativistic Hydrodynamics. *Astrophys. J. Suppl. Ser.*, 141(astro-ph/0106539):229–246.
- Lindquist, R. W. (1966). Relativistic transport theory. *Annals of Physics*, 37(3):487–518.
- Matsuo, Y., Tsujimoto, H., Noda, T., Saruwatari, M., Ono, M., Hashimoto, M.-a., and Fujimoto, M. Y. (2011). Effects of a new triple- α reaction on X-ray bursts of a helium-accreting neutron star. *Progress of Theoretical Physics*, 126(6):1177–1186.
- Oppenheimer, J. R. and Volkoff, G. M. (1939). On Massive Neutron Cores. *Phys. Rev.*, 55(4):374–381.
- Paczynski, B. (1983). Models of X-ray bursters with radius expansion. *The Astrophysical Journal*, 267:315–321.
- Paul, B., Saripalli, L., and Archana, M. (2012). Simultaneous X-ray and optical observations of thermonuclear bursts in the LMXB EXO 0748-676 and prospects with ASTROSAT. In *39th COSPAR Scientific Assembly*, volume 39, page 1468.
- Paxton, B., Bildsten, L., Dotter, A., Herwig, F., Lesaffre, P., and Timmes, F. (2011). Modules for Experiments in Stellar Astrophysics (MESA). page ApJS.
- Paxton, B., Cantiello, M., Arras, P., Bildsten, L., Brown, E. F., Dotter, A., Mankovich, C., Montgomery, M., Stello, D., Timmes, F., et al. (2013). Modules for Experiments in Stellar Astrophysics (MESA): Planets, Oscillations, Rotation, and Massive Stars. *The Astrophysical Journal Supplement Series*, 208(1):4.
- Peng, F., Brown, E. F., and Truran, J. W. (2007). Sedimentation and type I X-ray bursts at low accretion rates. *The Astrophysical Journal*, 654(2):1022.
- Potekhin, A. Y., Chabrier, G., and Yakovlev, D. G. (1997). Internal temperatures and cooling of neutron stars with accreted envelopes. *Astron. Astrophys.*, 323:415.
- Potekhin, A. Y. and Yakovlev, D. G. (2001). Thermal structure and cooling of neutron stars with magnetized envelopes. *Astron.Astrophys.*, 374:213–226.
- Prendergast, K. and Burbidge, G. (1968). On the nature of some galactic X-ray sources. *The Astrophysical Journal*, 151:L83.
- Press, W. H., Flannery, B. P., Teukolsky, S. A., and Vetterling, W. T. (1992). *Numerical Recipes*. Cambridge University Press.
- Rakavy, G., Shaviv, G., and Zinamon, Z. (1967). -and Oxygen-burning stars and pre-supernova models. *The Astrophysical Journal*, 150:131.

- Remillard, R., Morgan, E., et al. (2005). Superburst in 4U1608-52. *The Astronomer's Telegram*, 482:1.
- Schatz, H., Aprahamian, A., Barnard, V., Bildsten, L., Cumming, A., Ouellette, M., Rauscher, T., Thielemann, F.-K., and Wiescher, M. (2001). End point of the rp process on accreting neutron stars. *Physical Review Letters*, 86(16):3471.
- Schatz, H., Aprahamian, A., Görres, J., Wiescher, M., Rauscher, T., Rembges, J., Thielemann, F.-K., Pfeiffer, B., Möller, P., Kratz, K.-L., et al. (1998). rp-Process nucleosynthesis at extreme temperature and density conditions. *Physics reports*, 294(4):167–263.
- Schatz, H., Bildsten, L., Cumming, A., and Wiescher, M. (1999). The rp Process Ashes from Stable Nuclear Burning on an Accreting Neutron Star.
- Schatz, H., Gupta, S., Möller, P., Beard, M., Brown, E. F., Deibel, A. T., Gasques, L. R., Hix, W. R., Keek, L., Lau, R., Steiner, A. W., and Wiescher, M. (2013). Strong neutrino cooling by cycles of electron capture and β^- decay in neutron star crusts.
- Schenk, O., Gärtner, K., Fichtner, W., and Stricker, A. (2001). PARDISO: a high-performance serial and parallel sparse linear solver in semiconductor device simulation. *Future Generation Comp. Syst.*, 18(1):69–78.
- Schinder, P. J., Schramm, D. N., Wiita, P. J., Margolis, S. H., and Tubbs, D. L. (1987). Neutrino emission by the pair, plasma, and photo processes in the Weinberg-Salam model. *Astrophys.J.*, 313:531–542.
- Serino, M., Mihara, T., Matsuoka, M., Nakahira, S., Sugizaki, M., Ueda, Y., Kawai, N., and Ueno, S. (2012). Superburst with Outburst from EXO 1745- 248 in Terzan 5 with MAXI. *Publications of the Astronomical Society of Japan*, 64(5):91.
- Shapiro, S. L. and Teukolsky, S. A. (1983). *Black Holes, White Dwarfs, and Neutron Stars*. Wiley-Interscience, New York.
- Shternin, P. S., Yakovlev, D. G., Heinke, C. O., Ho, W. C. G., and Patnaude, D. J. (2011). Cooling neutron star in the Cassiopeia A supernova remnant: Evidence for superfluidity in the core. *page Mon. Not. Roy. Astron. Soc.*
- Shu, F. H. (1991). *The Physics of Astrophysics: Gas Dynamics*, volume 2. University Science Books.
- Stella, L., Friedhorsky, W., and White, N. (1987). The discovery of a 685 second orbital period from the X-ray source 4U 1820-30 in the globular cluster NGC 6624. *The Astrophysical Journal*, 312:L17–L21.
- Stevens, J., Brown, E. F., Cumming, A., Cyburt, R., and Schatz, H. (2014). Carbon Synthesis in Steady-State Hydrogen and Helium Burning On Accreting Neutron Stars. *arXiv preprint arXiv:1405.3541*.

- Strohmayer, T., Giles, B., Jahoda, K., and Lee, U. (1996). High Frequency Oscillations During Type I Bursts: Evidence for Millisecond Rotators in LMXB. In *Bulletin of the American Astronomical Society*, volume 28, page 1425.
- Strohmayer, T. E. and Brown, E. F. (2002). A remarkable 3 hour thermonuclear burst from 4U 1820–30. *The Astrophysical Journal*, 566(2):1045.
- Strohmayer, T. E. and Markwardt, C. B. (2002). Evidence for a Millisecond Pulsar in 4U 1636–53 During a Superburst. *Astrophys.J.*, 577:337–345.
- Sánchez-Fernández, C. (2012). The catalogue of X-ray bursts detected by JEM-X onboard INTEGRAL. In *Astrostatistics and Data Mining*, page 233–237. Springer.
- Taam, R. E. and Picklum, R. E. (1978). Nuclear fusion and carbon flashes on neutron stars. , 224:210–216.
- Thorne, K. S. (1977). The relativistic equations of stellar structure and evolution. *Astrophys.J.*, 212:825–831.
- Turlione, A., Aguilera, D. N., and Pons, J. A. (2013). Quiescent thermal emission from neutron stars in LMXBs.
- Urpin, V. and Yakovlev, D. (1980). Thermogalvanomagnetic effects in white dwarfs and neutron stars. *Soviet Astronomy*, 24:425.
- van Paradijs, J. and Lewin, W. H. (1988). X-ray bursts?Some recent developments. *Advances in Space Research*, 8(2):461–475.
- Van Wormer, L., Görres, J., Iliadis, C., Wiescher, M., and Thielemann, F.-K. (1994). Reaction rates and reaction sequences in the rp-process. *The Astrophysical Journal*, 432:326–350.
- Wallace, R. and Woosley, S. (1981). Explosive hydrogen burning. *The Astrophysical Journal Supplement Series*, 45:389–420.
- Watts, A. L. (2012). Thermonuclear burst oscillations. page 609–640.
- Weaver, T. A. and Woosley, S. E. (1978). Evolution and explosion of massive stars. Technical report, California Univ., Livermore (USA). Lawrence Livermore Lab.
- Woosley, S. and Taam, R. E. (1976). Gamma-ray bursts from thermonuclear explosions on neutron stars. *Nature*, 263:101–103.
- Yakovlev, D. G., Levenfish, K. P., and Gnedin, O. Y. (2005). Pycnonuclear reactions in dense stellar matter. *The European Physical Journal A*, 25(1):669.
- Zamfir, M., Cumming, A., and Niquette, C. (2014). The Thermal Stability of Helium Burning on Accreting Neutron Stars.
- Zhang, G., Méndez, M., Altamirano, D., Belloni, T. M., and Homan, J. (2009). A very rare triple-peaked type-I X-ray burst in the low-mass X-ray binary 4U 1636–53. *Monthly Notices of the Royal Astronomical Society*, 398(1):368–374.

Curriculum Vitae

Personal Data

Name	Sofie Fehlmann
Address	Wiesenstrasse 11 4600 Olten
Phone	0041 78 829 36 55
Email	sofie.fehlmann@gmail.com
Homepage	phys-merger.physik.unibas.ch/~sfehlmann
Date of Birth	06.02.1985

Education

2011 - 2015	PhD at the University of Basel in theoretical physics <i>Numerical Simulations of X-ray Bursts and Superbursts</i> Supervisor: Prof. Dr. F.-K. Thielemann, Prof. Dr. M. Liebendörfer
2007 - 2010	Master in physics at the University of Basel <i>Axissymmetric Simulations of Magnetorotational Instabilities</i> Supervisor: Prof. Dr. M. Liebendörfer
2004 - 2007	Bachelor in physics at the University of Basel
2000 - 2004	High school diploma in physics and applied mathematics at the Kantonsschule in Olten (SO)
1998 - 2000	Bezirksschule Schönenwerd (SO)
1992 - 1998	Elementary school in Niedergösgen (SO)

Professional Experience

2014 -	Joint owner of the World of Fehlmann GmbH
February 2013	Workshop at the CSCS in Lugano: <i>Introduction to OpenACC and CUDA Programming</i>
April 2011	Workshop in Chiemsee (DE): <i>Numerical Simulations of Nuclear Reaction Network</i>
2009 - 2011	Assistant at the Institute of Mathematics in Basel
2006 - 2010	Junior research assistant at the Department of Physics in Basel
August 2009	Practical training at the Paul Scherrer Institute in Villigen (AG)

Language Skills

German	first language
English	fluent
French	intermediate
Hungarian	basic knowledge

Skills

Programming knowledge	Fortran, Python, Latex, Excel, Java, Matlab, Mathematica, IDL, HTML, LabView
Operation systems	Unix, Linux, Windows

Hobbies

Boogie Woogie, Rock'n'Roll, cycling, jogging